REDUCING RISK IN LITHOLOGY AND FLUID DISCRIMINATION

WITH ATTRIBUTES DERIVED FROM SEISMIC INVERSION

_____

A Thesis Presented to

the Faculty of the Department of Earth and Atmospheric Sciences

University of Houston

_____

In Partial fulfillment

of the Requirements for the Degree

Master of Science

_____

By

Syed Omar Zaman

May 2016

REDUCING RISK IN LITHOLOGY AND FLUID DISCRIMINATION

WITH ATTRIBUTES DERIVED FROM SEISMIC INVERSION

_____

Syed Omar Zaman

APPROVED:

_____

Dr. Aibing Li, Chairman
Department of Earth and Atmospheric Sciences

_____

Dr. Fred Hilterman, Advisor
Department of Earth and Atmospheric Sciences

_____

Dr. Hua - Wei Zhou, Member
Department of Earth and Atmospheric Sciences

_____

Dr. Doug McCowan, Member
The University of Texas at Austin

_____

Dean, College of Natural Sciences & Mathematics

ACKNOWLEDGEMENTS

REDUCING RISK IN LITHOLOGY AND FLUID DISCRIMINATION

WITH ATTRIBUTES DERIVED FROM SEISMIC INVERSION

_____

An Abstract of a Thesis

Presented to

the Faculty of the Department of Earth and Atmospheric Sciences

University of Houston

_____

In Partial fulfillment

of the Requirements for the Degree

Master of Science

_____

By

Syed Omar Zaman

May 2016

Abstract

Pre-stack simultaneous inversion of seismic reflection data, a methodology based on amplitude variations with offset (AVO), presents a more flexible and detailed tool than traditional post-stack amplitude analysis. Given an initial earth model from well logs and structural geology interpretation, the simultaneous extraction of acoustic (AI) and shear impedances (SI) from seismic data allows for an effective transform of the seismic reflectivity series to layered rock properties. In the High Island Area, offshore Gulf of Mexico, the sand and shale lithologies show relatively equal acoustic impedance values and Class 2 AVO in the presence of hydrocarbons. To extract a thorough suite of rock property information from seismic in this environment, I use inverted AI and SI measurements to derive other seismic attributes, such as Lambda-Rho ($\lambda\rho$), Mu-Rho ($\mu\rho$), and water saturation (Sw). By deriving these attributes, rock property information such as rock type, porosity, and pore fluid content can be translated from localized well data to the larger seismic volume. These derived attributes assist in defining relationships between properties that distinguish the sedimentary rock type that AI and density from post-stack amplitude analysis alone cannot. The results of the experiment showed a successful establishment of relationships to separate sand and shale lithology, as well as the extraction of structurally-conformable hydrocarbon-bearing sand in conformance with seismic AVO attributes and termination against faults in the study area which act as seals to the gas sand reservoirs.

CONTENTS

CHAPTER 1

INTRODUCTION

1.1 Background

Seismic amplitude interpretation techniques are varied in approach and assumptions, though all seek to accomplish the same goal of extending geologic knowledge. By understanding the change in amplitude-versus-offset, critical information such as lithology and pore fluid can be extracted from seismic reflection data. When it comes to gas sand discrimination, a typical seismic response is large negative reflection amplitudes, also known as bright spots. As established in the 1970's, bright spots and other amplitude anomalies are the main tools in delineating gas bearing sands because of a reservoir rock's acoustic impedance significantly decreasing relative to the surrounding strata with a change from water to gas saturation (Hilterman, 2001). These methods, however, do not adequately take into account changing lithology, and most importantly for this study, economic versus fizz (non-economic) gas saturation. Due to the non-uniqueness of amplitude anomalies being correlated to commercial gas saturation, a closer evaluation process is necessary.

Ostrander (1984) introduced the correlation of the change in Poisson's ratio between two media and showed how this affects amplitude as a function of incident-angle. In general, gas-saturated lithologies will have a lower Poisson's ratio than a water

bearing unit of similar lithology. Following Koefoed's work (1955), four variables were
initially determined by Ostrander critical to understand a reflection coefficient:

1. Compressional velocity ratio between the upper and lower media,

2. Density ratio between the upper and lower media,

3. Poisson's ratio of the upper medium, and

4. Poisson's ratio of the lower medium.

Poisson's ratio (σ) can be expressed as a function of the compressional and shear
velocities (Vp/Vs) as

$$\sigma = \frac{1}{2} \left[\frac{(Vp/Vs)^2 - 2}{(Vp/Vs)^2 - 1} \right] \qquad\qquad (1.1)$$

In short, three measurable factors from the upper and lower media around an
interface are all that are needed to understand a reflection from that interface; they are

1. Compressional velocity (Vp),

2. Density (ρ), and

3. Shear velocity (Vs).

These three variables, which can be extracted from seismic data, are related to the
elastic parameters of bulk modulus, κ, and shear modulus, μ as

$$Vp = \sqrt{(\kappa + 4/3\mu)/\rho} = \alpha \text{ , and} \qquad\qquad (1.2)$$

$$Vs = \sqrt{\mu/\rho} = \beta . \qquad\qquad (1.3)$$

An exploration goal for all potential hydrocarbon surveys is the estimation of the petrophysical properties of the reservoir, such as water saturation, lithology, and porosity. These petrophysical properties derived from seismic are calibrated to the same petrophysical properties derived from well-log curves by various methods such as crossplots. Finally, in order to estimate rock property variations when the petrophysical properties are varied, the rock properties (Vp and Vs) are expressed as a function of their elastic constants (bulk and shear moduli).

1.2 AVO Properties and Signatures

The theoretical foundation on how reflection coefficients vary as a function of incident angle was established by the Zoeppritz (1919) equations. Zoeppritz's equations are based on four boundary conditions that result in the four reflection and/or transmitted amplitudes being expressed in a 4x4 matrix containing the rock properties and propagation angles. From these 4x4 matrices, it is difficult to interpret how the reflection amplitude relates directly to rock properties. Subsequently, many reflection coefficient approximations have been implemented to streamline the relationship of amplitude and rock properties. An early linearization of these equations that formed the foundation of later work was derived by Bortfeld (1961), which is often expressed in fluid and rigidity terms as shown in Figure 1.1. Shuey (1985) modified this relationship with the following equations to associate specific rock properties with different incident-angle ranges:

$$R(\theta) = A + B\sin^2\phi + C(\tan^2\phi - \sin^2\phi) \tag{1.4}$$

$$A = \text{Normal Incident Reflectivity} = \frac{1}{2}\left(\frac{\Delta\alpha}{\alpha} + \frac{\Delta\rho}{\rho}\right) \qquad (1.5)$$

$$B = \Delta\sigma/(1-\sigma)^2 \qquad (1.6)$$

$$C = {}^{1}/_{2}\left(\Delta\alpha/\alpha\right) \qquad (1.7)$$

where α represents p-wave velocity; β, s-wave velocity; ρ, density; and, σ, Poisson's ratio. The angle θ on the left side of equation 1.4 represents the angle of incidence, while the angle ϕ on the right is the average of the incident and transmitted angles. The first term, A, represents the amplitude at normal incidence, also known as acoustic impedance. The second term, B, becomes more pronounced for incident-angles between 15° and 90°, and it is mainly a function of the change in Poisson's ratio between the lower and upper media. The term B is also a reflectivity, which is known as Poisson reflectivity (Verm and Hilterman, 1995). At angles greater than 30°, the third term's change in compressional velocity increasingly influences the reflection amplitude.

Rutherford and Williams (1989) defined three major AVO classification groups, each defined primarily by the normal-incident amplitude for shale over a gas-saturated sandstone. They are:

1. Class I AVO – High-Impedance Sand,

2. Class II AVO – Near-Zero Impedance Sand, and

3. Class III AVO – Low-Impedance Sand.

Class III AVO sands are found mostly in uncompacted, unconsolidated sandstones with a hydrocarbon saturation that gives the sandstone a lower acoustic impedance than the surrounding media. These sand units typically do not have a large change in amplitude with offset, so CMP stacking does not greatly distort the reflection. Class III gas sands are readily recognized as bright spots (large amplitudes) in seismic sections.

Class II AVO sands have similar or near-equal acoustic impedance values to the surrounding media. Due to this, CMP stacking may not easily highlight the interface between the different lithologies. With sufficient incident-angle coverage, the reflection becomes more apparent as the relative amplitude increases with increasing offset. On a full CMP stack, Class II AVO anomalies are often identified by the phase reversals along an interface where the sand unit changes from gas to brine saturation. The magnitude of the AVO gradient for a Class II seismic anomaly is generally greater than those for a Class III anomaly.

Class I AVO sands generally represent well-consolidated, compacted units at depth. These sands have higher acoustic impedance values than the surrounding media. In a CMP stack, a Class I gas-saturated event would be identified as a dim spot compared to the brine-saturated portion of the event. The magnitude of the AVO gradient of Class I anomalies is greater than those for Class II or Class III. Within CMP gathers, it is not unusual for Class 1 anomalies to exhibit a phase reversal with greater offset. Figure 1.2 summarizes the three classifications, as well as the later defined Class IV anomaly

signature, a negative impedance event with decreasing magnitude over incident-angle (Castagna and Smith, 1994).
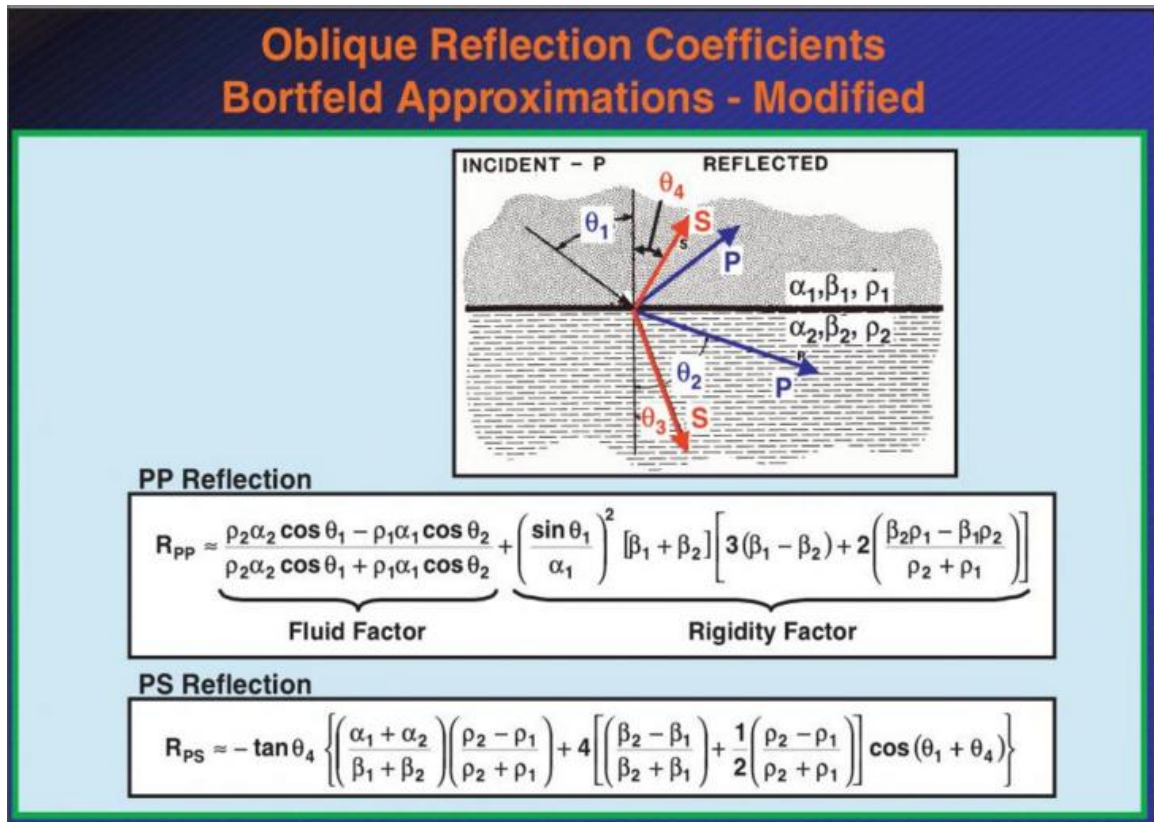

Figure 1.1 Illustration of the Bortfeld (1961) linearization of the Zoeppritz (1919) equations. For a p-wave reflection, the equation can be expressed in fluid and rigidity terms. (Hilterman, 2001)
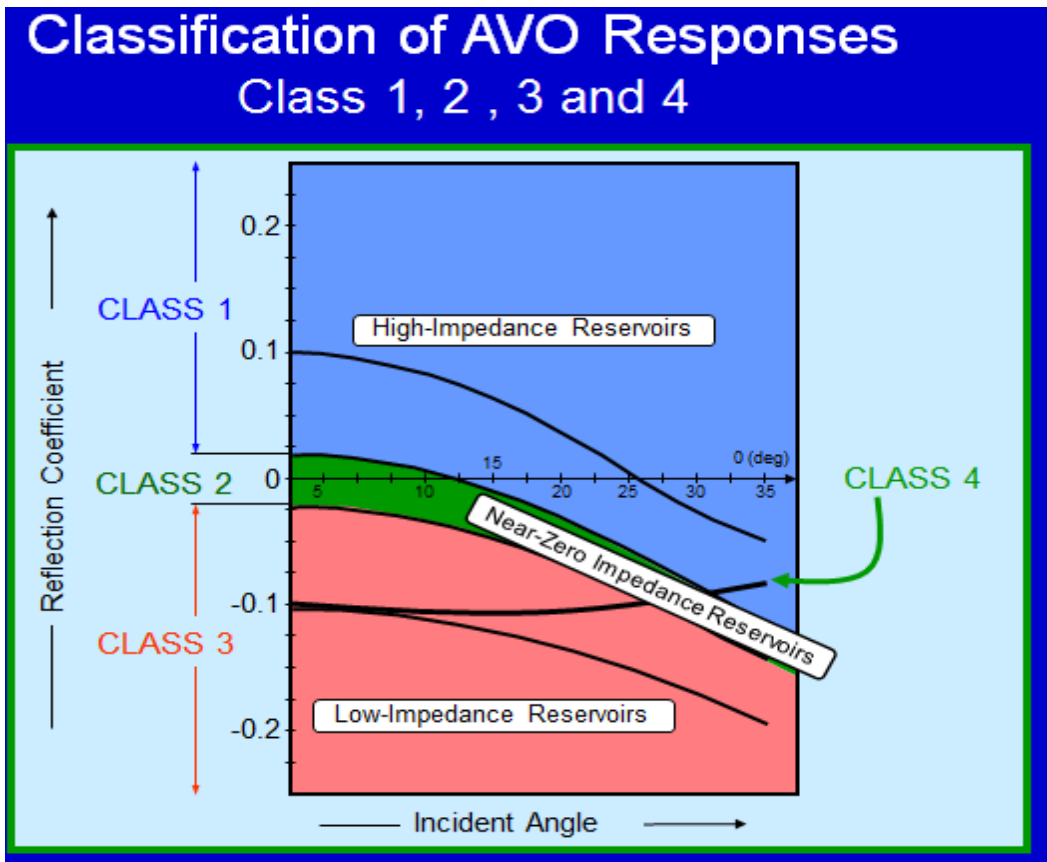
Figure 1.2 Summary of AVO Classification (Hilterman, 2001)

1.3 Rock Property Estimation from AVO Data

For this study, a technique called simultaneous seismic inversion was used to extract rock-property information from AVO data. As detailed by Ma (2002), pre-stack inversion simultaneously estimates acoustic (AI) and shear impedances (SI) from pre-stack data, rather than using a two-step process of first estimating the normal incident and gradient traces to estimate AI and SI. Since seismic data normally does not have stable frequency components beneath 6 Hz, low-frequency background functions were derived from well-log data to serve as the initial guess of the AI, SI, and density models and

7

interpolated throughout the seismic dataset. Then, the AI, SI, and density models are updated to better match synthetic seismic data with the observed seismic data through a global search algorithm and a general linear-inversion process. The process reiterated until a match between the synthetic and actual field data are at a "best" fit for the given wavelet, seismic data, and low-frequency model. The three inverted seismic volumes, AI, SI, and density were then used to derive numerous other elastic parameters and rock-property volumes.

One issue that sometimes plagues traditional elastic inversion is that seismic traces at large incident-angles, which contain much of the Poisson's ratio information, are subject to large normal moveout (NMO) stretch, which can then drift the far-angle wavelet away from the baseline wavelet (Ma, 2002). Simultaneous inversion has the ability to account for these wavelet differences by assigning a different extracted wavelet to each of the input angle-limited stacks, and to allow a specified attenuation mechanism to account for any time-varying effects. For this research, variable wavelets were extracted for different angles of incidence. In my research, I did not implement spatially-variant wavelets, though that is a possibility for a larger area.

1.4 Research Objective

My research objective was to determine the effectiveness of simultaneous inversion in a legacy seismic volume with a poor signal-to-noise ratio that contained difficult to interpret Class II AVO signatures across known gas reservoirs. My primary

goal was to reliably discriminate between shale, wet sand, and gas sand in a 3D volume. My secondary objective was to estimate water saturation for the gas sand units. I used well-log data as the control for the experiment, both to constrain inversion results, as well as to QC the final data.

1.5 Available Data

The available seismic data for this research were provided by Fairfield Industries, and well-log information was provided by Geokinetics Inc. The seismic data included CMP gathers, near (2-15°), far (15-42°), and full angle (0-42°) volume stacks. The seismic data set that I used for this interpretation represented the earlier stages of processing by Fairfield, which utilized true amplitude and controlled - phase processing and Kirchhoff Pre-Stack Time Migration. The processing history is detailed in Figure 1.4. The seismic project grid geometry has an inline range labeled from 1786-1965, incremented by 1, and crossline range from 3876-4382, incremented by 2. Inline spacing was 55 ft. and crossline spacing was 110 ft. The maximum reflection time was 7.8 seconds, and the sample rate was 6 ms. With this sample rate, the Nyquist frequency was 83 Hz, which was deemed to be sufficient for the survey. A total of 20 wells with well-log curves were obtained for this research. The curves available included: gamma ray, spontaneous potential (SP), sonic, bulk density, neutron porosity, caliper, deep resistivity, and sand percentage. Not all of the wells had every curve available, so there was some work in determining which wells were feasible for inversion property building versus "blind" wells for QC of the results. The research was primarily conducted utilizing

Schlumberger's Petrel software for horizon and fault interpretation, seismic attribute generation, and seismic inversion and Petroseismic's jTIPS for AVO model building, log analysis, and pore-fluid analysis. Pre-stack pre-processing of CMP data was conducted using Schlumberger's Omega software.
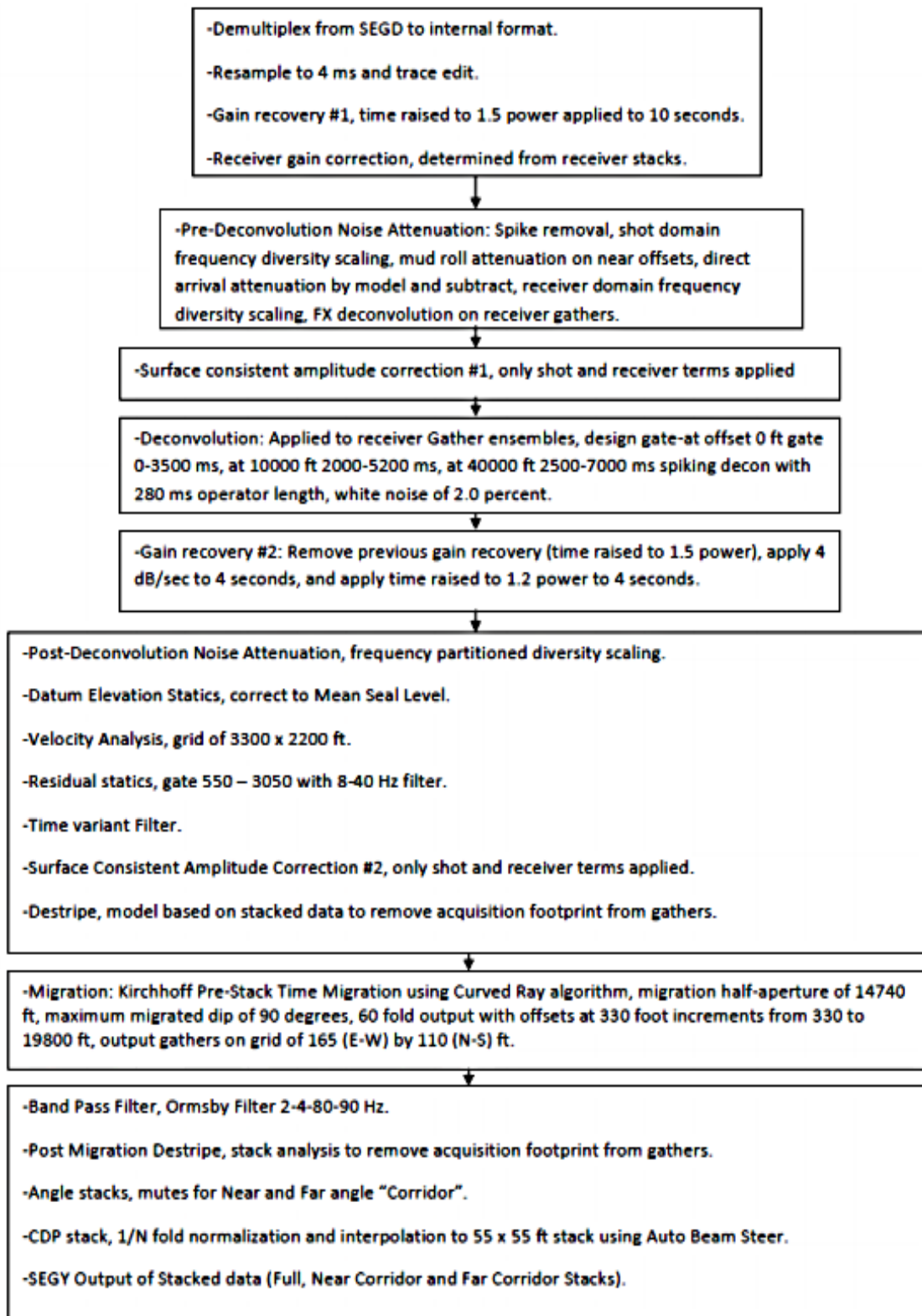
-Demultiplex from SEGD to internal format.

-Resample to 4 ms and trace edit.

-Gain recovery #1, time raised to 1.5 power applied to 10 seconds.

-Receiver gain correction, determined from receiver stacks.

-Pre-Deconvolution Noise Attenuation: Spike removal, shot domain frequency diversity scaling, mud roll attenuation on near offsets, direct arrival attenuation by model and subtract, receiver domain frequency diversity scaling, FX deconvolution on receiver gathers.

-Surface consistent amplitude correction #1, only shot and receiver terms applied

-Deconvolution: Applied to receiver Gather ensembles, design gate-at offset 0 ft gate 0-3500 ms, at 10000 ft 2000-5200 ms, at 40000 ft 2500-7000 ms spiking decon with 280 ms operator length, white noise of 2.0 percent.

-Gain recovery #2: Remove previous gain recovery (time raised to 1.5 power), apply 4 dB/sec to 4 seconds, and apply time raised to 1.2 power to 4 seconds.

-Post-Deconvolution Noise Attenuation, frequency partitioned diversity scaling.

-Datum Elevation Statics, correct to Mean Seal Level.

-Velocity Analysis, grid of 3300 x 2200 ft.

-Residual statics, gate 550 – 3050 with 8-40 Hz filter.

-Time variant Filter.

-Surface Consistent Amplitude Correction #2, only shot and receiver terms applied.

-Destripe, model based on stacked data to remove acquisition footprint from gathers.

-Migration: Kirchhoff Pre-Stack Time Migration using Curved Ray algorithm, migration half-aperture of 14740 ft, maximum migrated dip of 90 degrees, 60 fold output with offsets at 330 foot increments from 330 to 19800 ft, output gathers on grid of 165 (E-W) by 110 (N-S) ft.

-Band Pass Filter, Ormsby Filter 2-4-80-90 Hz.

-Post Migration Destripe, stack analysis to remove acquisition footprint from gathers.

-Angle stacks, mutes for Near and Far angle "Corridor".

-CDP stack, 1/N fold normalization and interpolation to 55 x 55 ft stack using Auto Beam Steer.

-SEGY Output of Stacked data (Full, Near Corridor and Far Corridor Stacks).

Figure 1.3 Processing workflow (Courtesy of Fairfieldnodal Industries)

1.6 Research Outline

The first action to be taken in this research was to orient myself with the available well logs and seismic volumes. Well-log interpretation and seismic-well tie analyses was necessary to ensure that formations of interest were identified. Various rock properties that were not directly measured, such as fluid-substituted velocities and elastic parameters such as Lambda-Rho, were created in order to understand the petrophysical properties. Crossplots of key parameters were generated to begin delineating lithology and pore fluid from the well curves. After estimating wavelets for the available wells, synthetic seismograms were generated to calibrate the borehole information in depth to the seismic data in time.

Following the initial petrophysical interpretation, I utilized the existing stack and angle - stack volumes and interpreted horizons based on markers in the well logs. Due to the strong faulting in the area, I built a fault framework to understand how this affected my horizon interpretation.

Fluid substitution was implemented on the well-log curves to generate different scenarios of water and gas saturation to better understand the effect of gas saturation on the seismic. The target area was expected to showcase Class II AVO, and this was compared to the actual seismic in brine and gas saturated formations. The AVO modeling was accomplished using PetroSeismic's jTIPS Well Log Modeling software.

Utilizing Schlumberger's Omega and Petrel software, the pre-stack seismic data was restacked in 10 degree bands (0-10°, 10-20°, 20-30°, and 30-40°). In order to derive the three attribute volumes of AI, SI and density, the software required a minimum of three input angle stacks. To better highlight Class II AVO signature at far offsets, I included a fourth band at larger angles. By utilizing partial stacks rather than raw gathers, noise contamination was mitigated. These angle-stack groups were analyzed for residual moveout and static errors. After generating new wavelets for each angle band, the angle-stacks, along with low-frequency Vp, Vs, and density volumes estimated from well-logs, were used in the simultaneous-inversion process to generate 3D inversion cubes.

Using the inversion results and crossplot trends generated during well-log interpretation, 3D volumes of rock properties and pore-fluid attributes were generated and the results compared to the well-log trends. The similarity or difference of the inverted elastic properties from those of the measured well-log data ultimately determined the success or failure of the inversion workflow on the dataset.

CHAPTER 2

GEOLOGY OF RESEARCH AREA

The study area was focused on a 3D seismic dataset from offshore Gulf of Mexico. The survey is located in the High Island Area, offshore of Texas. The geology of this region consists largely of alternating transgressive and high stand systems with erosional surfaces defining sequence boundaries and conformable shale layers at maximum flooding surfaces (Reymond and Stampfli, 1996). Structurally, growth faults related to these eustatic sequences are expected, as portrayed in Figure 2.1. Due to the shallow focus of the dataset, there are no major non-clastic geobodies expected to be imaged, such as the numerous salt bodies found further south in the Gulf of Mexico.

The Gulf of Mexico basin is a mostly circular structural basin with up to 15 km of sediments ranging in age from Late Triassic to Holocene (Boorman et al., 2006). The primary formation of the basin began in the Late Triassic with the breakup of Pangaea into the Gondwana and Laurasia continents. With the actions of Jurassic age rifting, and the subduction of the Farallon plate, the Western Interior Seaway, also known as the Cretaceous Seaway, presented an organic rich shallow marine environment on transitional continental crust that was a major source for hydrocarbon source rocks (Mitrovica et al, 1989). Throughout the Mesozoic, constantly changing eustatic sea levels allowed for anoxic conditions during transgressive phases, with rapid sedimentation and salt body formations during regressive phases. With the advent of the Laramide orogeny and

lowering sea levels, rapid sedimentation in the Paleocene began to deposit over the Mesozoic carbonate, salt, and organic shale formations. The primary reservoir rocks for this area of the northern Gulf of Mexico are typically mid - Miocene in age (Boorman et al., 2006; Rutherford and Williams, 1989).

With this geologic setting, the goals for the project can be set. The alternating layering of shale and sandstone units can be difficult to differentiate based on acoustic impedance alone at the depth of the target due to the similar normal incidence reflectivity. Utilizing well-log data as a control, $\lambda\rho$-$\mu\rho$ attributes can be used to better define the change between lithology (Benabentos, 2007). Faulting in the area also presented a quality control measure in regards to the termination and continuation of attribute facies against the fault plane. The faults in this environment contribute to the petroleum geology system as trap and seals to the reservoirs. In some exploration scenarios, potential hydrocarbon plays were evaluated based on the density change within the formation. However, this was risky due to the difficulty in extracting a high quality density attribute in the inversion process. P-wave and s-wave impedance attributes, such as $\lambda\rho$-$\mu\rho$ and Poisson's ratio assisted the interpretation process.
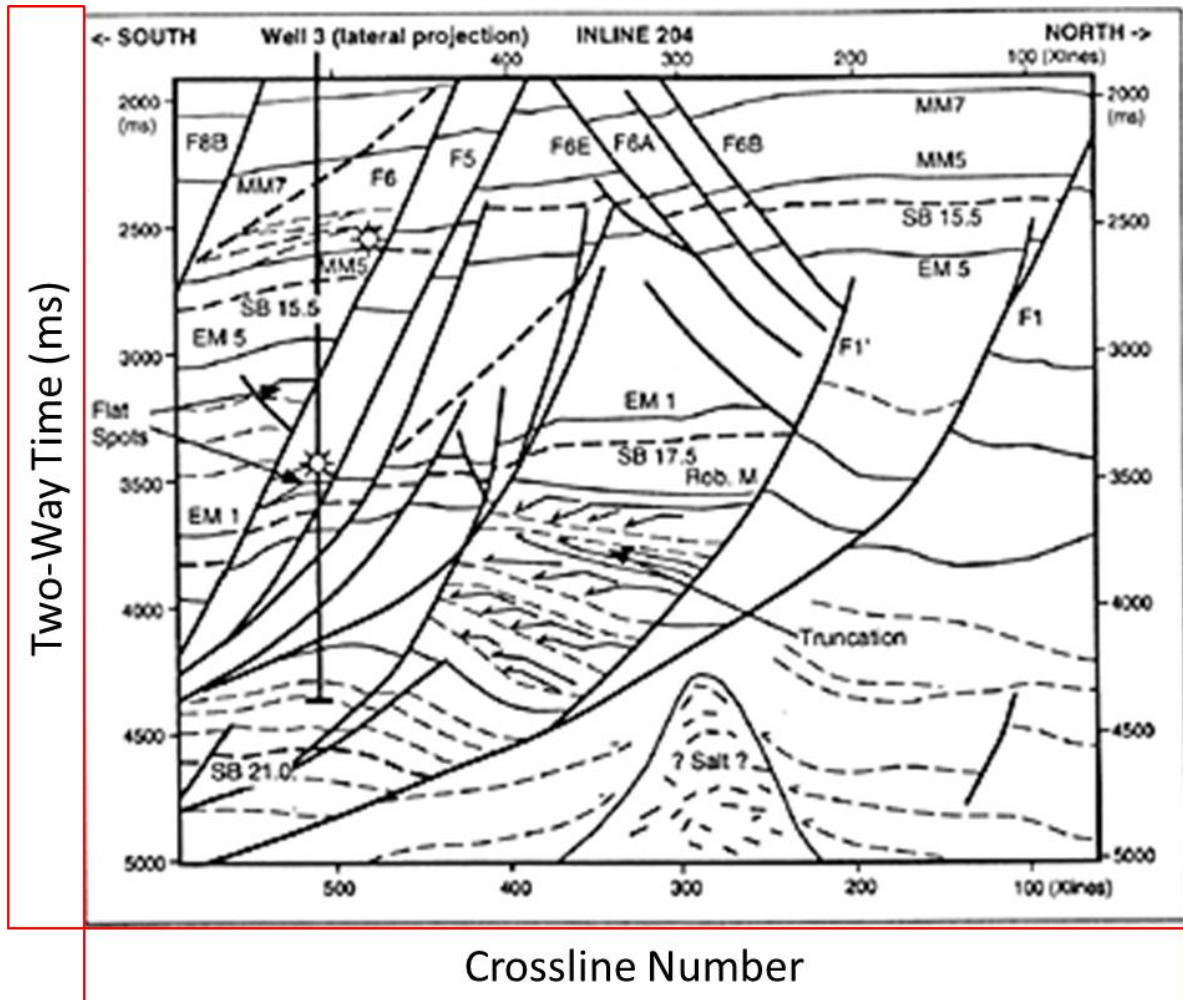
Figure 2.1. Interpretation derived from seismic. Growth faults associated with deposition from the north to the south dominate the structure. (Reymond and Stampfli, 1996).

CHAPTER III

WELL-LOG INTERPRETATION

3.1 Introduction

Before evaluating the entire seismic survey, significant geological information was extracted from the existing well logs. Five wells with sufficient logged data over a sufficient depth interval were analyzed. Each well log had a suite of sonic, gamma ray, spontaneous potential, neutron porosity, density, resistivity, and interpreter-derived sand percentage logs. Figure 3.1 displays a base map of the well locations with respect to the seismic survey geometry.

Figure 3.2 details the initial curves for Well A. Depth values were measured depth from Kelly bushing. Notable lithological changes were seen at the transition of thick sand formations with small shale sequences from 0-3000 ft. to a more shale dominated lithology down to around 9000 ft. Based on a zoomed view of the resistivity and neutron-density logs in Figure 3.3, there were potential hydrocarbon-bearing areas in two thin sand formations at 9065-9085 ft. and 9090-9102 ft. Figure 3.4 details the well-log data for Well B, which showcased a similar change from a likely transgressive system to a regressive environment at around 3300 feet. Based on a closer examination of the resistivity and neutron-density logs in Figure 3.5, this location had three potential hydrocarbon-bearing thin sands between 8250 and 8305 ft. Well-log curves in Well C, as

shown in Figure 3.6, start below the previously observed change in large sandstone units to the major shale unit. Similar to Well B, there were at least three potential hydrocarbon rich sands at around 9600 ft., at most 40 ft. layer thickness combined, as shown in Figure 3.7. Figure 3.8 highlights available well-log data in Well D and Figure 3.9 zooms to potential hydrocarbons at ~9600 ft. Well E, which lay close to Well B, differed in that it has evidence of at least two hydrocarbon-bearing sands of around 30-40 ft. thickness approximately 600 feet apart, rather than 1 or 2 very close thin sands. Figure 3.10 and 3.11 show the full log and a highlight of the gas sands, respectively.
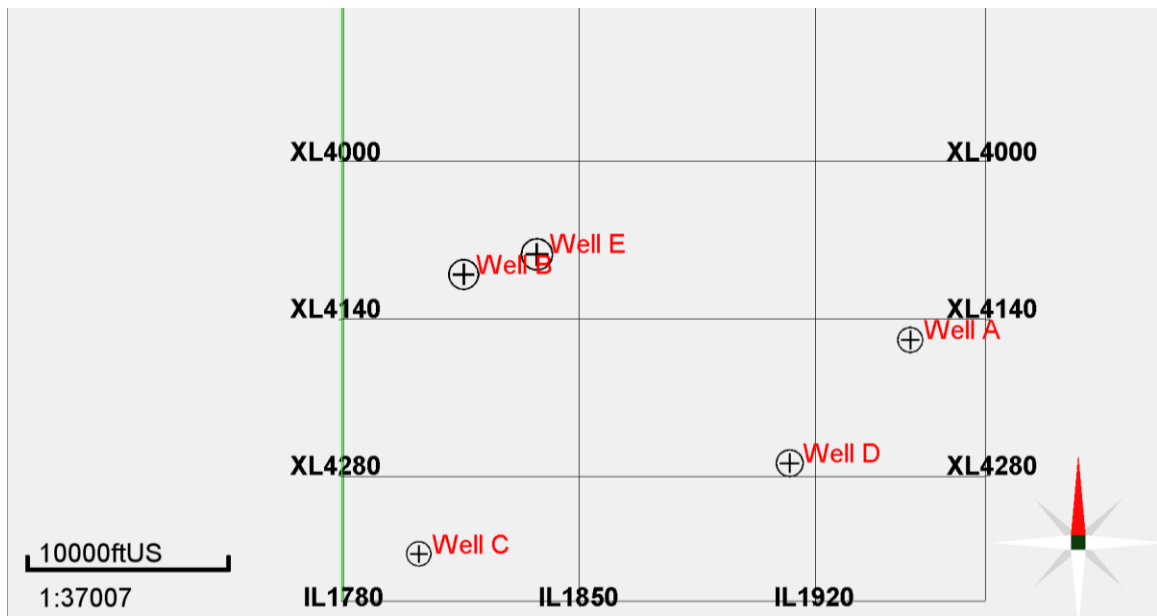
Figure 3.1 Base map of survey with well locations indicated.
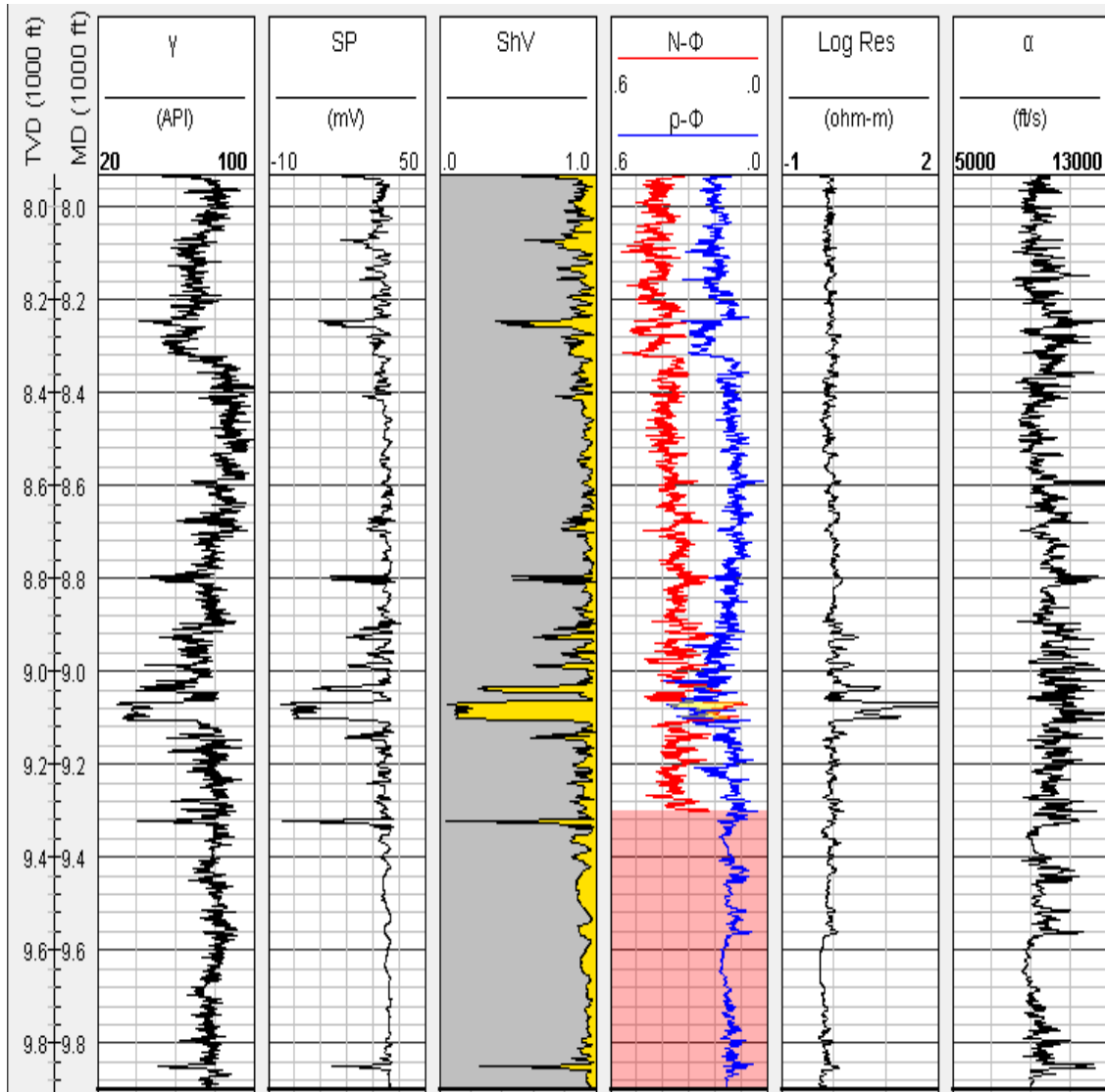
Figure 3.2 Well A well curves. Lithology below ~4500 ft. is dominantly shale with thin sand interbeds. Potential gas bearing formation occurs around 9000 ft.
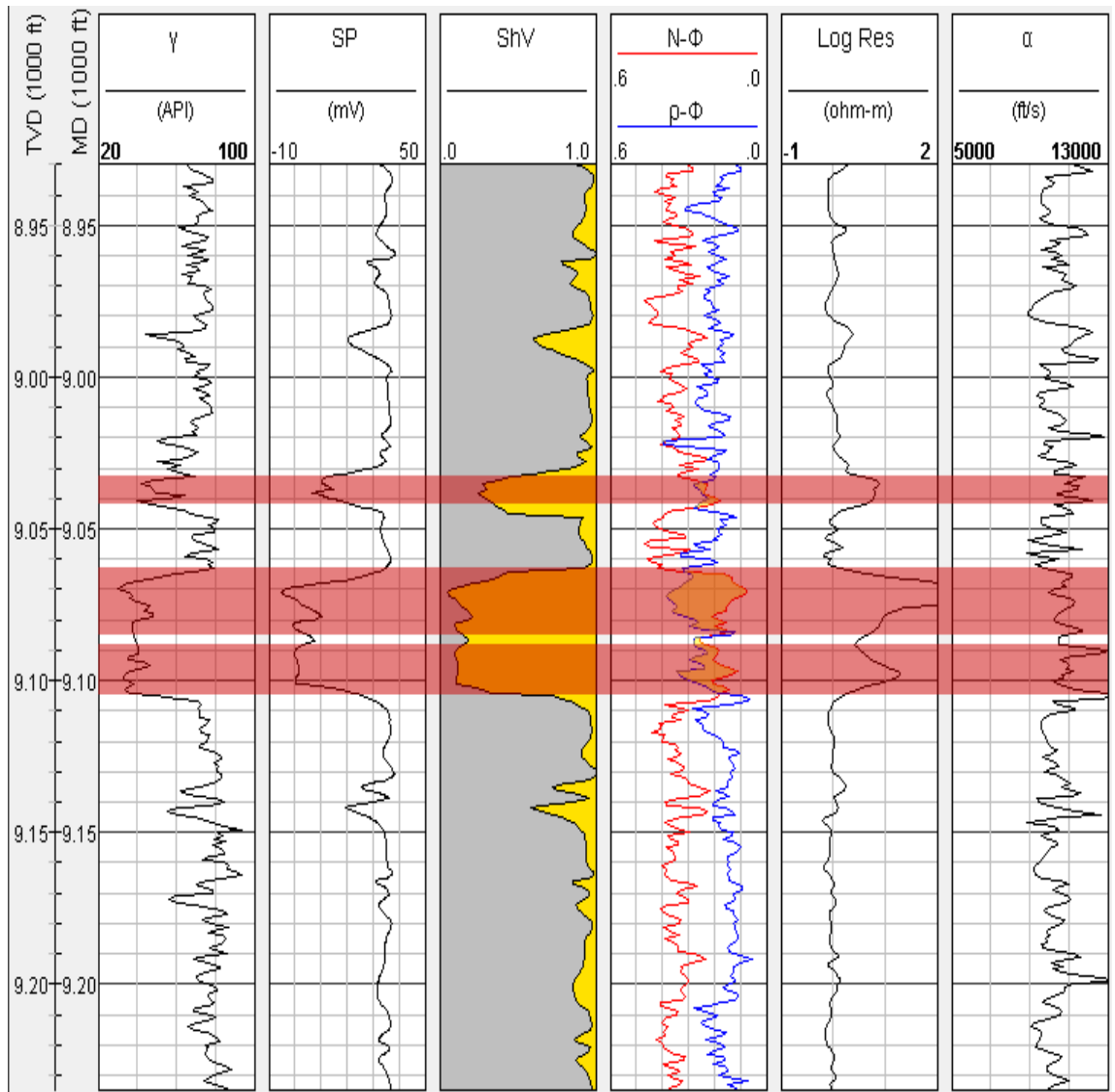
Figure 3.3 Zoomed view of Well A curves at reservoir level. There are potential hydrocarbons in two thin sand formations at 9065-9085 ft. and 9090-9102 ft.
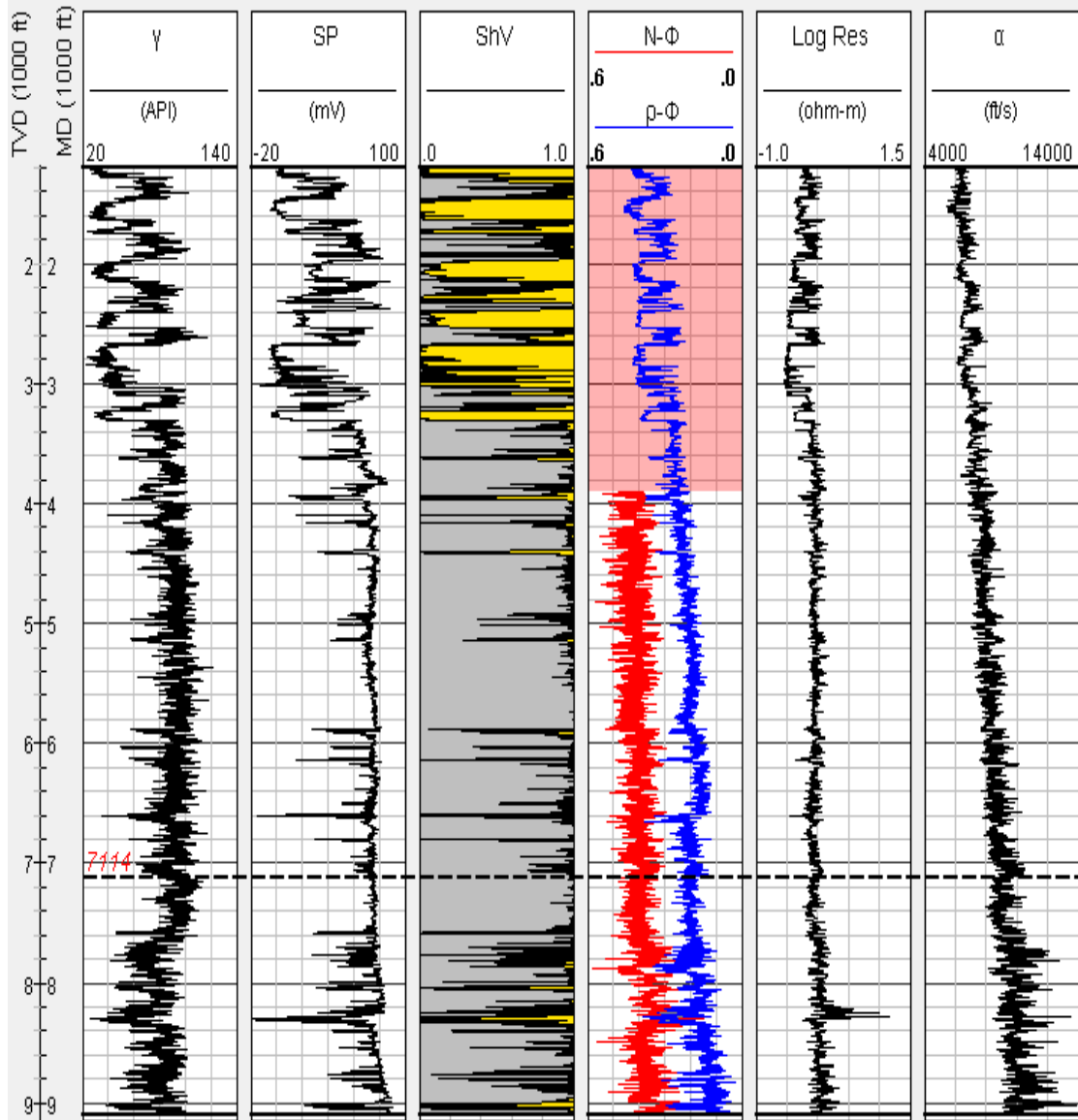
Figure 3.4 Well B well curves. Lithology below ~4000 ft. is dominantly shale with thin
sand interbeds. Potential gas bearing formation occurs around 8200 ft.
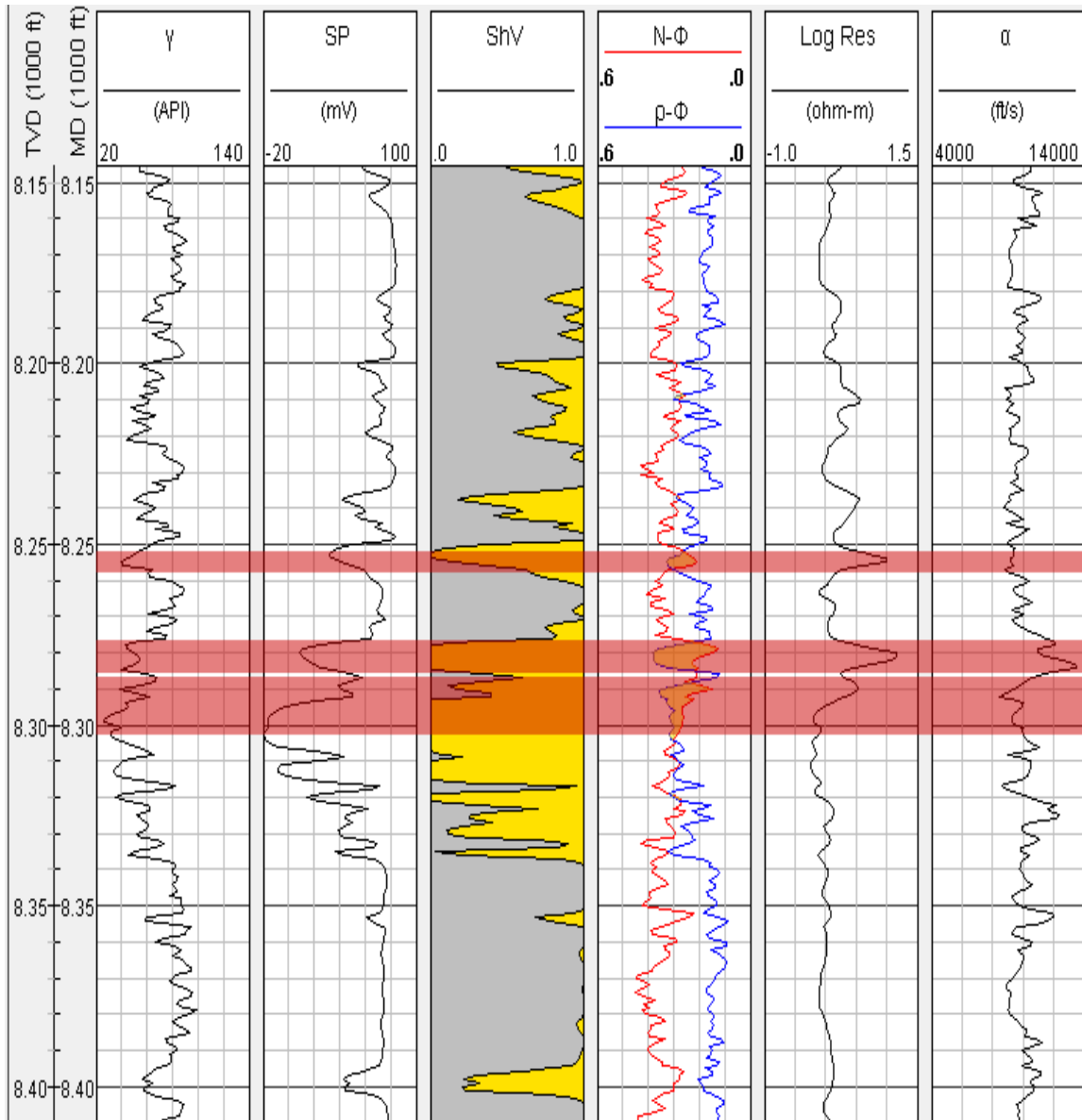
Figure 3.5 Zoomed view of Well B at reservoir level. Log curves indicate two close together potential reservoir rocks. This location has three potential hydrocarbon-bearing thin sands between 8250 and 8305 ft.
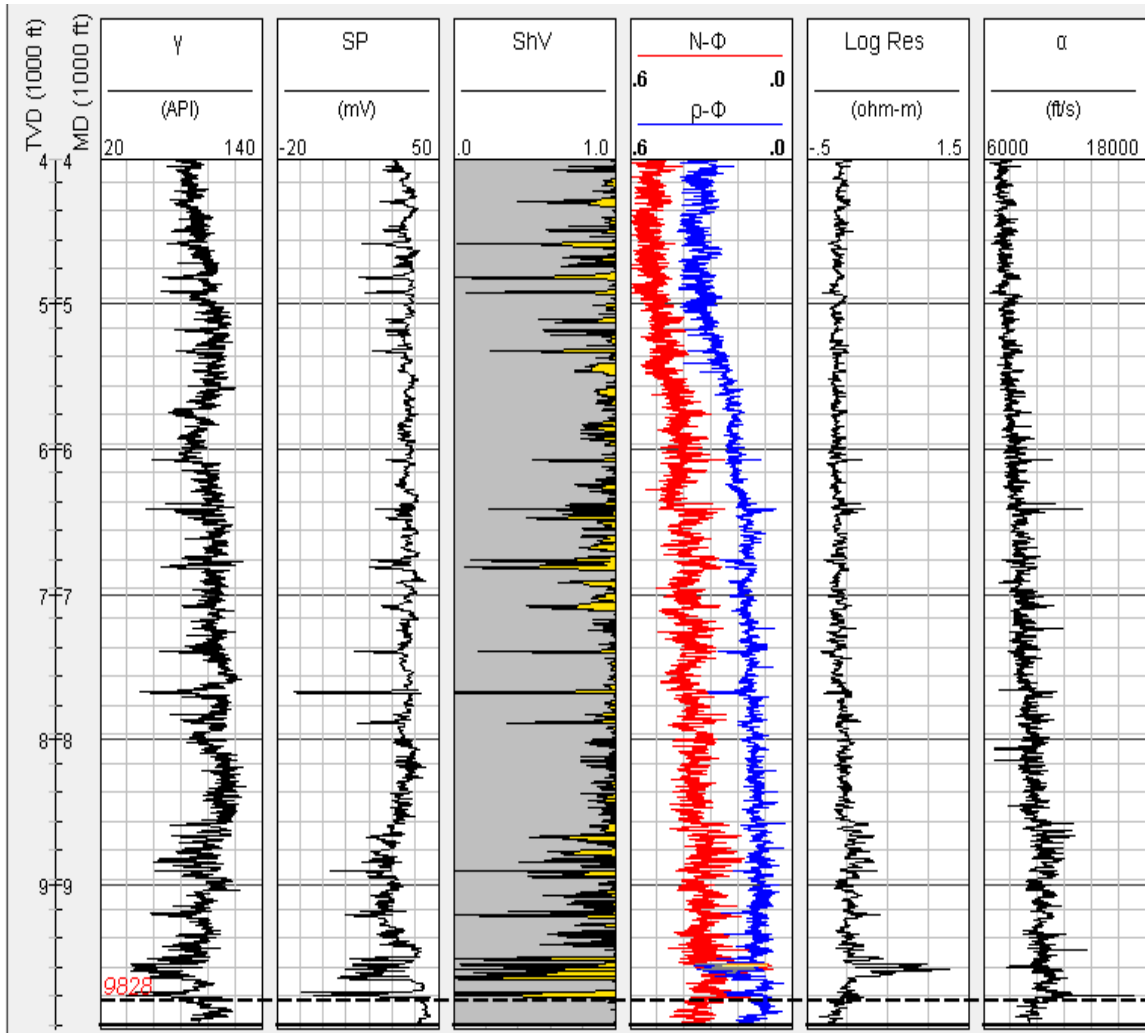
Figure 3.6 Well C well curves. Lithology dominantly shale with thin sand interbeds. Potential gas bearing formation occurs around 9600 ft.
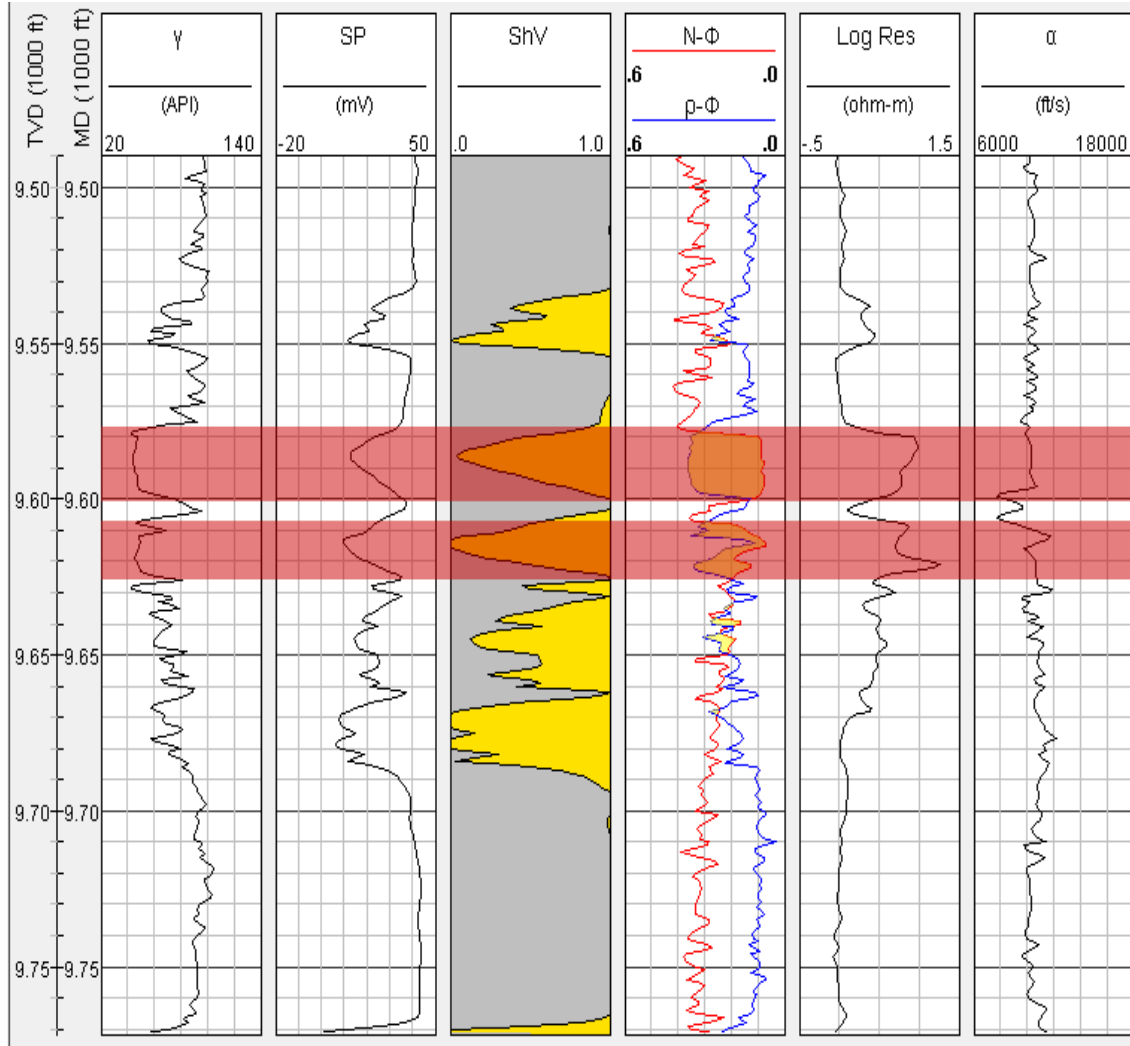
Figure 3.7 Zoomed view of Well C at reservoir level. Similar to Well B, there are at least three potential hydrocarbon rich sands at around 9600 ft., with at most 40 ft. of net thickness.
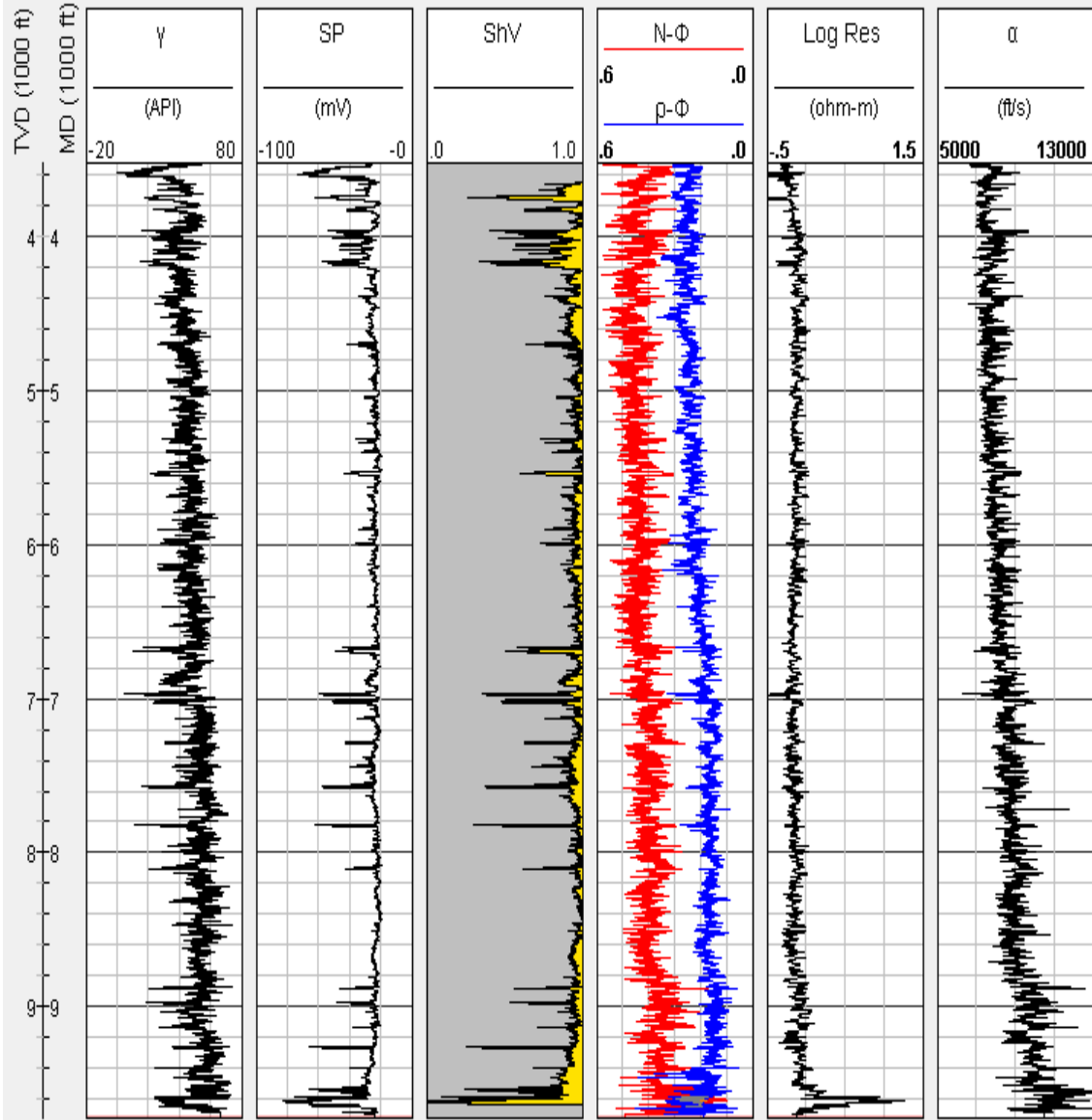
Figure 3.8 Well D well curves. Lithology dominantly shale with thin sand interbeds. Potential gas bearing formation occurs around 9600 ft.
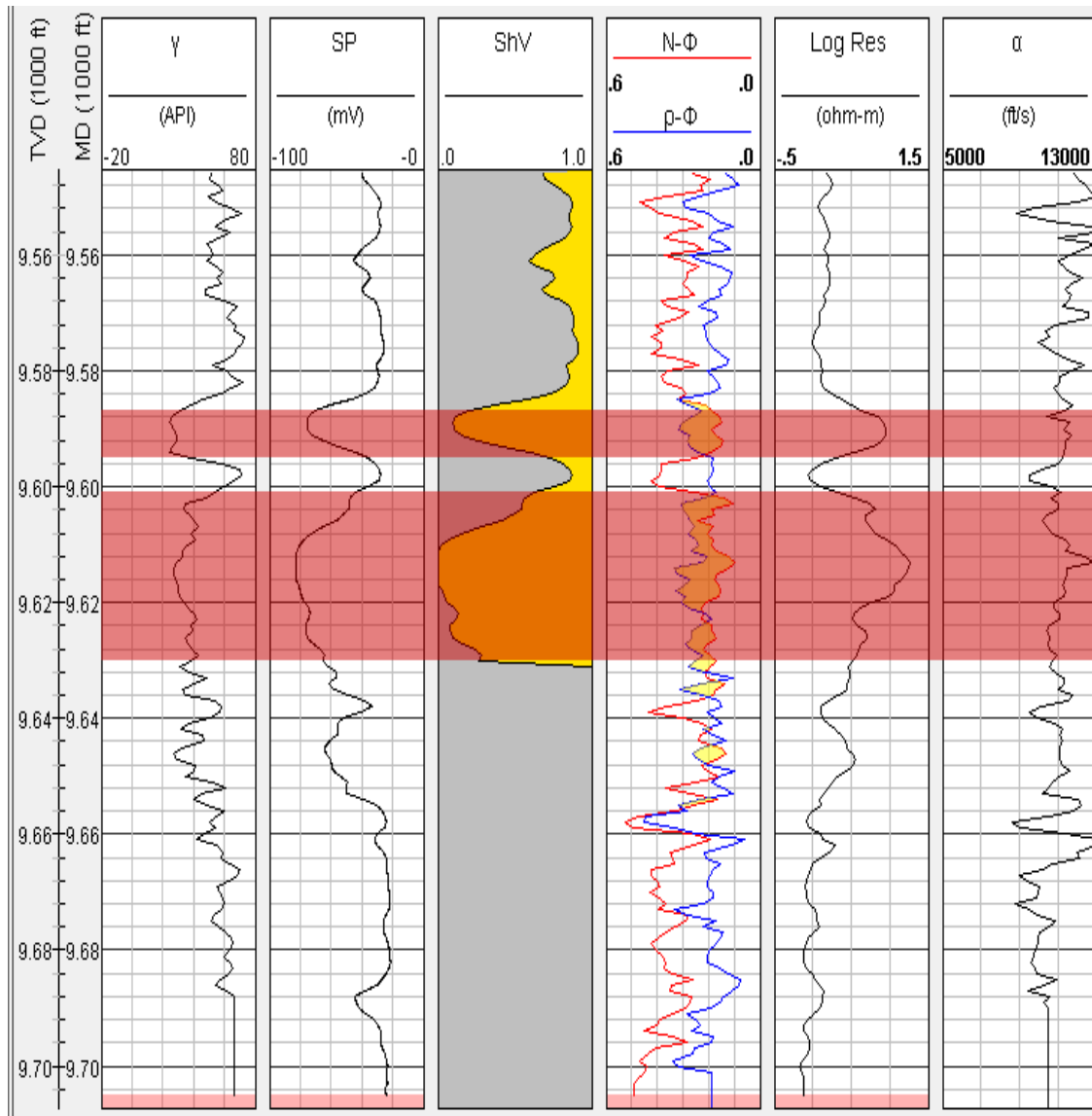
Figure 3.9 Zoomed view of Well D at reservoir level. Two closely spaced potential reservoir rocks, similar to Wells B and C are between 15-30 feet thick around 9600 ft. depth.
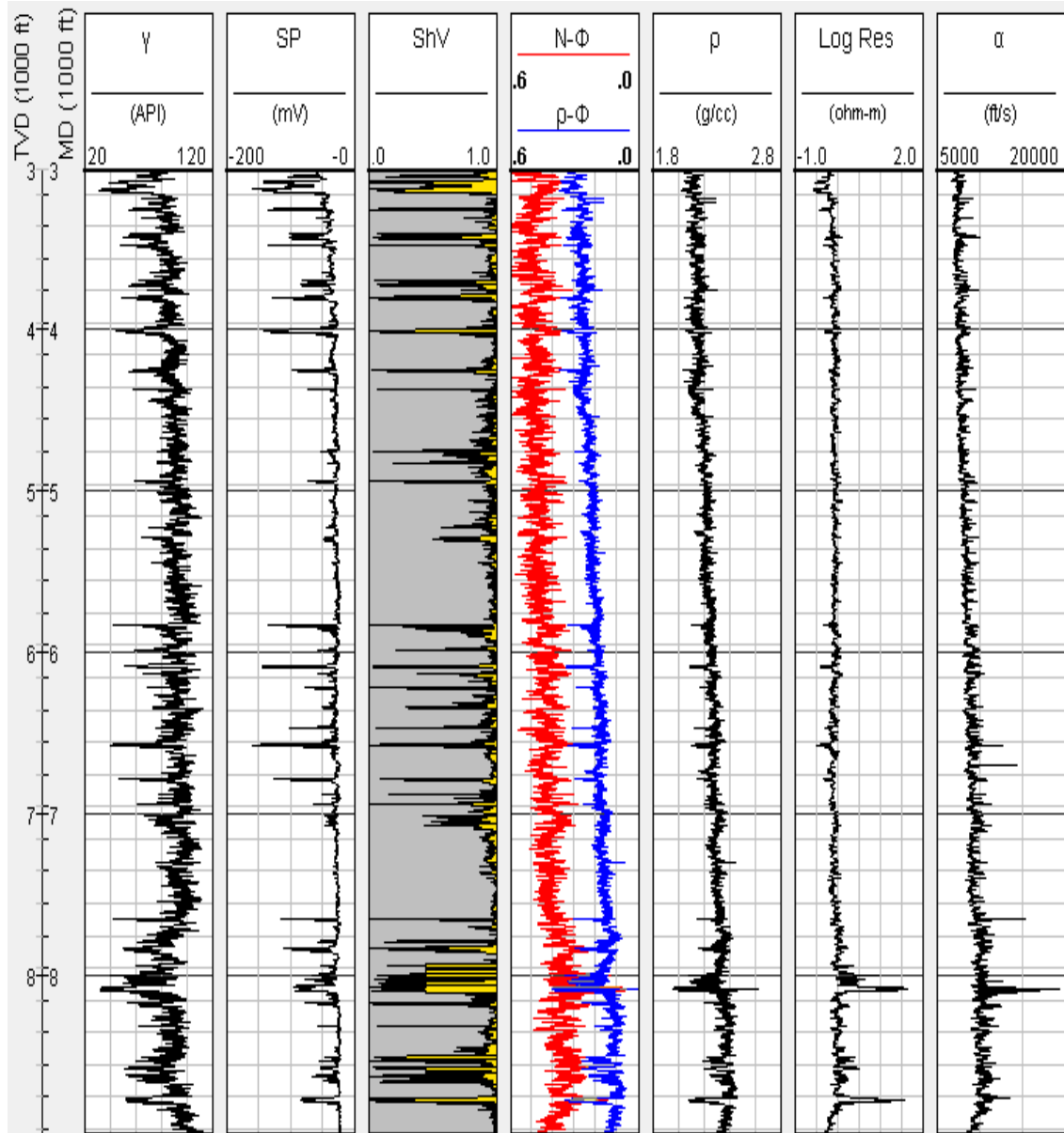
Figure 3.10 Well E well curves. Lithology dominantly shale with thin sand interbeds.
Potential gas bearing formations occur around 8100 and 8800 ft.
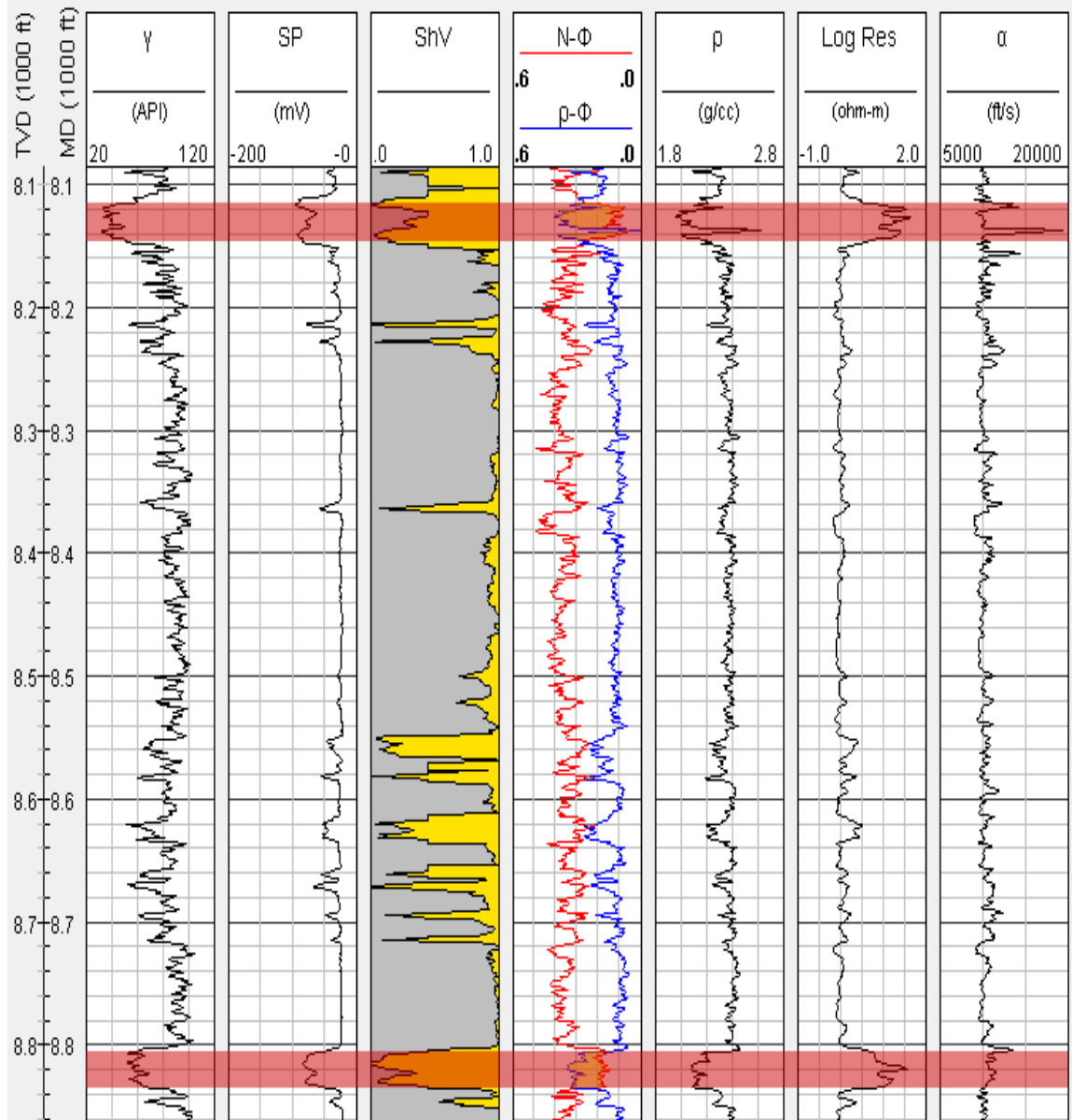
Figure 3.11 Zoomed view of Well E at reservoir level. Unlike previous wells with collocated reservoirs, this location has evidence of two formations with noticeable separation at 8100 ft. and 8800 ft. depth. Both potential reservoirs are between 30-40 feet thick.

3.2 Well-log Interpretation

3.2.1 Lithology and Fluid Determination

Before proceeding with the sand percentage curves, I generated a crossplot using the full depth range in wells A, B, and C in Figure 3.12 with respect to the gamma ray curve as a QC to determine the validity of the sand percentage curve. Except for Well A, there was a slight cloud of uncertainty, but still a good general trend towards higher sand percentage with a lower gamma ray index. When compared to spontaneous potential, the same curves showed a much cleaner correlation, as seen in Figure 3.13. For this experiment, I took the sand percentage as a general guide on whether a unit is sand or shale dominated as an initial view.

In Figure 3.14, the p-impedance and density curves from Well B were crossplotted in jTIPS to highlight different lithology and pore-fluid trends over the depth interval 7700-8700 ft. surrounding the reservoir interval. As can be seen on the crossplot, there was some overlap between sand and shale units for this set of attributes. Given this information, an inversion only for acoustic impedance would be insufficient to confidently identify separate sand and shale lithologies, while fluid type could be more readily identified.

I generated shear velocity logs utilizing the Greenberg-Castagna (1992) equations for sand (equation 3.1) and shale (3.2) units using the existing lithology log to define the sand and shale content.

$$Vs(sand)(\tfrac{ft}{s}) = -2807.7(\tfrac{ft}{s}) + 0.804*Vp(sand)(\tfrac{ft}{s}) \qquad (3.1)$$

$$Vs(shale)(\tfrac{ft}{s}) = -2845.8(\tfrac{ft}{s}) + 0.770*Vp(shale)(\tfrac{ft}{s}) \qquad (3.2)$$

With shear velocity derived, shear impedance logs were generated in jTIPS, allowing p-impedance and s-impedance to be cross plotted to illustrate the effectiveness of AI vs. SI as a lithology indicator (Figure 3.15). There was a more prominent demarcation between these sand and shale trends than was exhibited on the acoustic impedance vs. density crossplot. At this scale, there was also a noteworthy separation in the sand trend between brine and gas saturation. To better separate the two lithology trends, however, other attributes and crossplots would prove to be more suitable.

Utilizing the known velocity and density information, other elastic attributes could be calculated as summarized in Table 3.1.

	Young's modulus, E	Poisson's ratio, σ	Bulk modulus, k	Shear modulus, μ	Lamé constant, λ	P-wave velocity, α	S-wave velocity, β	Velocity ratio, β/α
(E, σ)			$\dfrac{E}{3(1-2\sigma)}$	$\dfrac{E}{2(1+\sigma)}$	$\dfrac{E\sigma}{(1+\sigma)(1-2\sigma)}$	$\left[\dfrac{E(1-\sigma)}{(1+\sigma)(1-2\sigma)\rho}\right]^{1/2}$	$\left[\dfrac{E}{2(1+\sigma)\rho}\right]^{1/2}$	$\left[\dfrac{1-2\sigma}{2(1-\sigma)}\right]^{1/2}$
(E, k)		$\dfrac{3k-E}{6k}$		$\dfrac{3kE}{9k-E}$	$3k\left(\dfrac{3k-E}{9k-E}\right)$	$\left[\dfrac{3k(3k+E)}{\rho(9k-E)}\right]^{1/2}$	$\left[\dfrac{3kE}{(9k-E)\rho}\right]^{1/2}$	$\left(\dfrac{E}{3k+E}\right)^{1/2}$
(E, μ)		$\dfrac{E-2\mu}{2\mu}$	$\dfrac{\mu E}{3(3\mu-E)}$		$\mu\left(\dfrac{E-2\mu}{3\mu-E}\right)$	$\left[\dfrac{\mu(4\mu-E)}{(3\mu-E)\rho}\right]^{1/2}$	$\left(\dfrac{\mu}{\rho}\right)^{1/2}$	$\left(\dfrac{3\mu-E}{4\mu-E}\right)^{1/2}$
(σ, k)	$3k(1-2\sigma)$			$\dfrac{3k}{2}\left(\dfrac{1-2\sigma}{1+\sigma}\right)$	$3k\left(\dfrac{\sigma}{1+\sigma}\right)$	$\left[\dfrac{3k(1-\sigma)}{\rho(1+\sigma)}\right]^{1/2}$	$\left[\dfrac{3k}{2\rho}\left(\dfrac{1-2\sigma}{1+\sigma}\right)\right]^{1/2}$	$\left[\dfrac{1-2\sigma}{2(1-\sigma)}\right]^{1/2}$
(σ, μ)	$2\mu(1+\sigma)$		$\dfrac{2\mu(1+\sigma)}{3(1-2\sigma)}$		$\mu\left(\dfrac{2\sigma}{1-2\sigma}\right)$	$\left[\left(\dfrac{2\mu}{\rho}\right)\left(\dfrac{1-\sigma}{1-2\sigma}\right)\right]^{1/2}$	$\left(\dfrac{\mu}{\rho}\right)^{1/2}$	$\left[\dfrac{1-2\sigma}{2(1-\sigma)}\right]^{1/2}$
(σ, λ)	$\lambda\dfrac{(1+\sigma)(1-2\sigma)}{\sigma}$		$\lambda\left(\dfrac{1+\sigma}{3\sigma}\right)$	$\lambda\left(\dfrac{1-2\sigma}{2\sigma}\right)$		$\left[\left(\dfrac{\lambda}{\rho\sigma}\right)(1-\sigma)\right]^{1/2}$	$\left[\dfrac{\lambda}{\rho}\left(\dfrac{1-2\sigma}{2\sigma}\right)\right]^{1/2}$	$\left[\dfrac{1-2\sigma}{2(1-\sigma)}\right]^{1/2}$
(k, μ)	$\dfrac{9k\mu}{3k+\mu}$	$\dfrac{3k-2\mu}{2(3k+\mu)}$			$k-2\mu/3$	$\left(\dfrac{k+4\mu/3}{\rho}\right)^{1/2}$	$\left(\dfrac{\mu}{\rho}\right)^{1/2}$	$\left(\dfrac{\mu}{k+4\mu/3}\right)^{1/2}$
(k, λ)	$9k\left(\dfrac{k-\lambda}{3k-\lambda}\right)$	$\dfrac{\lambda}{3k-\lambda}$		$\dfrac{3}{2}(k-\lambda)$		$\left(\dfrac{3k-2\lambda}{\rho}\right)^{1/2}$	$\left[\dfrac{3(k-\lambda)}{2\rho}\right]^{1/2}$	$\left[\dfrac{1}{2}\left(\dfrac{k-\lambda}{k-2\lambda/3}\right)\right]^{1/2}$
(μ, λ)	$\mu\left(\dfrac{3\lambda+2\mu}{\lambda+\mu}\right)$	$\dfrac{\lambda}{2(\lambda+\mu)}$	$\lambda+\dfrac{2}{3}\mu$			$\left(\dfrac{\lambda+2\mu}{\rho}\right)^{1/2}$	$\left(\dfrac{\mu}{\rho}\right)^{1/2}$	$\left(\dfrac{\mu}{\lambda+2\mu}\right)^{1/2}$
(α, β)	$\rho\beta^2\left(\dfrac{3\alpha^2-4\beta^2}{\alpha^2-\beta^2}\right)$	$\dfrac{\alpha^2-2\beta^2}{2(\alpha^2-\beta^2)}$	$\rho\left(\alpha^2-\dfrac{4}{3}\beta^2\right)$	$\rho\beta^2$	$\rho(\alpha^2-2\beta^2)$			

Table 3.1 Derivations of elastic moduli. (Sheriff, 1991)

For this research, I made strong use of the Lambda-Rho and Mu-Rho attributes. Goodway et al. (1997) first proposed the Lambda-Mu-Rho (LMR) method as a way to create both a matrix and fluid discriminant with the elastic parameters. In this case, Mu-Rho would be a grain matrix identifier due to the lack of change in rigidity due to fluid change. Inversely, Lambda-Rho was a fluid discriminant due to its susceptibility to change with hydrocarbon saturation. Figures 3.16 and 3.17 show the crossplots for Lambda-Rho vs. Mu-Rho and Lambda-Rho vs. Poisson's ratio plots respectively within jTIPS. Lithology discrimination using LMR plots and Poisson's ratio are shown to be potentially more effective for both fluid discrimination and rock type classification in comparison to acoustic impedance. Overall, the well log data suggested that lithology

and fluid content can be determined with confidence in this geologic setting given the right set of elastic attributes.
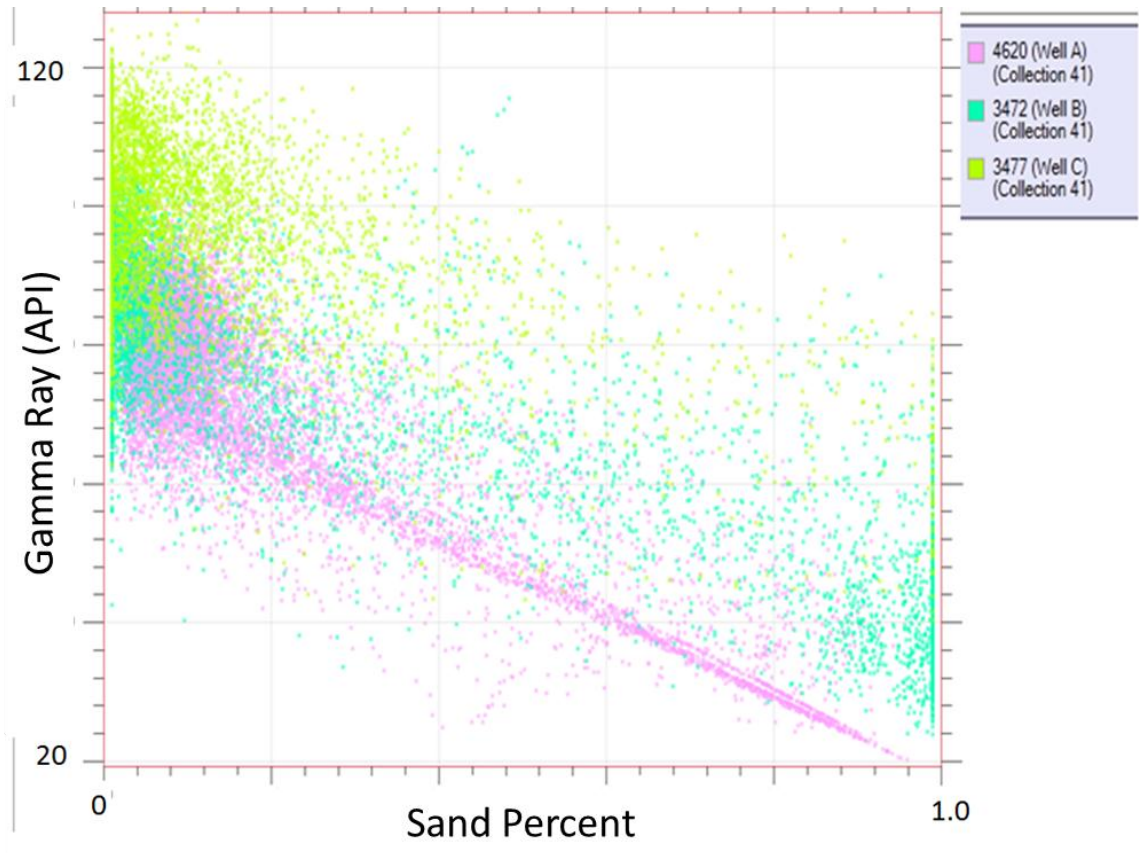

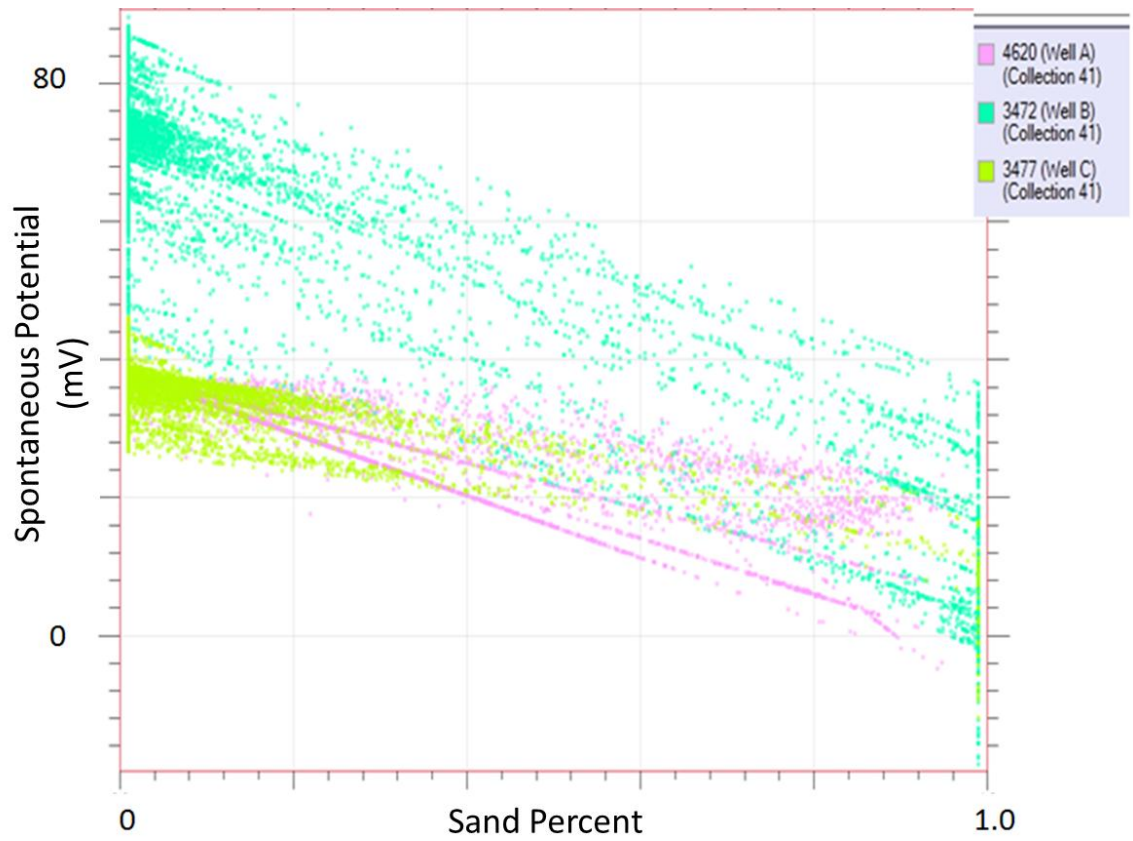Figure 3.12 Crossplot of Gamma Ray and Sand Composition Logs for Wells A, B, and C.

Figure 3.13 Crossplot of Spontaneous Potential and Sand Composition Logs for Wells A, B, and C. This combination yields a fairly linear relationship between SP and sand percentage logs.
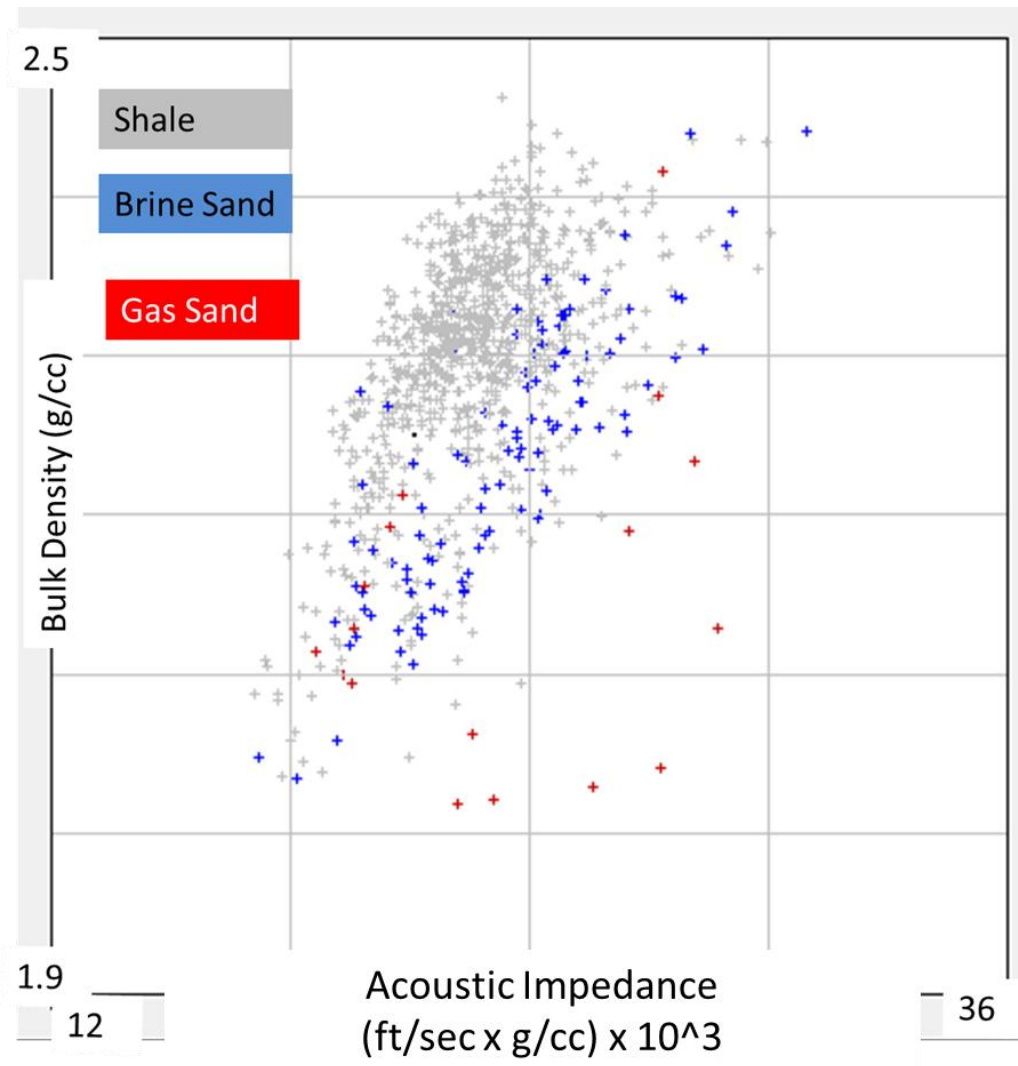
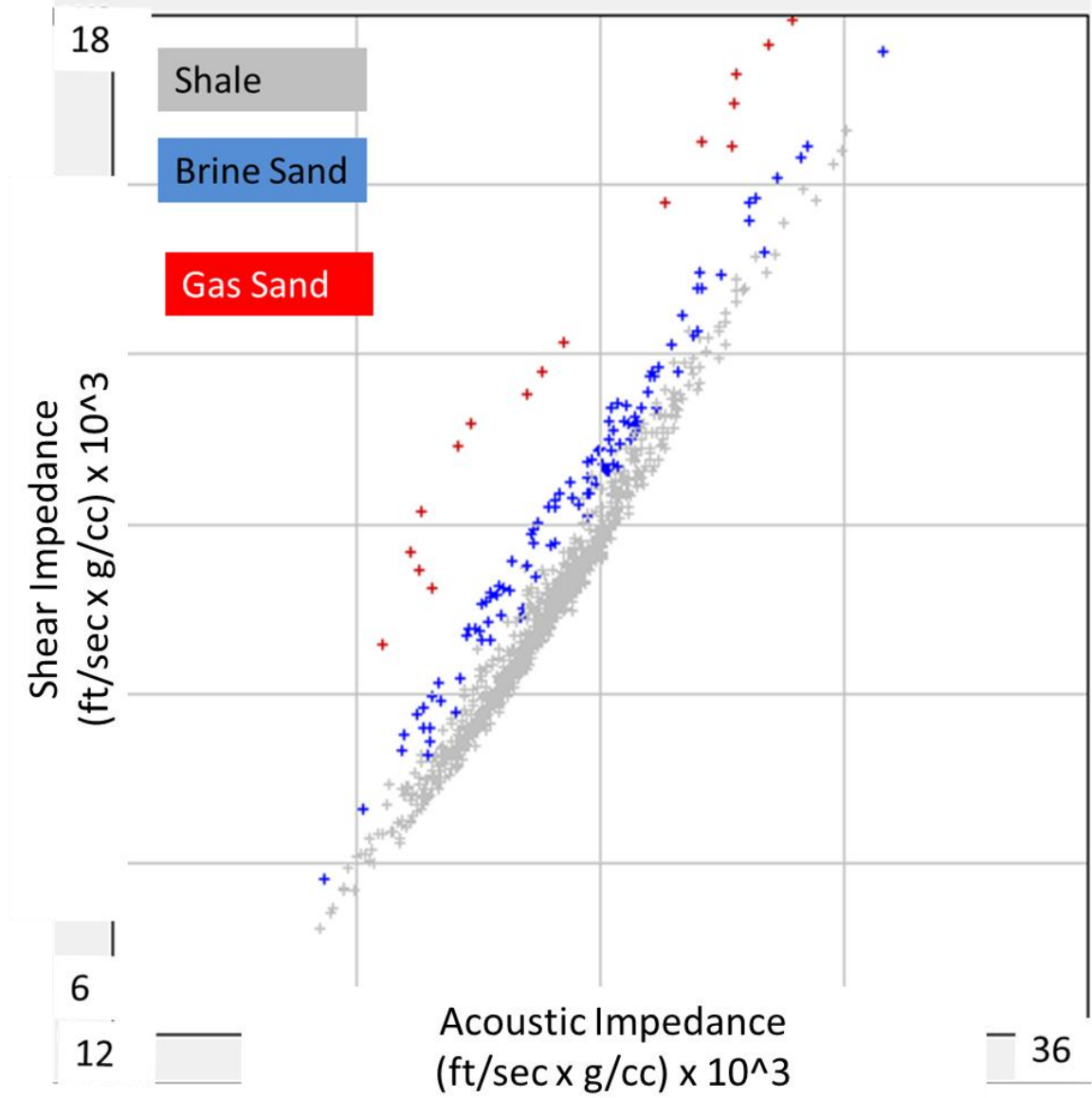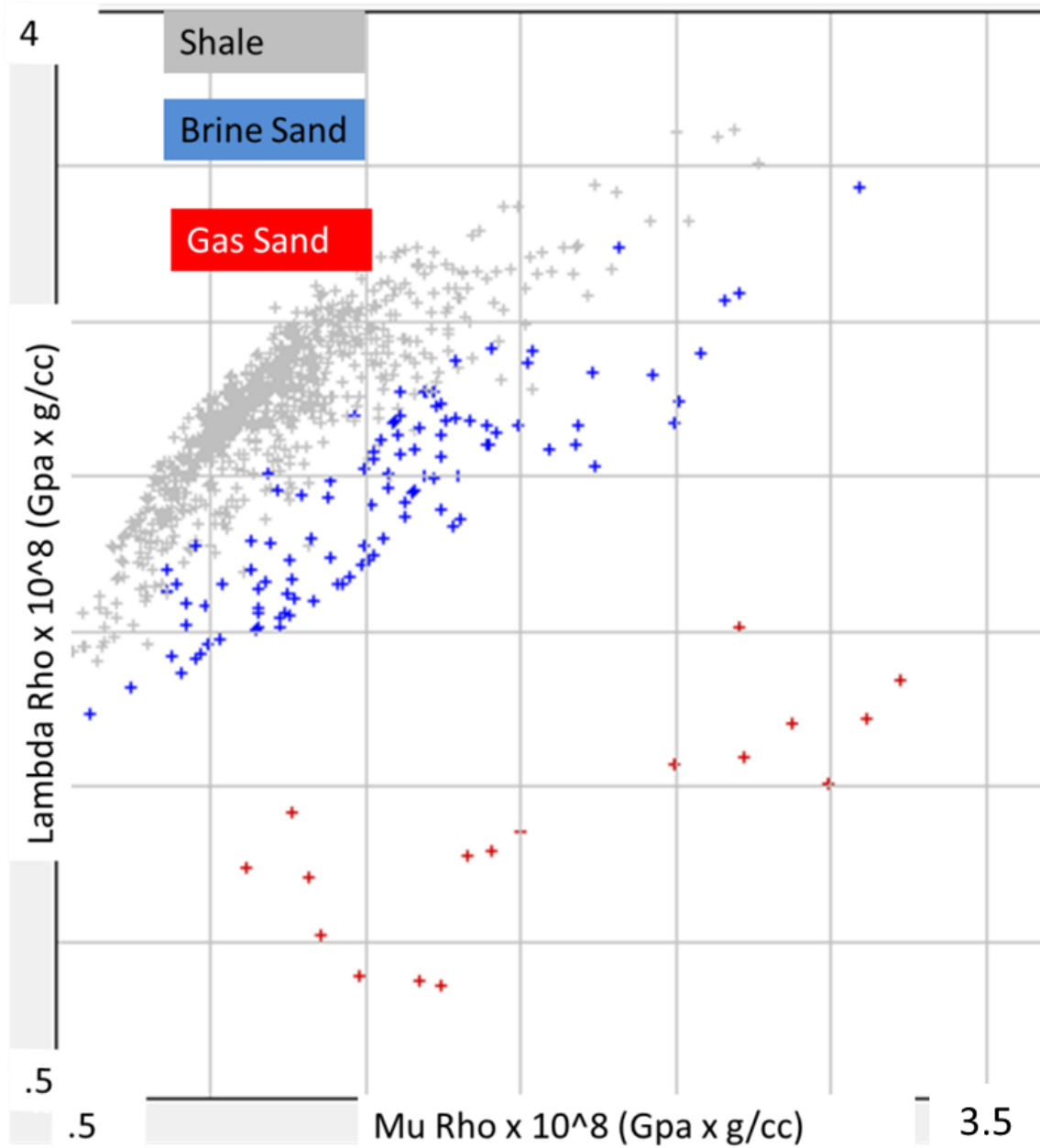Figure 3.14 P-impedance vs. density crossplot from Well B using jTIPS.

Figure 3.15 Well A P-Impedance vs. Shear Impedance.

Figure 3.16 Well A Mu-Rho vs Lambda-Rho. Brine Sand vs. Shale discrimination is improved over the previous acoustic impedance and density plot. Sands with gas saturation directly correlate with a large drop in Lambda Rho and a consistent Mu Rho as compared to brine saturated sands.
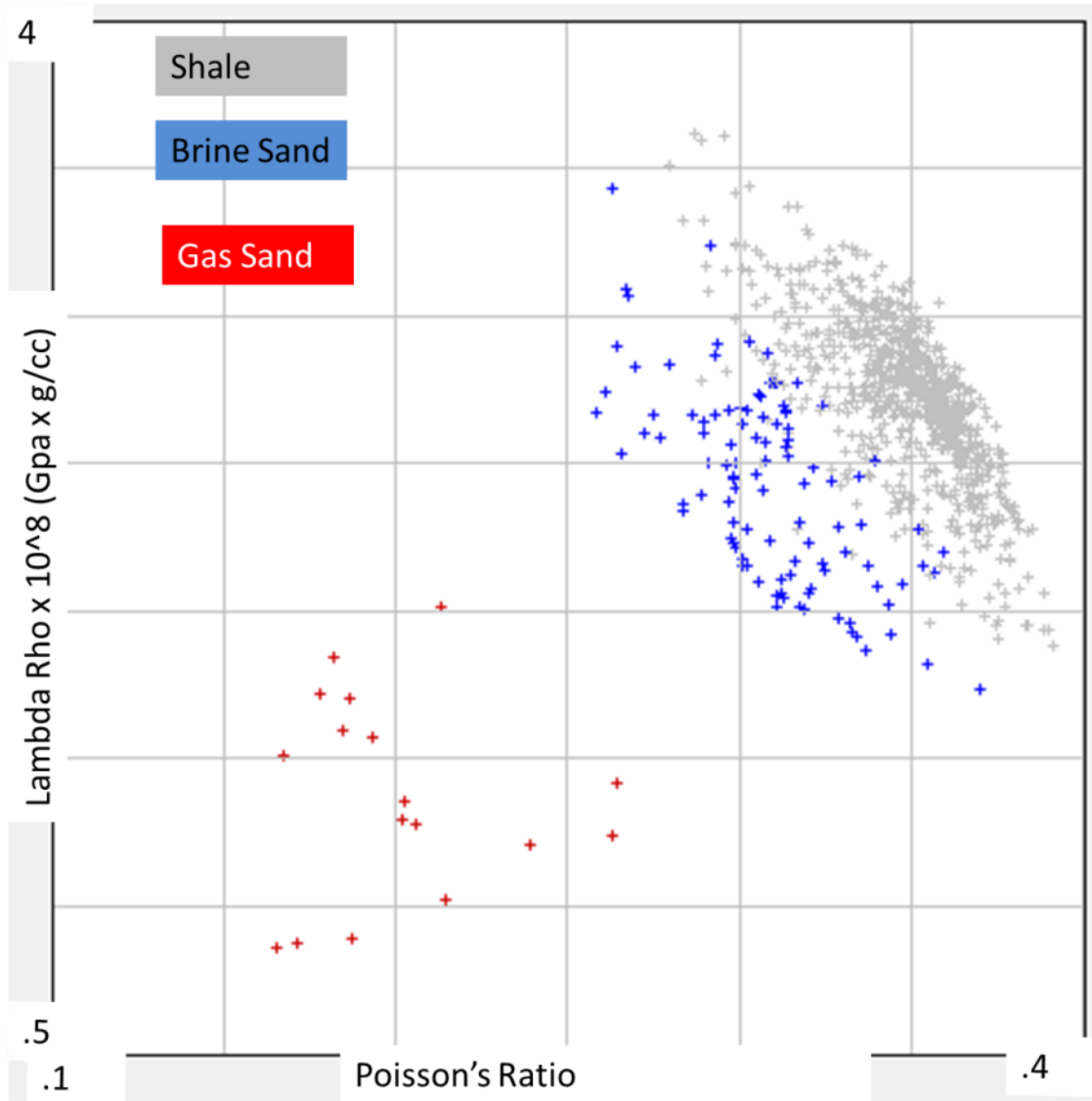
Figure 3.17 Well A Poisson's ratio vs Lambda-Rho. Similar to Lambda-Rho and Mu-Rho, Poisson's ratio readily identifies gas sand saturation with a shared lower value in Poisson's ratio and Lambda-Rho. Brine sands show a slightly lower Poisson's ratio versus the background Shale trend as well.

3.2.2 Reservoir Porosity

As a measure of hydrocarbon saturation, seismic amplitude and acoustic impedance attributes do not adequately distinguish between economic and "fizz"

saturations. Further risk is derived from the potential that an amplitude change is due to rock properties rather than fluid content, such as rock type or porosity changes within a layer. To mitigate risk in the interpretation of these factors, I utilized the existing logs to estimate rock properties for each reservoir layer at each well location.

The first rock property I sought to evaluate was the reservoir porosity, the amount of void space in a rock. Although this is not necessarily measured directly by a specific well sonde in the available datasets, the total porosity is generally estimated by,

$$\Phi = (\rho_b - \rho_m)/(\rho_f - \rho_m) \tag{3.3}$$

where Φ is porosity, ρ_b represents the measured bulk density of the rock, ρ_m represents the grain density of the matrix, and ρ_f represents the density of the pore fluid. In this study, I assumed that sandstone and shale have similar grain densities of 2.65 g/cm^3.

An issue arises, however, when trying to solve for ρ_f, the density of pore fluid. In order to accurately determine this factor from the bulk density log, the saturation percentage of gas and water are required.

$$\rho_f = (1 - Sw)\rho_{gas} + Sw(\rho_{water})$$

$$(3.4)$$

where $\rho_{gas} = 0.29$ g/cm^3 and $\rho_{water} = 1.09$ g/cm^3 were estimated from the Batzle and Wang equations (1992). At the same time, as will be shown later, water saturation often requires that the porosity is known. To get around this, an estimate was made using both the density and neutron porosity logs. A crossover effect occurs due to gas saturation

increasing the porosity estimate in the density log and decreasing the porosity estimate in the neutron log. The recommended empirical approach for finding porosity is

$$\Phi = \sqrt{(\Phi_{neutron})^2 + (\Phi_{density})^2/2} \qquad (3.5)$$

One important note is that this calculated value was only valid for gas bearing units, and that the bulk density derived porosity was more correct for brine pore-fluid saturations.

The general trend of porosity across all five wells is from approximately 40% porosity in the shallow sands of Wells A and B, to around 15% porosity in the sub reservoir shale units. Reservoir porosity for Well A is 28%, Well B 29%, Well C 27%, Well D 20%, and Well E 28% for both reservoirs. Since the porosity values are high in the reservoir units, I assumed that the total and effective porosity were approximately the same.

Water saturation (Sw) refers to the fraction of the pore volume filled with formation water. This was primarily determined using the Archie (1952) equation that utilizes porosity and resistivity logs,

$$S_w = (a/\Phi^m * R_w/R_t)^{1/n} \qquad (3.6)$$

where a is a constant, m is the cementation factor, n is the saturation exponent, φ is porosity, R_w is resistivity of formation water, and R_t is the measured resistivity of the formation. A form of this equation is often written in two parts, the first being

$$F = R_o/R_w = a/\Phi^m \qquad (3.7)$$

where F is the Formation Factor and R_o is a brine - saturated rock's expected resistivity. The second part relates the measured resistivity to the expected, brine filled resistivity, as follows

$$R_t/R_o = 1/(S_w)^n \qquad (3.8)$$

In this research, I assumed that $a = 1$, $m = 2$ and $n = 2$. In order to determine Formation Water resistivity, I utilized equation 3.7 in brine sand units above the reservoir and found an average of $R_w = 0.07$ ohm*m. Inserting this value of R_w into Equation 3.6 yielded the following average reservoir water saturation values: Well A - 30%, Well B - 30%, Well C - 32%, Well D - 24%, and Well E - 20% and 15%. Figures 3.18 - 22 display the water saturation curves at the far right in cyan. At these saturation levels, each well was considered to have good quality reservoirs, especially A and E. With the later inversion work, the horizontal extent of these reservoirs helped determine the most economic pay.
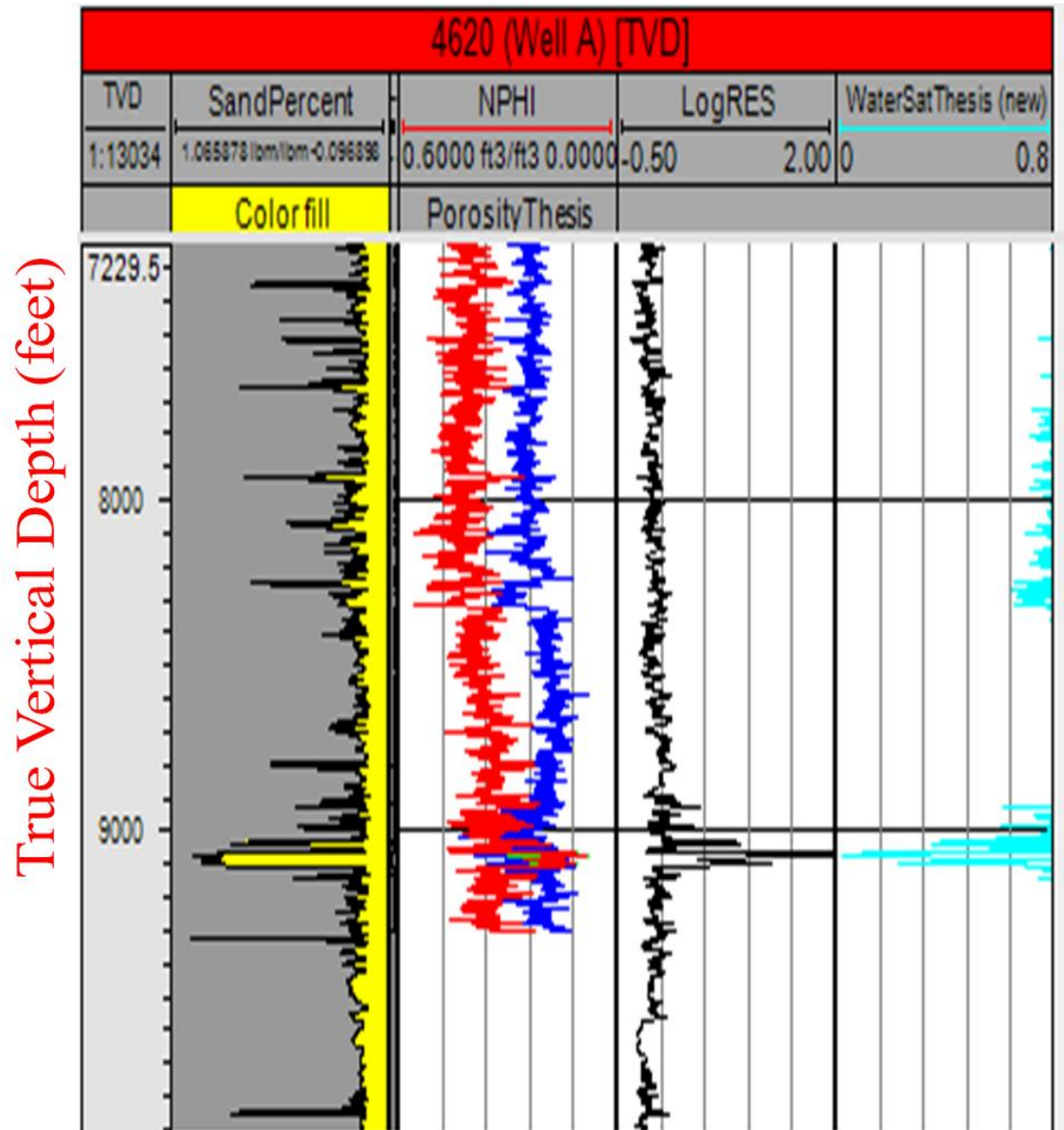
Figure 3.18 Well A well-log curves with water saturation estimation.
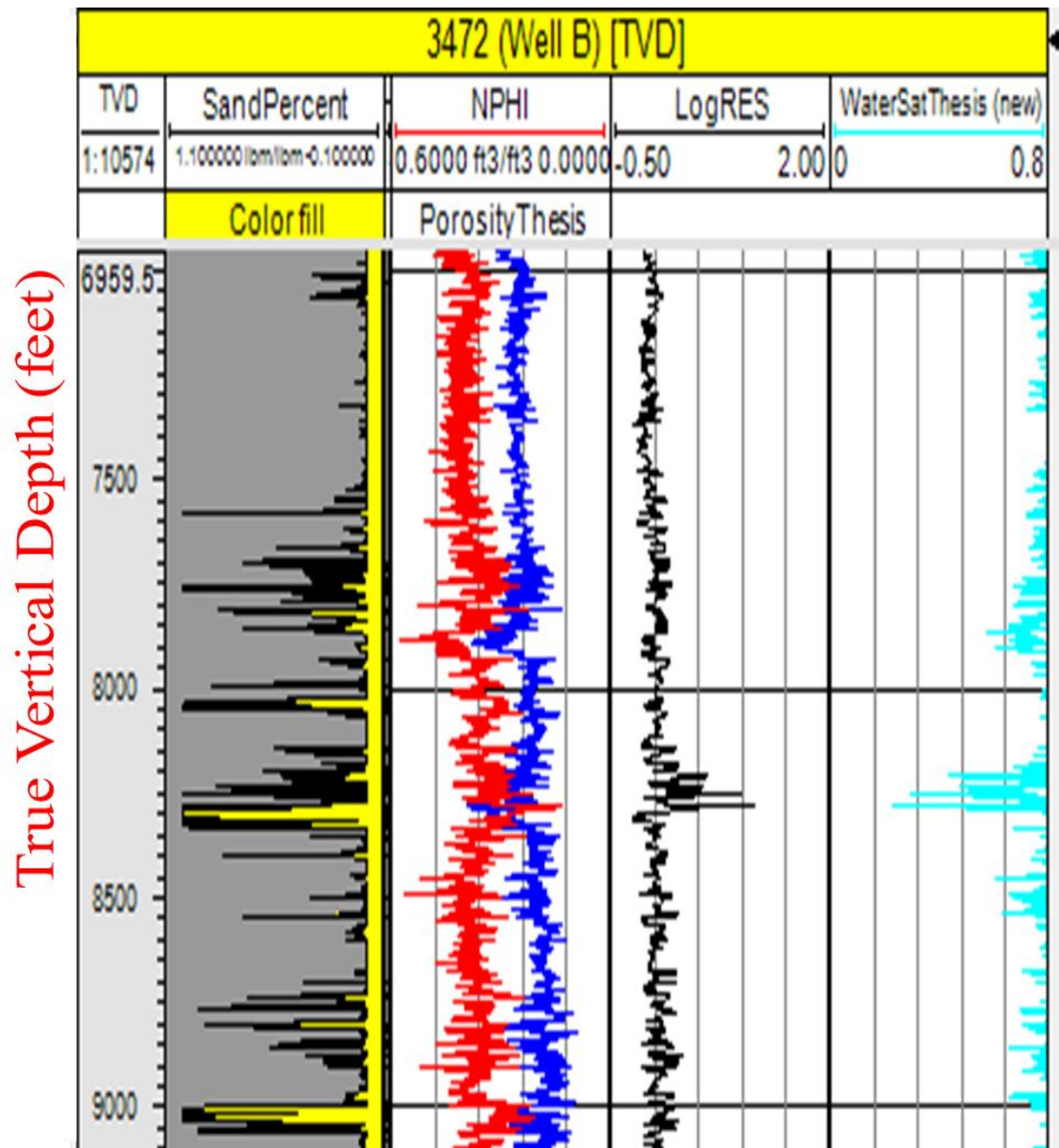
Figure 3.19 Well B water saturation estimation.
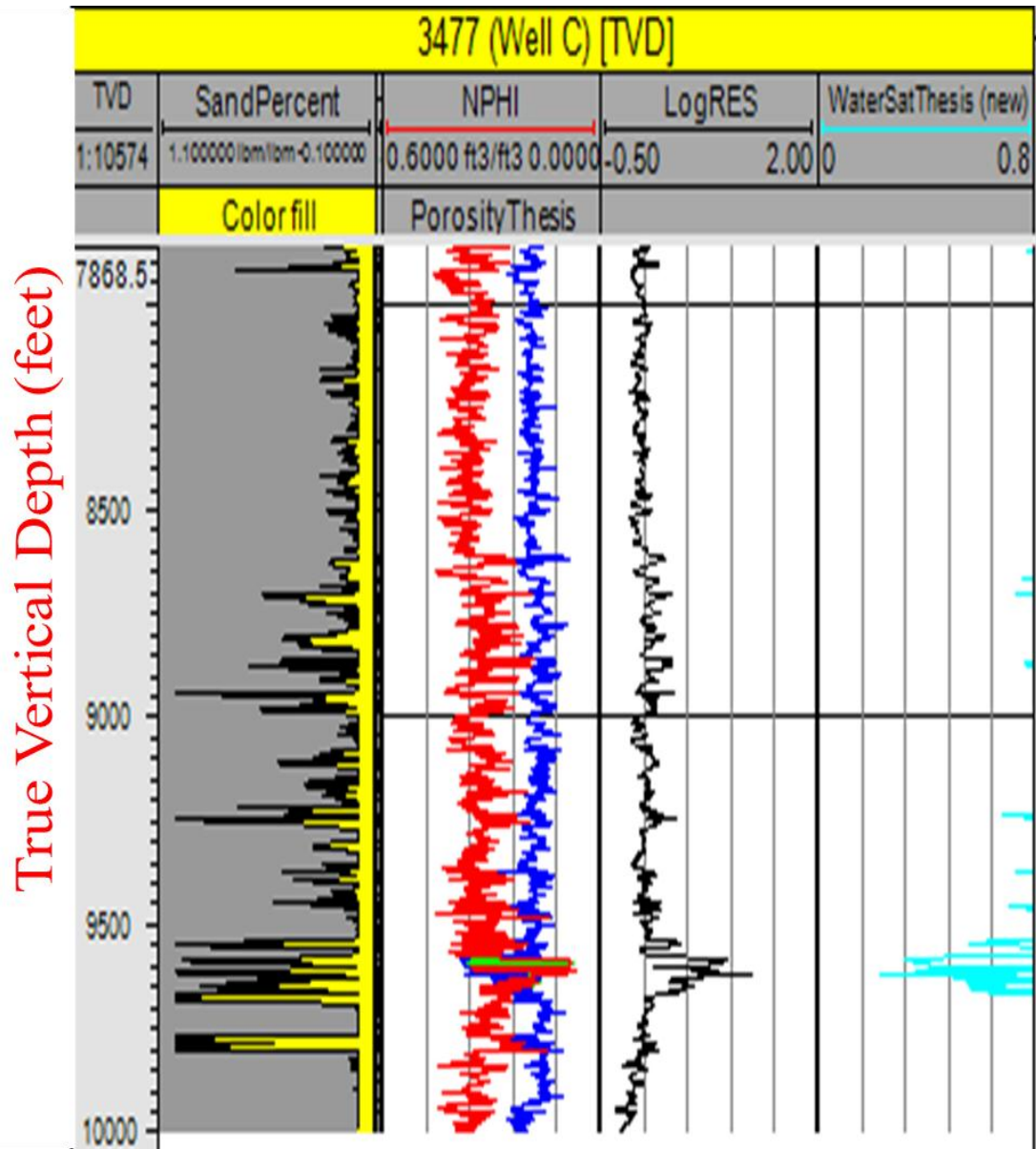
Figure 3.20 Well C water saturation estimation.
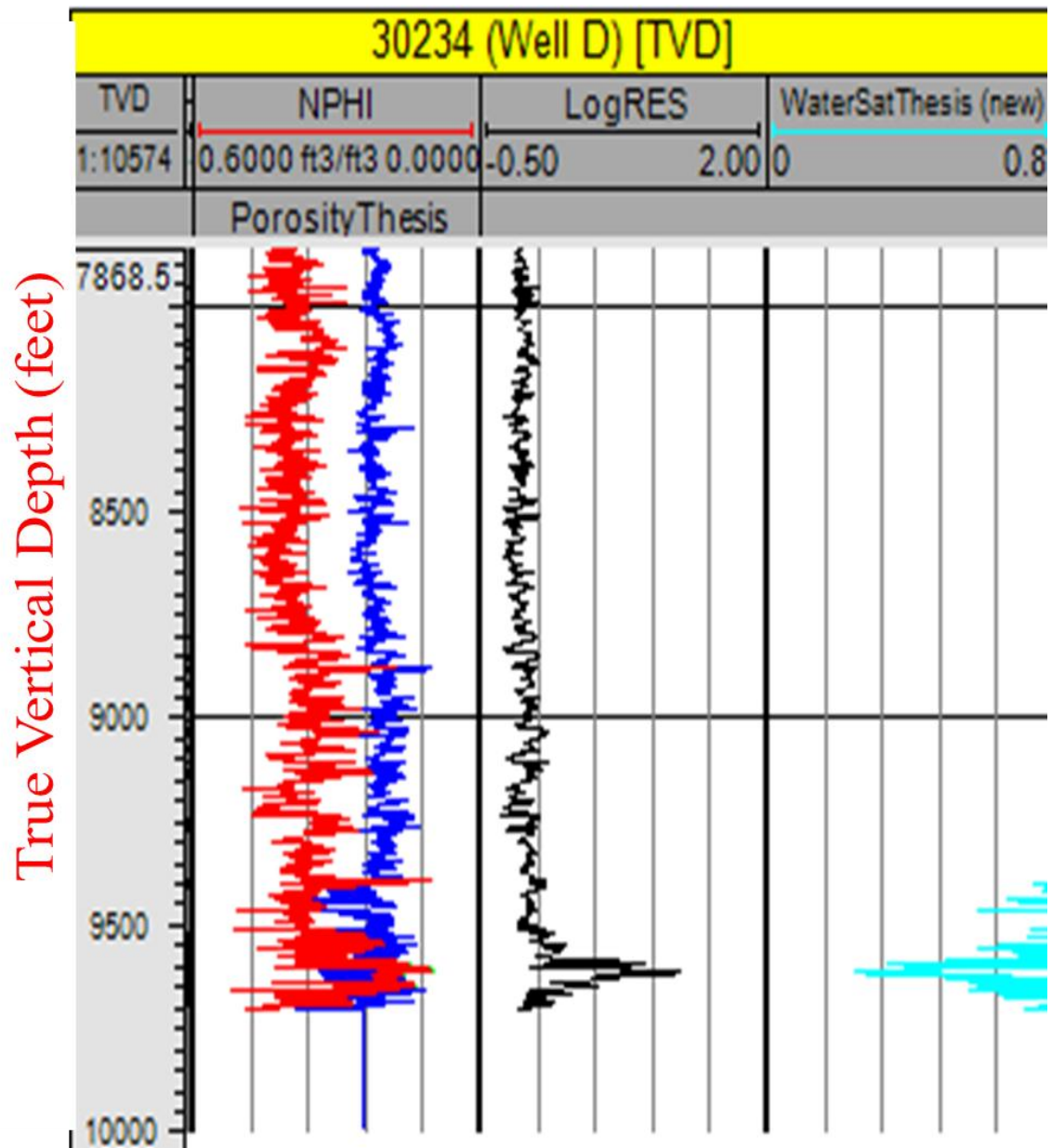
Figure 3.21 Well D water saturation estimation.
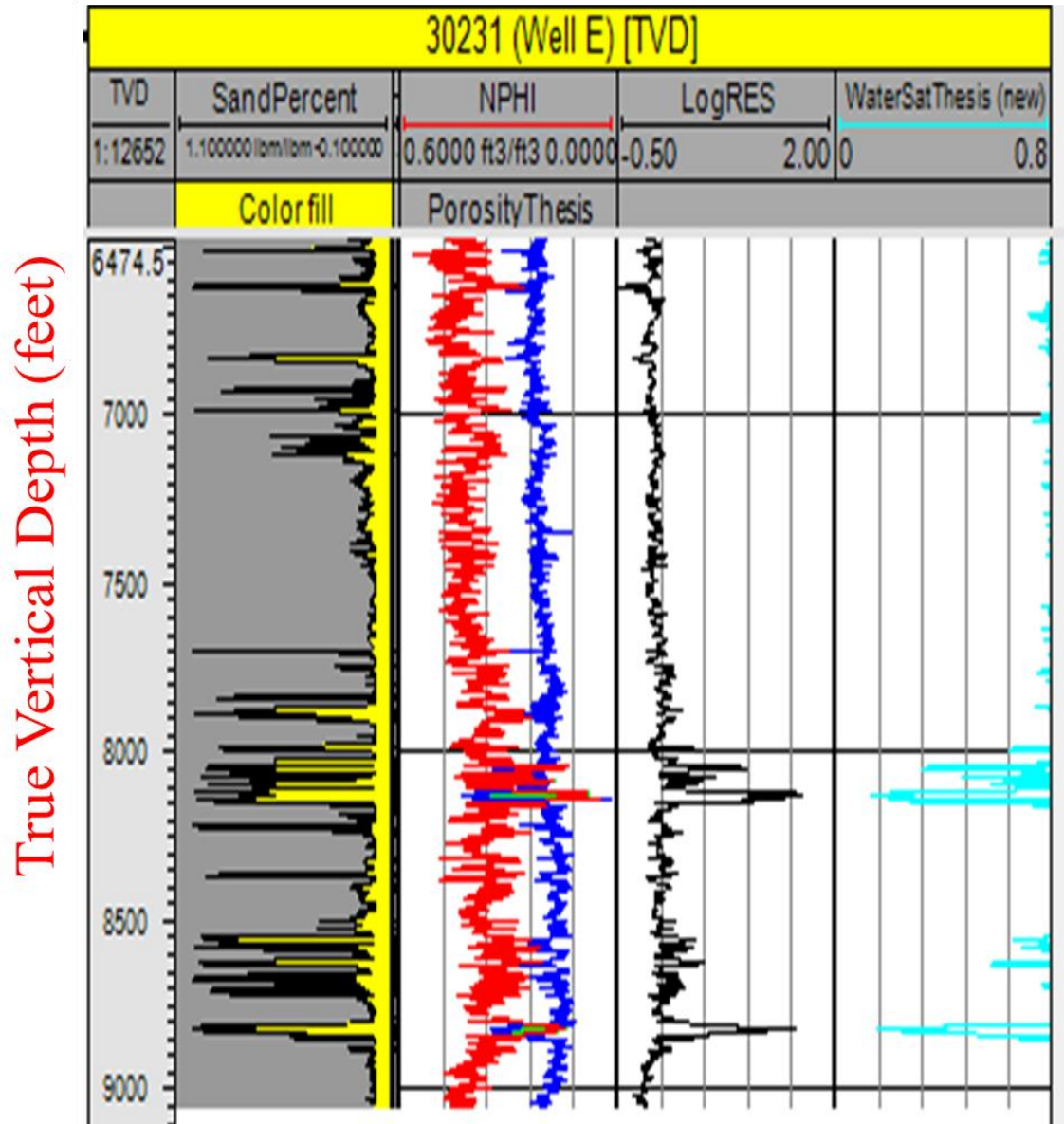
Figure 3.22 Well E water saturation estimation.

3.3 Seismic-well Tie

To match the well-log data, which is recorded in depth, to the seismic data, which is in time, I utilized the well-tie process in Petrel. By correlating events between depth

and time, the initial petrophysical model can be built for the inversion process, as well as assist in the seismic interpretation. This process was accomplished with convolving an input wavelet with a reflectivity series generated from well measurements to generate synthetic seismograms.   The seismograms operate on the assumption that the well trajectory is vertical and that this is an isotropic medium (Liner, 2004). These synthetic sections were then correlated to the field recorded seismic to tie the well and field data.

The first step was to extract a wavelet from the near stack volume (0-25 degrees) at each well location. For the initial well tie process, I used a zero - phase Ricker wavelet convolved with a reflectivity series generated from Backus average blocked acoustic impedance logs generated from the P-wave and density measurements. After accounting for any bulk shift to the datum of the well, I extracted a more detailed wavelet using the Extended White (White, 1997) algorithm. This method works by determining a best fit wavelet given an input reflectivity series and a seismic input, in this case the near-angle stack.   This wavelet was calculated for an inline and crossline range, generally a 10 x 10 section, in the seismic for the specified time window, up to 1 second above the reservoir. The end result is a wavelet with a maximum "Predictability" for the given section. This value was determined by a function of the cross correlation of the predicted and recorded trace and their respective autocorrelations, as shown in the following equation:

$$\text{Predictability} = \frac{\Sigma \; \text{Xcor(t)}^2 * 100}{\Sigma \; (\text{Acor1(t)} * \text{Acor2(t)})}$$

For well A and B, the resulting predictability values were poorer for the near trace results, 0.34 and 0.37 respectively, than for the far trace results, 0.54 and 0.63. To verify the

time-depth relationship, I repeated the wavelet extraction for the far-angle stack volume. Figure 3.23 showcases the initial Ricker wavelet synthetic match around Well B against the near-angle stack. Figure 3.24 displays the synthetic-seismic well tie using the derived wavelet from the near trace volume. Figures 3.25 displays the wavelet extraction results for the far angle stack for Well B. Figures 3.26-3.28 display the results at Well A, which has a similar extracted wavelet for the near angle stack, but noticeable differences with the far angle wavelet. Overall, the match at Well A may be less precise than Well B due to the lack of input data for the extraction window, as Well A was at the edge of the survey limits. Due to the similar acoustic impedance between sand and shale formations in this study area, the extracted wavelet for the near angle stack was more noise contaminated given the expected reflection coefficients and provided data. However, the far angle wavelets were generally less noise influenced as the sand-shale units were distinguished by changes in amplitude due to lithology variations at larger angles of incidence.
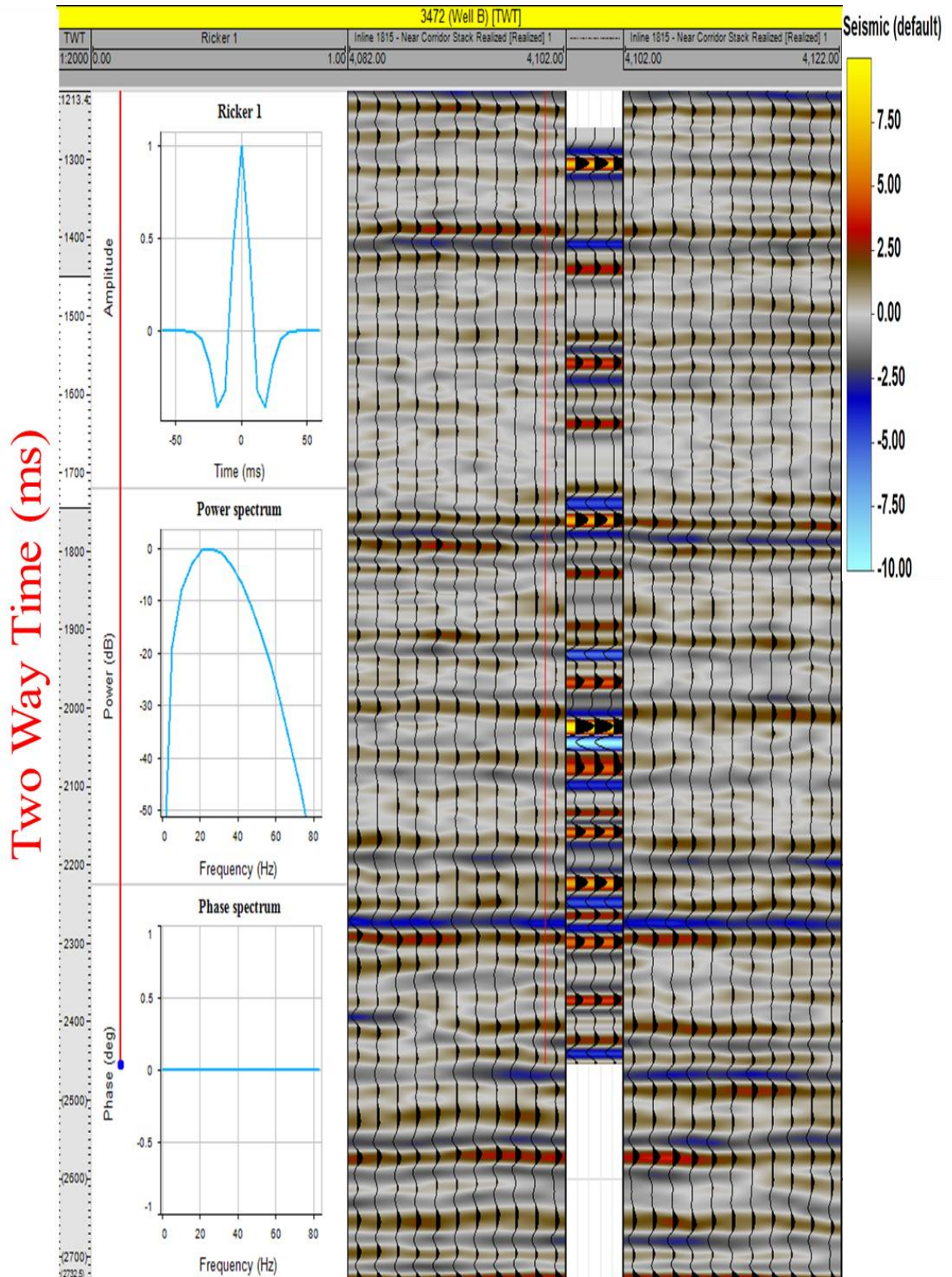
Figure 3.23 Well B Seismic-well tie using a zero-phase Ricker wavelet. Reservoir located at approximately 2300 ms.
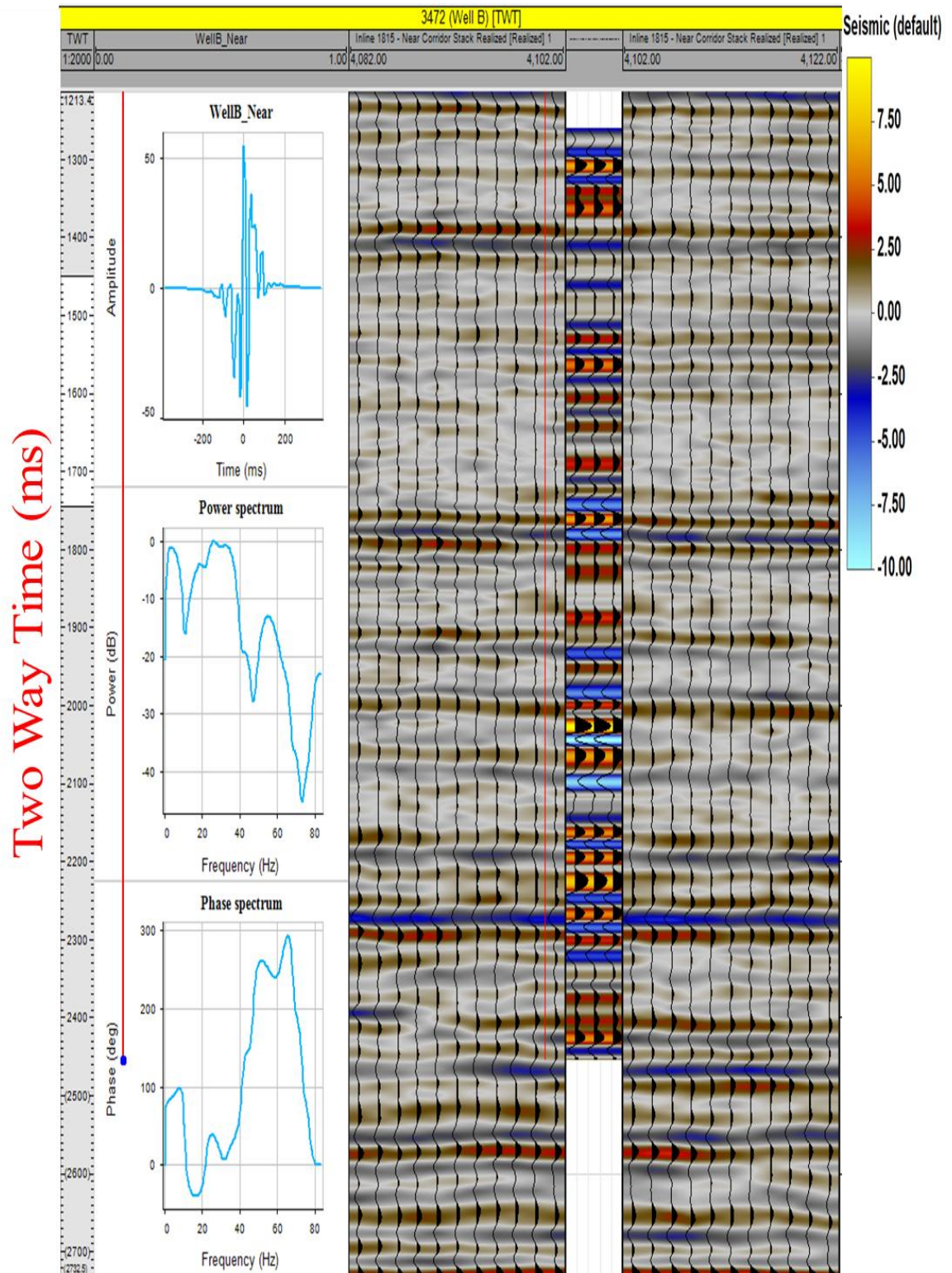
Figure 3.24 Well B Seismic-well tie using the extracted wavelet from the near angle stack. The overall match is maintained when compared to the Ricker wavelet
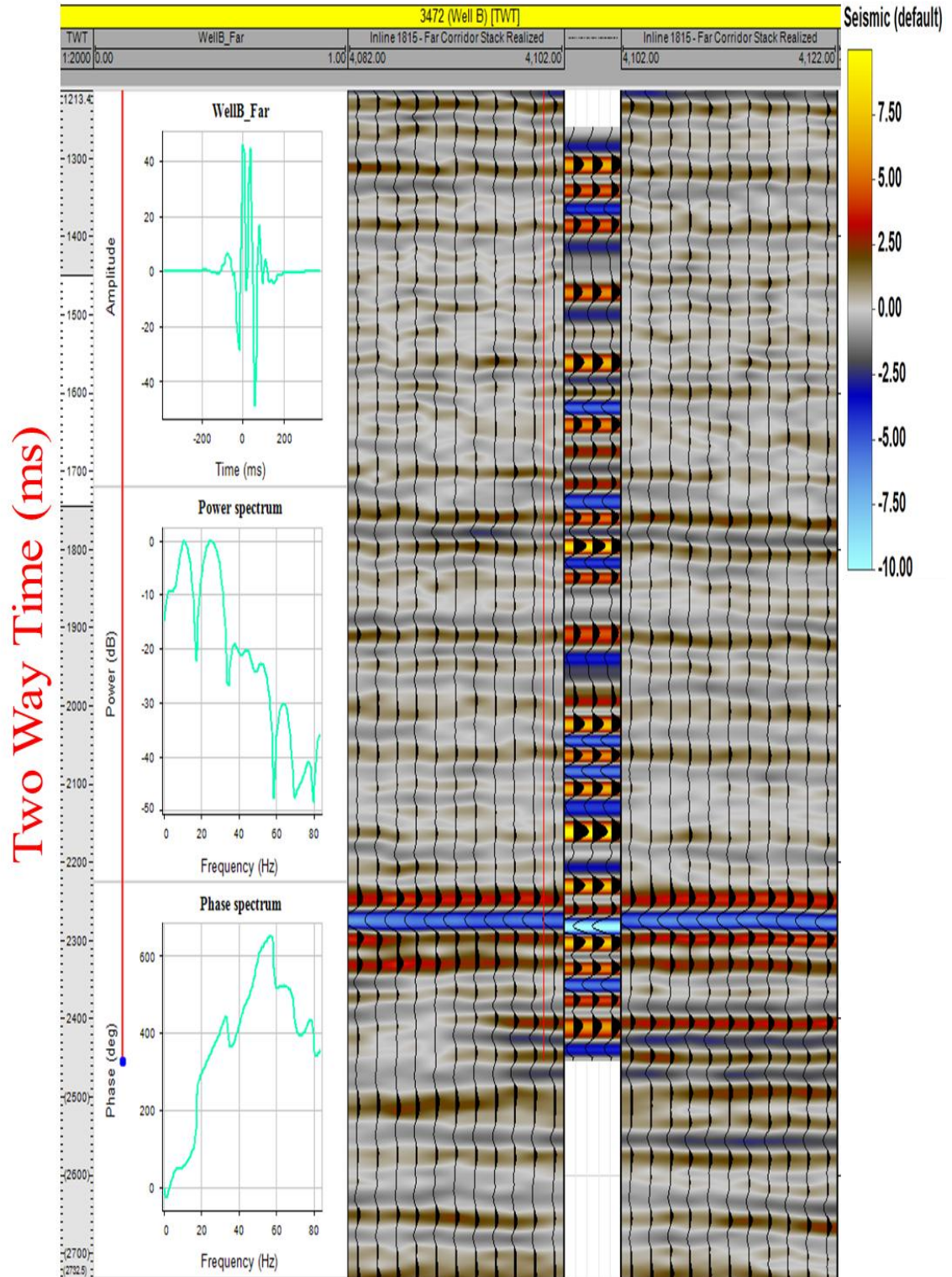
Figure 3.25 Well B Seismic-well tie using the extracted wavelet from the far angle stack. Reservoir is more apparent at this farther angle at approximately 2300 ms.
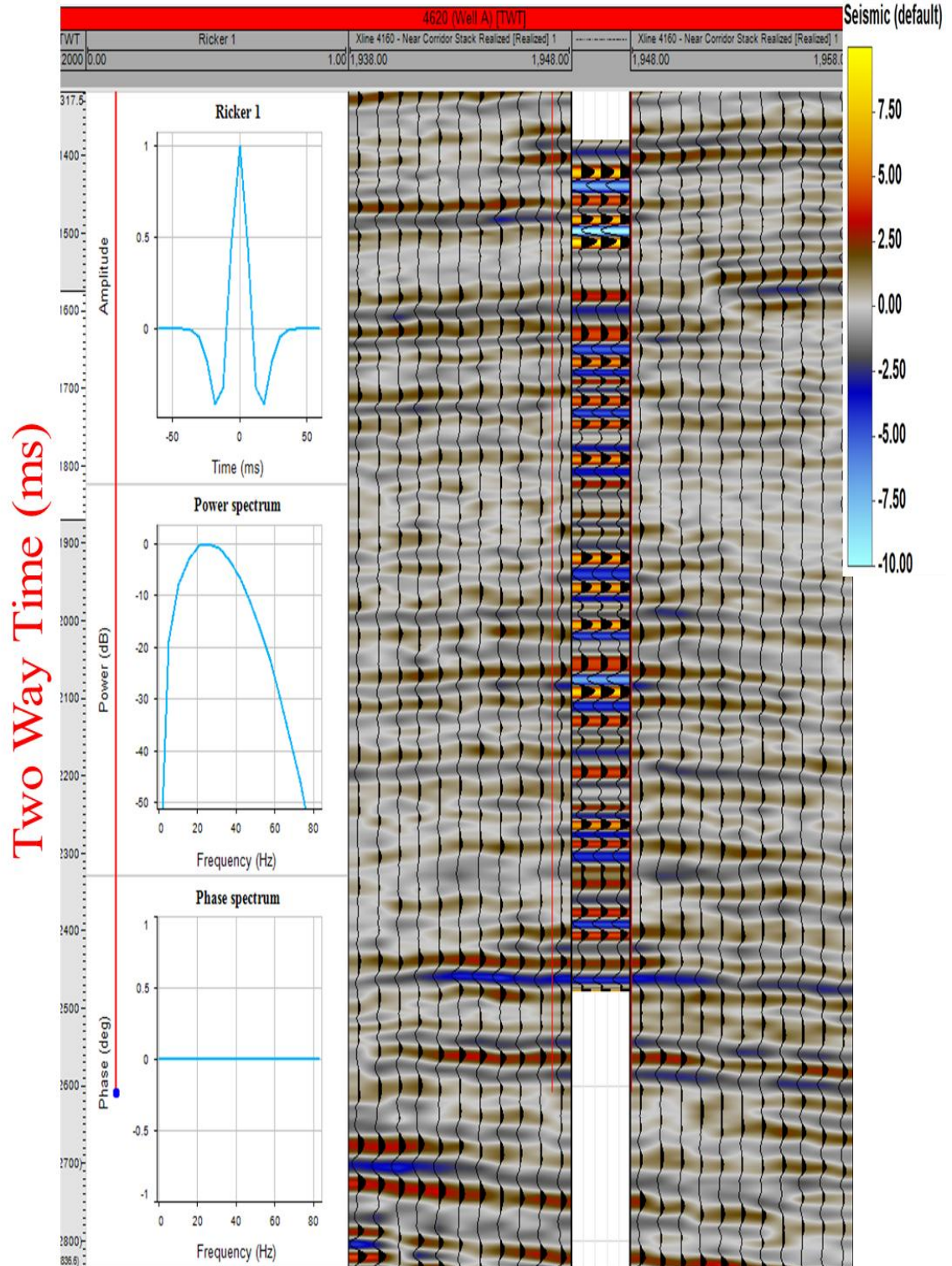
Figure 3.26 Well A Seismic-well tie using a zero-phase Ricker wavelet. Reservoir located at approximately 2450 ms.
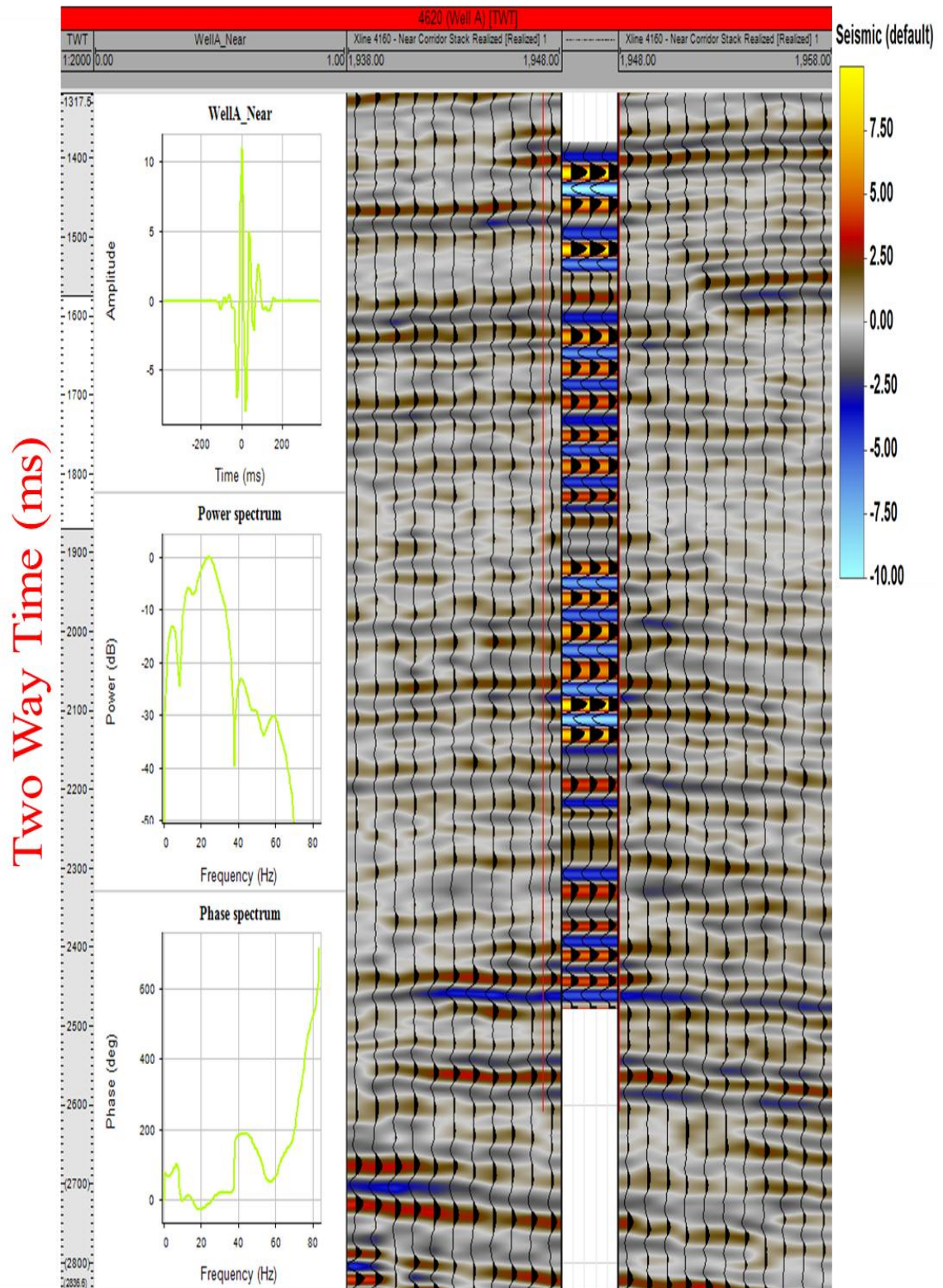
Figure 3.27 Well A Seismic-well tie using the extracted wavelet for the near angle stack volume. The synthetic trace overall ties with the seismic above the target reservoir zone.
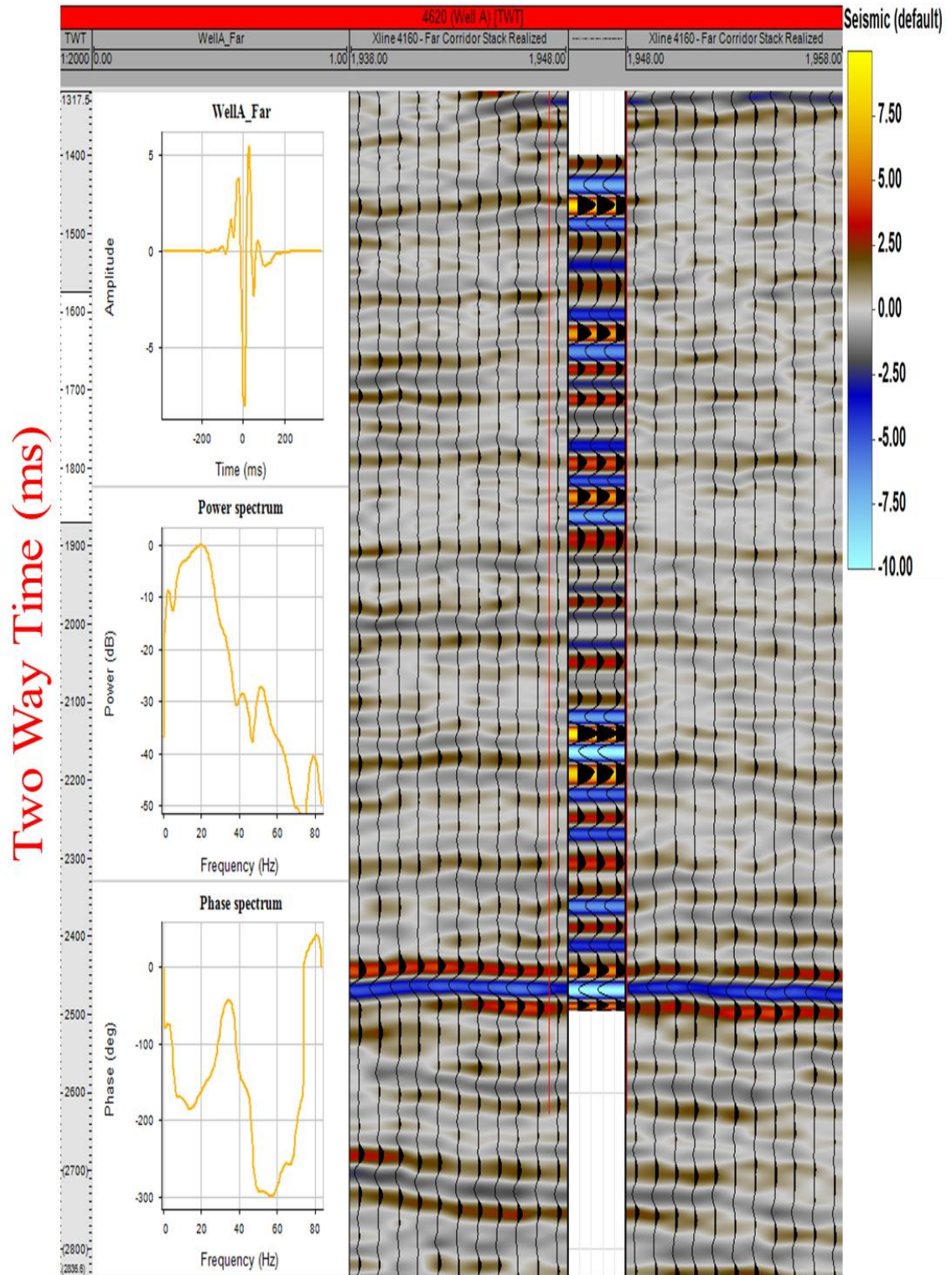
Figure 3.28 Well A Seismic-well tie using the extracted wavelet for the far angle stack volume. The synthetic trace overall ties with the seismic above the target reservoir zone.

3.4 Well Log AVO Synthetics

3.4.1 AVO Response vs. Observed Data

After converting the well logs to the time domain, I generated AVO synthetic seismograms at each well location to compare to the recorded data. Each of the synthetic seismograms was generated using a linear approximation of the Zoeppritz (1919) equations. The main goal of this step was to investigate the character of the seismic reflector at the reservoir level as seen in the well logs versus the previously processed seismic data. Well A, as seen in Figure 3.29, displayed an increasing AVO response in both the synthetic and observed seismic at the far offsets. However, consistent with the difficulty in the near trace well tie process, the expected small negative amplitude at the near offset was somewhat difficult to recognize. Similarly, Well B at 2280 ms. showed similar negative amplitude at far offsets, but a more noise contaminated near offset section (Figure 3.30). From these observations, I concluded that angle stacks derived from this existing data required preconditioning in the form of trim statics to ensure the alignment of the stacked volumes.
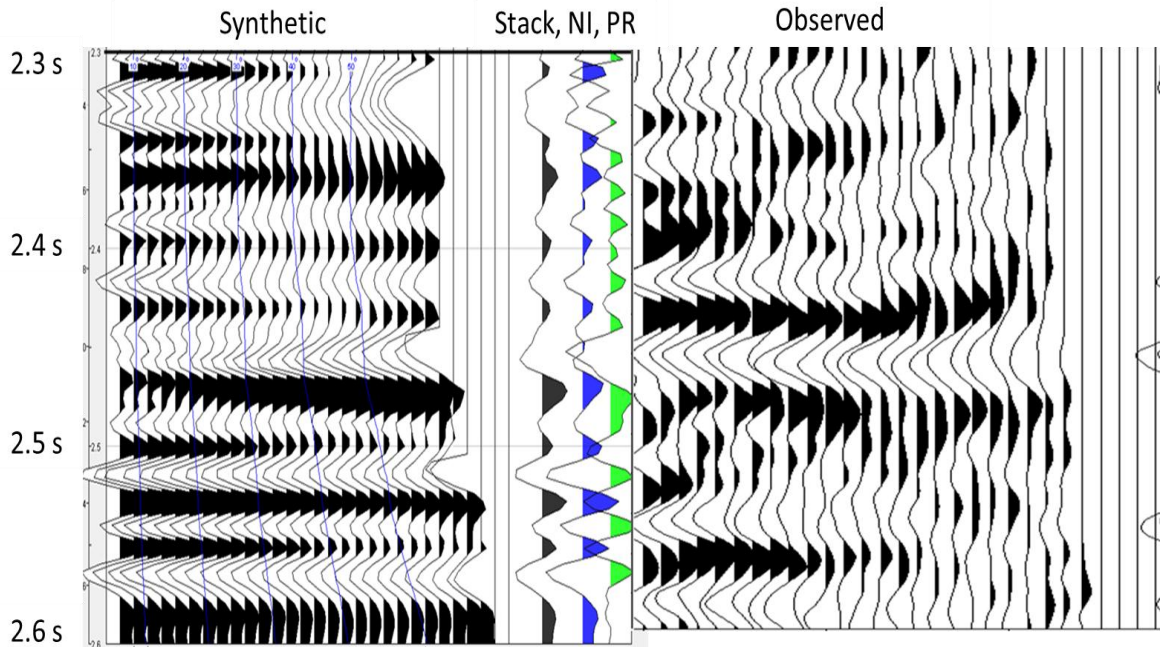
Figure 3.29 Well A . AVO synthetic (left) compared to observed data (right). Reservoir at 2450 ms shows Class II response.
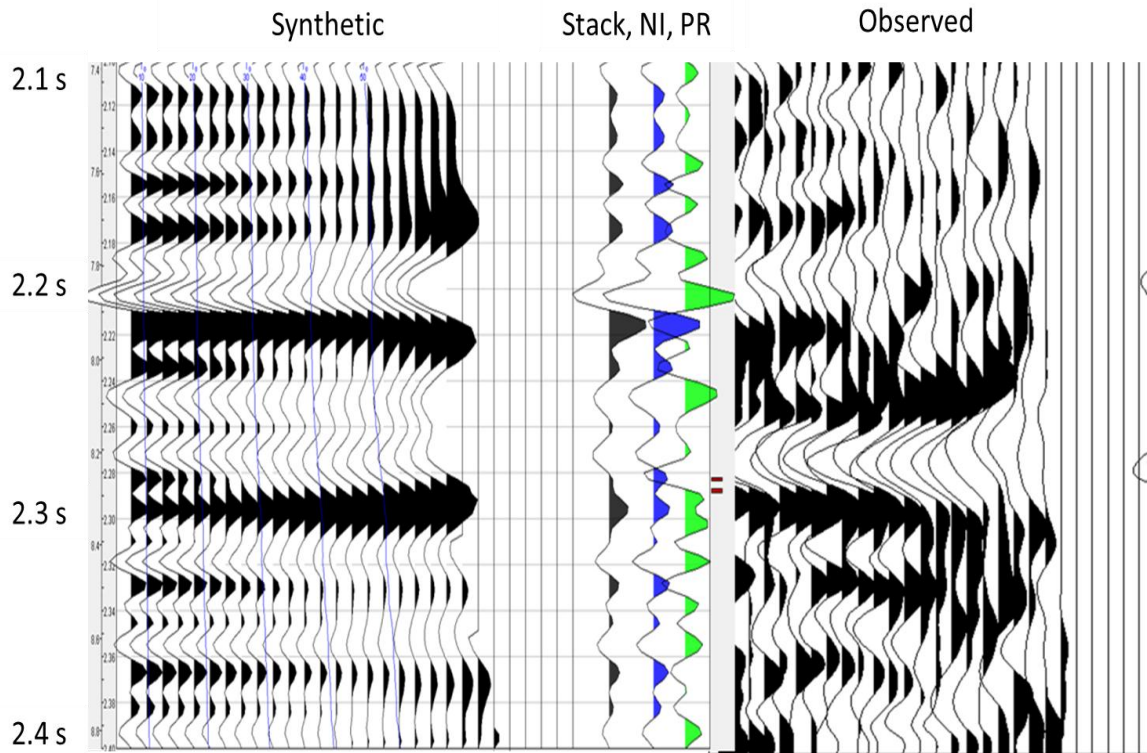
Figure 3.30 Well B AVO synthetic (left) compared to observed data (right). Reservoir at 2300 ms does not exhibit a distinct top of reservoir event, but the base reflector is clear on observed and synthetic level.

3.4.2 Fluid Substitution

To understand the influence of hydrocarbon saturation for this dataset, I implemented a fluid substitution experiment on two of the primary well locations, A and B. Utilizing PetroSeismic's jTIPS software, I used my previously derived well-log curves from Petrel to generate in-situ vs. water-substituted reservoirs at the well locations. Figures 3.31 and 3.32 showcase Well A, where the replacement of the gas reservoir yielded the expected significant changes in density and Poisson's Ratio, with a less dramatic effect on P-wave velocity. The synthetic seismic comparison between the in-situ and fluid-substituted synthetics showed a clear difference around the reservoir zone, as the water-substituted event had much reduced amplitude with offset. In the bottom left panel, the crossplots for ln(AI) vs Poisson's Impedance and the bottom central panel for Lambda-Rho vs Mu-Rho, which had previously shown good contrasts for fluid discrimination in earlier experiments, corroborate the fluid substitution as the water saturated reservoir falls along the expected sand curve in each plot. Figures 3.33 and 3.34 show the repeat of the fluid substitution experiment for Well B. For the in-situ well-log curves, the hydrocarbon zones on the AVO synthetic stack had a small normal incident positive amplitude, a Class 2p response, whereas for the water-saturated fluid substitution, the near trace had a large positive impedance change.
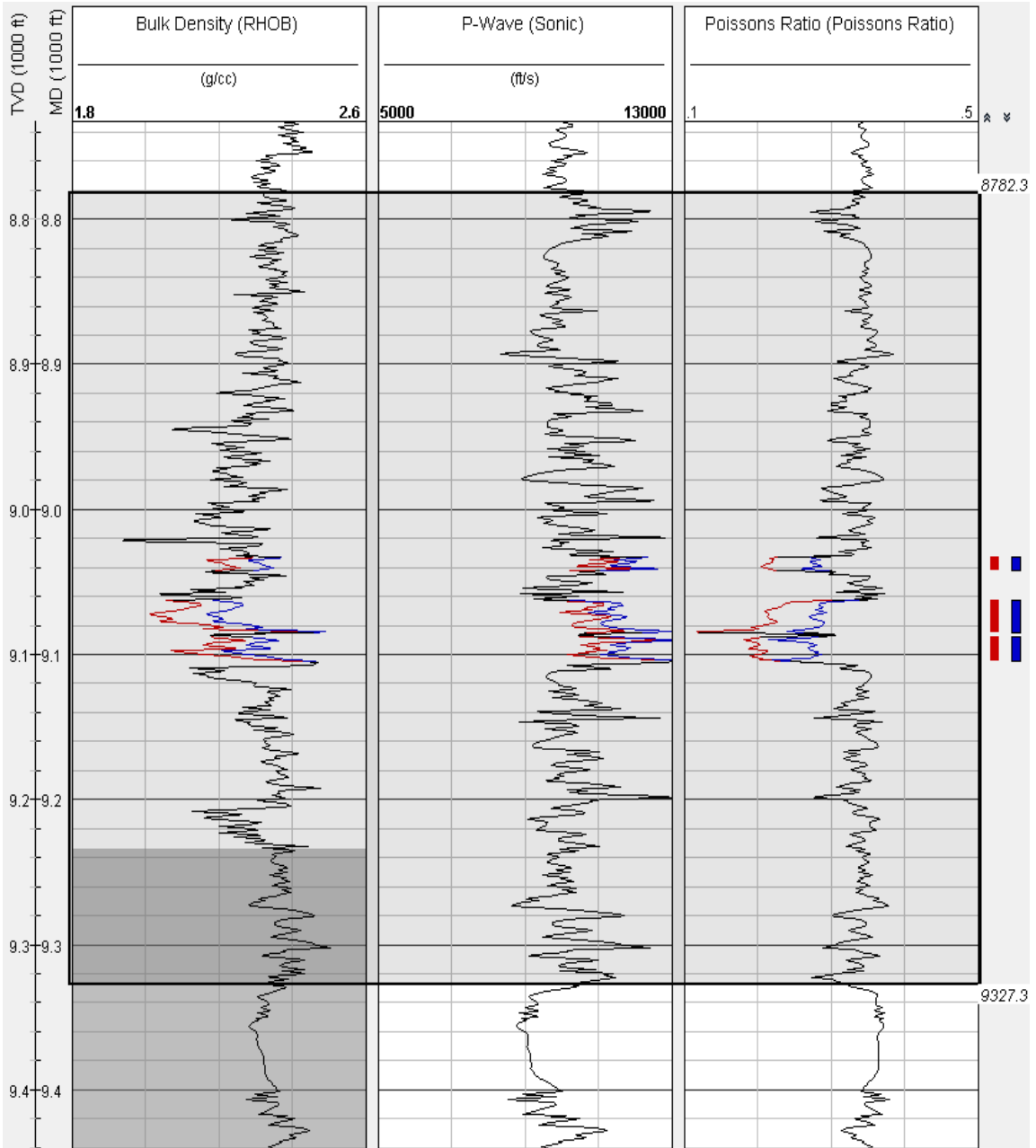
Figure 3.31 Well A fluid substitution experiment using jTIPS. Panels are well-log curves for density, P-wave, and Poisson's ratio. The largest change in well properties is in the density and Poisson's ratio curves. Red and blue curves represent gas and water saturated scenarios.
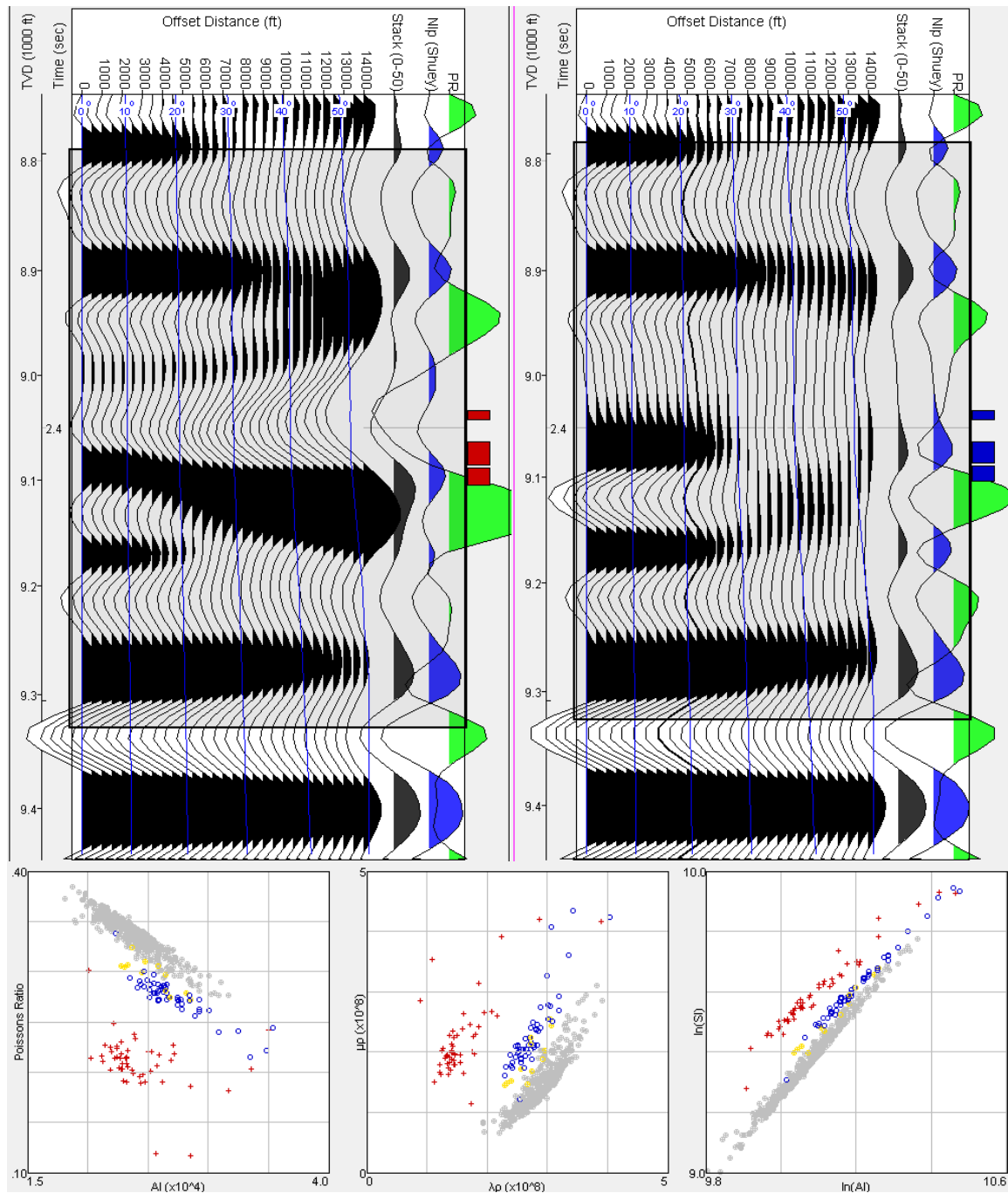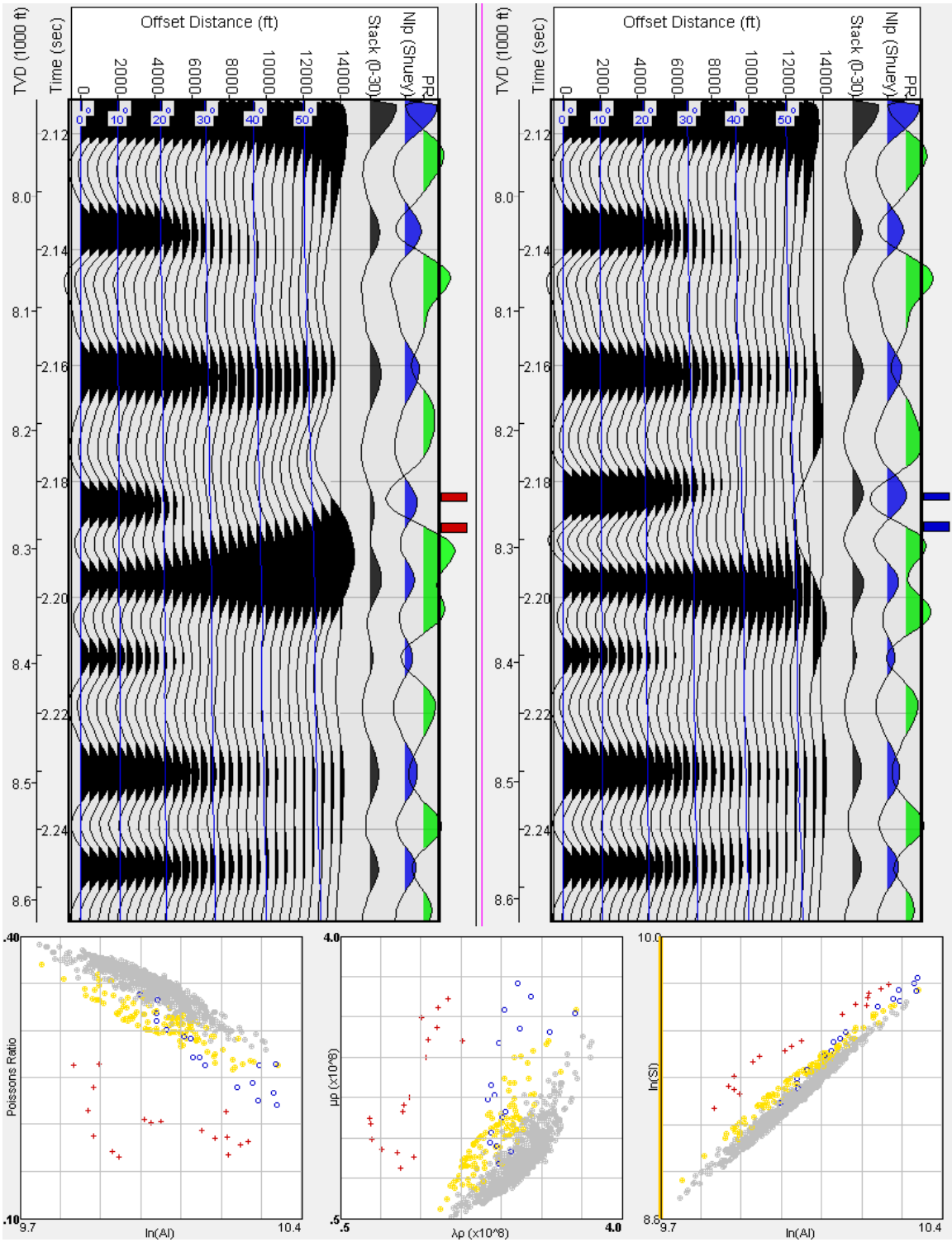
Figure 3.32 Well A fluid substitution experiment using jTIPS. Panels are AVO synthetics for in-situ and fluid-substituted pore-fluid properties (top), and elastic parameter crossplots (bottom). The synthetic seismogram changes from a Class 2n in the gas-saturated in-situ data to a Class 1 peak - tough in the fluid-substituted water-saturated synthetic.

58
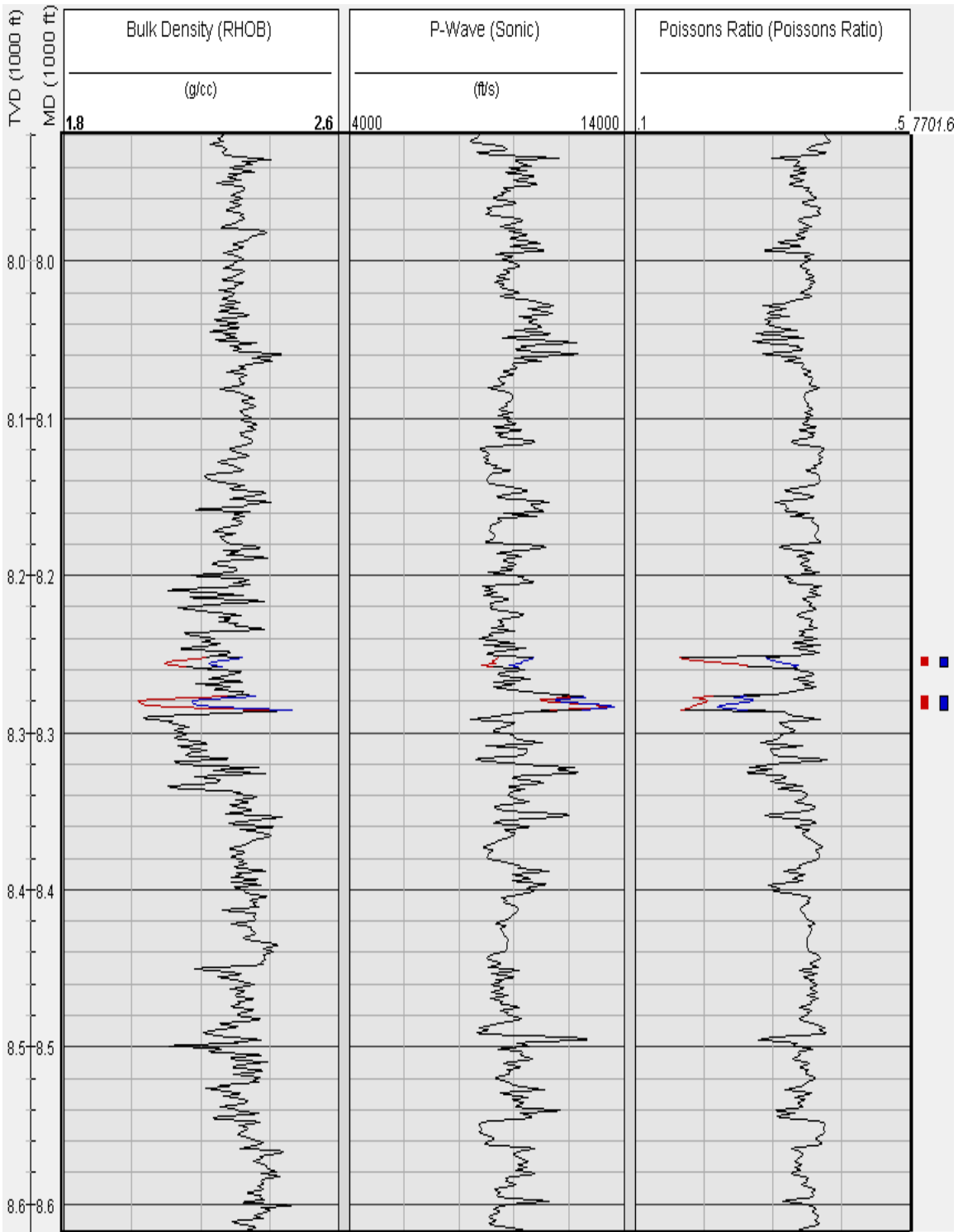
Figure 3.33 Well B fluid substitution experiment using jTIPS. Panels are well-log curves for density, P-wave, and Poisson's ratio. The largest change in well properties is in the density and Poisson's ratio curves. Red and blue curves represent gas and water saturated scenarios.

Figure 3.34 Well B fluid-substitution experiment using jTIPS. The AVO synthetic seismogram moves from a weak peak - trough (Class 2p) in the gas-saturated synthetic to a higher amplitude peak - trough (Class 1) in the water-substituted model.

3.5 Conclusions

After interpretation at the available well locations, it was clear that this survey posed a challenge in adequately imaging gas-bearing sand locations due to their faint amplitude signature and thin structure on the final stack data. According to well-log crossplots, the best possible combination of parameters for discriminating gas sands, brine sands, and shale utilized some combination of Lambda-Rho, Mu-Rho, and Poisson's ratio attributes. AVO modeling verified the initial information that indicated that the primary AVO response of the gas bearing sands were Class II, with minimal change to acoustic impedance due to fluid content change. One challenge that had to be overcome was the poor signal-to-noise ratio of the surface seismic data, especially for the near offset data that influences the acoustic impedance results. These observations were be kept in mind for the final seismic inversion processing and results.

CHAPTER IV

SEISMIC INTERPRETATION

4.1 Introduction

While the available well-log data allowed for a detailed analysis on a localized level, these data points had to be properly extended to the regional level for input to the inversion process. In order to accurately relay local well-log data to the seismic data, the horizon structure of the area must be understood to relate the geology to the well locations. Furthermore, AVO reconnaissance was implemented using angle stacks for an initial interpretation of anomalous events. A base map of the 3D seismic survey is shown in Figure 4.1 using a variance attribute.
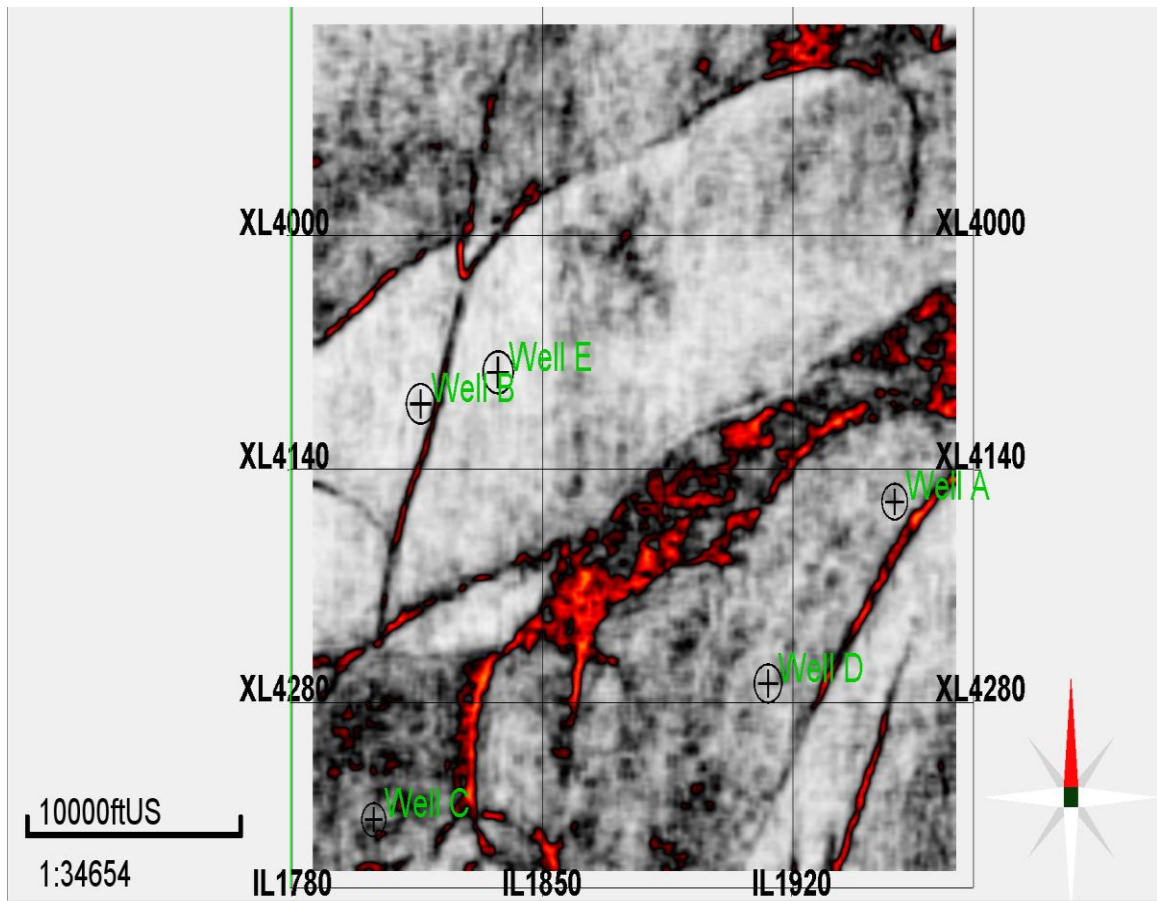
Figure 4.1 Time slice of seismic survey at 1800 ms. A Variance Attribute, which is related to the better known coherency process, highlights significant faulting in the area.

4.2 Fault Interpretation

As previously discussed in Chapter Two, the structural geology of the survey was dominated by normal growth faults associated with rapid sedimentation. Generally, these faults are younger basin ward and often coincide with paleo shelf breaks (Zhang and Watkins, 1994). The continued formation of growth faults allowed for increased sedimentation by providing the accommodation space for further sediment loading. This created a system of numerous major faults propagating from the shore towards the basin

interior. For this survey, I interpreted the locations of several large faults to assist in later interpretation of horizons for inversion model building, as well as quality control of the reservoir termination and seal. An effective tool I employed was the variance attribute, the inverse of coherency, which calculates the dissimilarity of seismic data. Practically, for the relatively flat geology and slow change in structure outside of faulting, the attribute suppressed the coherent seismic events to near-zero, and highlighted incoherency up to a value of 1. In total, 10 faults of notable prominence were interpreted, with four major faults that served as the reservoir boundaries that dominated the structure shown in Figures 4.2.
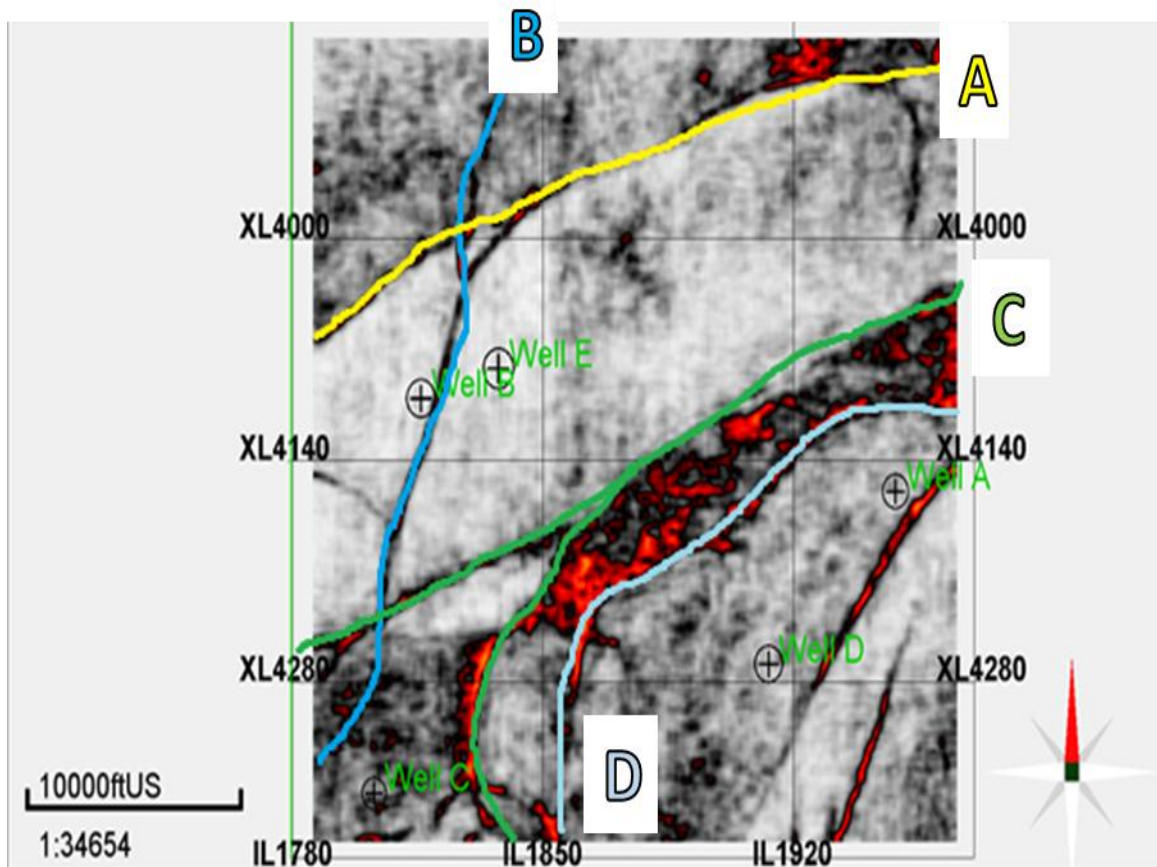
Figure 4.2 Fault map. Fault A (yellow) has relatively East-West strike with northern footwall and southern hanging wall. Fault B (blue) has relatively North-South strike with western footwall and eastern hanging wall. Fault C (green) and Fault D (grey) have East-West strike with northern footwall and southern hanging wall.

4.3 Seismic Interpretation and Attribute Generation

With the understanding of the fault framework, I sought to orient the well targets with the seismic data. In Figure 4.3, the full stack response of a NS line near Well B produced a noticeable trough at 2260 ms, which was related to a reduction in impedance between media, that is bound to Fault A in the North, and faded in amplitude as the inline moved to the south. In Figure 4.4, the near-offset stack over the same area did not yield

as large of an anomaly, but there was a small negative trough at the well location. The

far-offset stack in Figure 4.5 predictably revealed a significant trough at and away from

the well location. Figures 4.6-4.8 show the data from the repeat of the exercise at Well A,

bound by Faults C and D.

Another tool used in trying to initially resolve reservoir areas was extracting AVO

reflectivity attributes from the seismic angle stacks. These attributes are generally

derived using the linear approximations of Zoeppritz equations for intercept and gradient

terms of Shuey's (1985) equation or Verm and Hilterman's (1994) normal incident

reflectivity and Poisson Reflectivity. These equations are generalized as

$$R(\theta) = A + B\sin^2\theta \qquad \text{(Shuey 1985)} \qquad (4.1)$$

$$R(\theta) = NI\cos^2\theta + PR\sin^2\theta \quad \text{(Verm and Hilterman 1994)} \quad (4.2)$$

where:

$$A = NI = \text{Normal Incident Reflectivity (NI)} = \frac{1}{2}(\Delta\alpha/\alpha + \Delta\rho/\rho)$$

$$B = \frac{1}{2}(\Delta\alpha/\alpha) - (2\,\Delta\alpha/\alpha - \Delta\rho/\rho)(1 - 2\sigma/1 - \sigma)$$

$$PR = \text{Poisson Reflectivity (PR)} = (\sigma_2 - \sigma_1)/(1 - \sigma_{avg})^2$$

For this study, to better highlight the Class II AVO trends from the background

trend, I used equation 4.2 for NI and PR. Figures 4.9 and 4.10 show NIxPR attribute

before and after a -15 degree rotation along a North-South line near Well B. With a -15

degree rotation, the normal incidence variation of the trend was effectively zero,

validating that the distinction in sand and shale must be more evident in the change in

Poisson's ratio. Since Well B had previously shown a negative Class 2 AVO trend during the fluid substitution and AVO modeling, the reservoir could be recognized by the positive (blue) event at the well location. Post-rotation, the full extent of the reservoir sand layer was recovered from the background trend by rotating to effectively zero normal incident reflectivity. Figures 4.11 and 4.12 show the NIxPR attribute on a N-S line near Well A which displayed a more notable distinction of the reservoir between the pre-rotation and post-rotation stacks in conformance with the modeled Class 2p AVO response in the previous modeling steps. In all of these cases, the relationship of the reservoir and lithology change terminated at the fault boundaries, with the throw of the fault determining the displacement of the layers between the foot wall and hanging wall.

The final preliminary attribute extraction I used was root mean square (RMS) amplitude attributes from the interpreted reservoir horizon, whose time structure is seen in Figure 4.13. In Figure 4.14, the RMS amplitude of the full stack yields somewhat of a clear anomaly at Well B and E, but Well A was more noise contaminated to discriminate from the background amplitude. Figures 4.15-18 showcase the change in the reservoir RMS amplitude across 10° angle stacks (0° - 10°, 10° - 20°, 20° - 30°, and 30° - 40°). As the angle increases, the expected hydrocarbon reservoirs become clearer for both major reservoir areas. There are clear amplitude terminations along the fault planes, as well as areas of influence delineating reservoir extents, as interpreted in Figure 4.19.
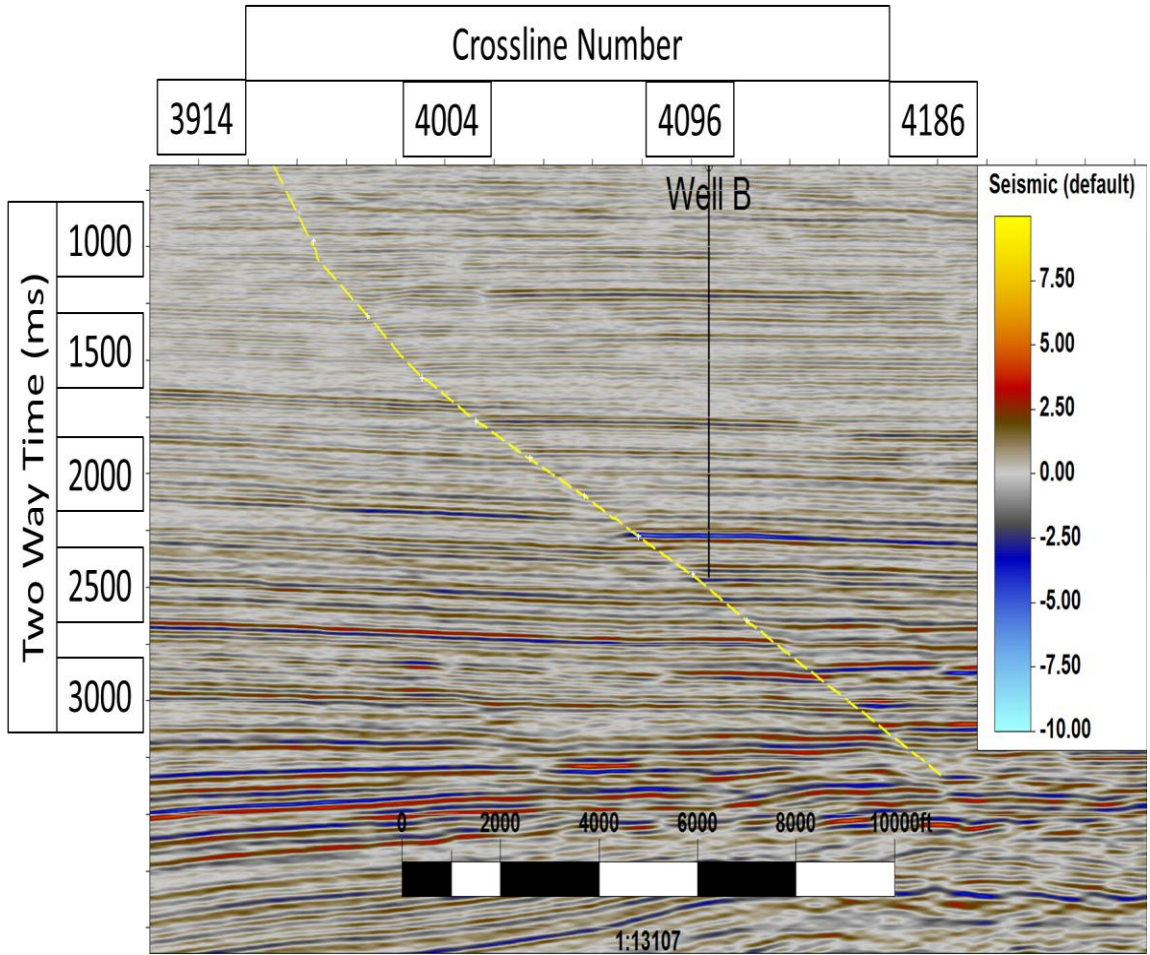
Figure 4.3 N-S line near Well B location. The noticeable trough on the *full-stack* section correlates to the gas reservoir previously noted in the well logs for Well B
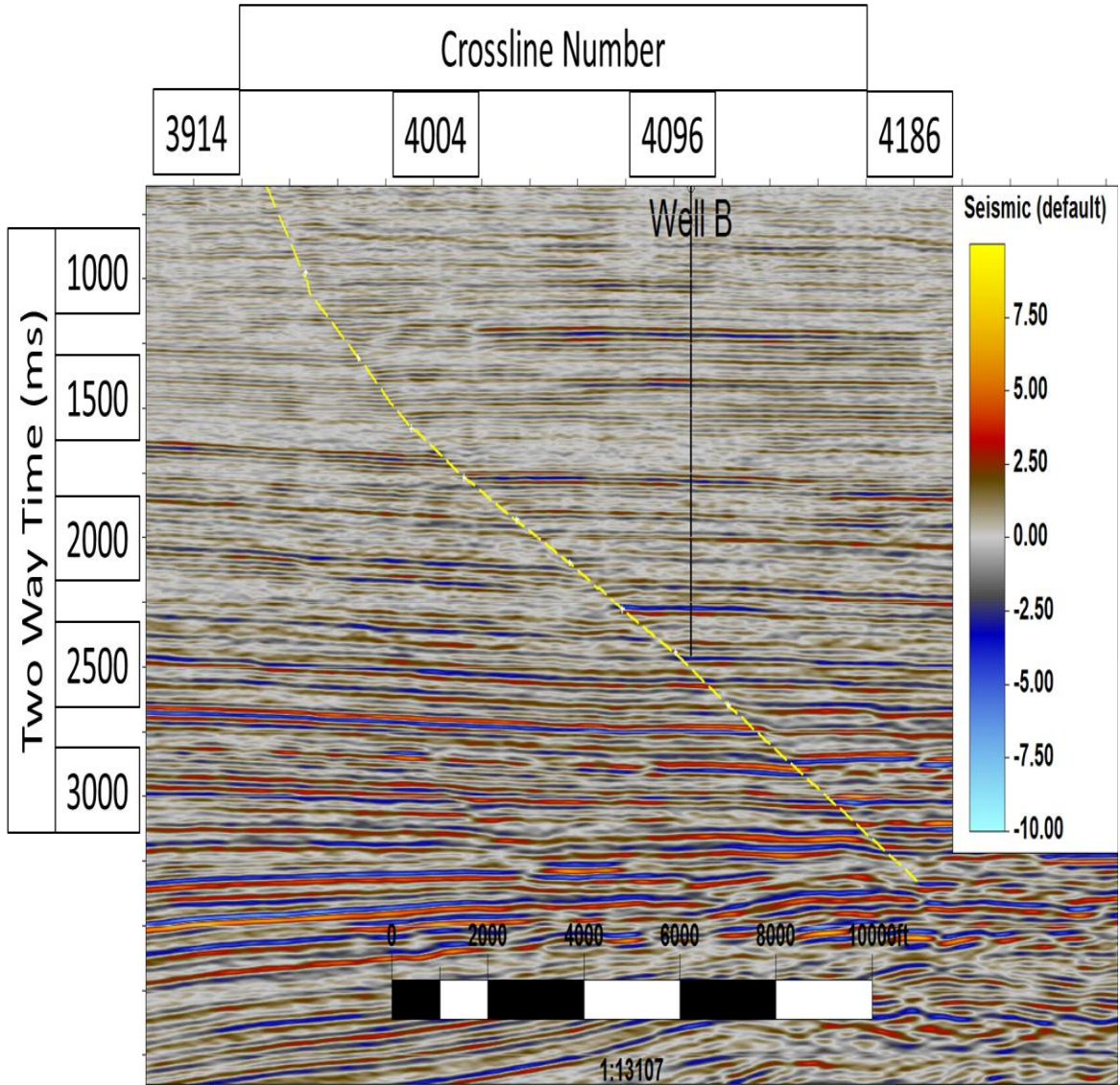
Figure 4.4 N-S line near Well B location. The *near-angle stack* section does not produce an impedance anomaly at the gas reservoir location.
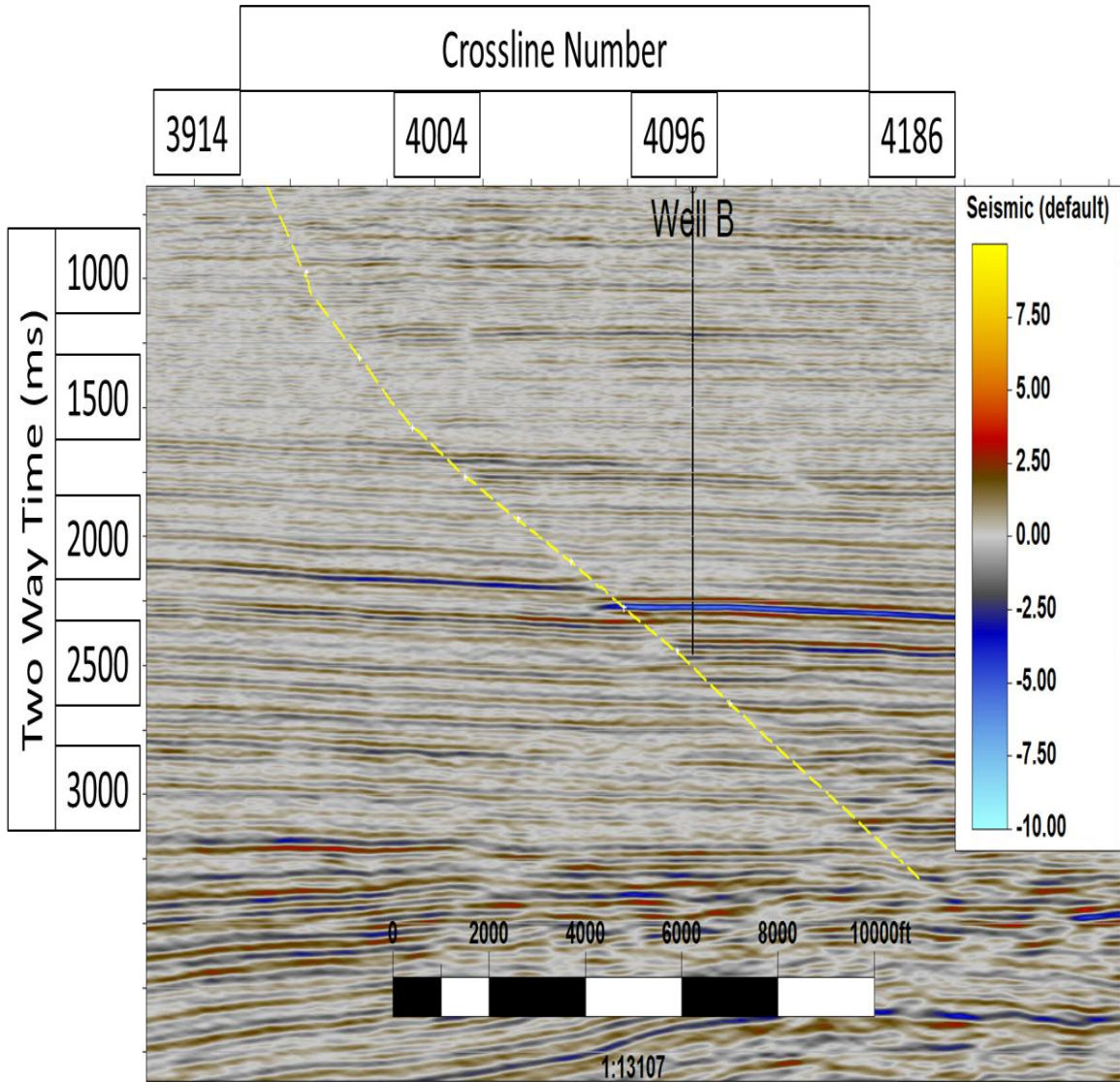
Figure 4.5 N-S line near Well B location. The *far-angle stack* section shows the previously discussed strong trough at the gas reservoir.
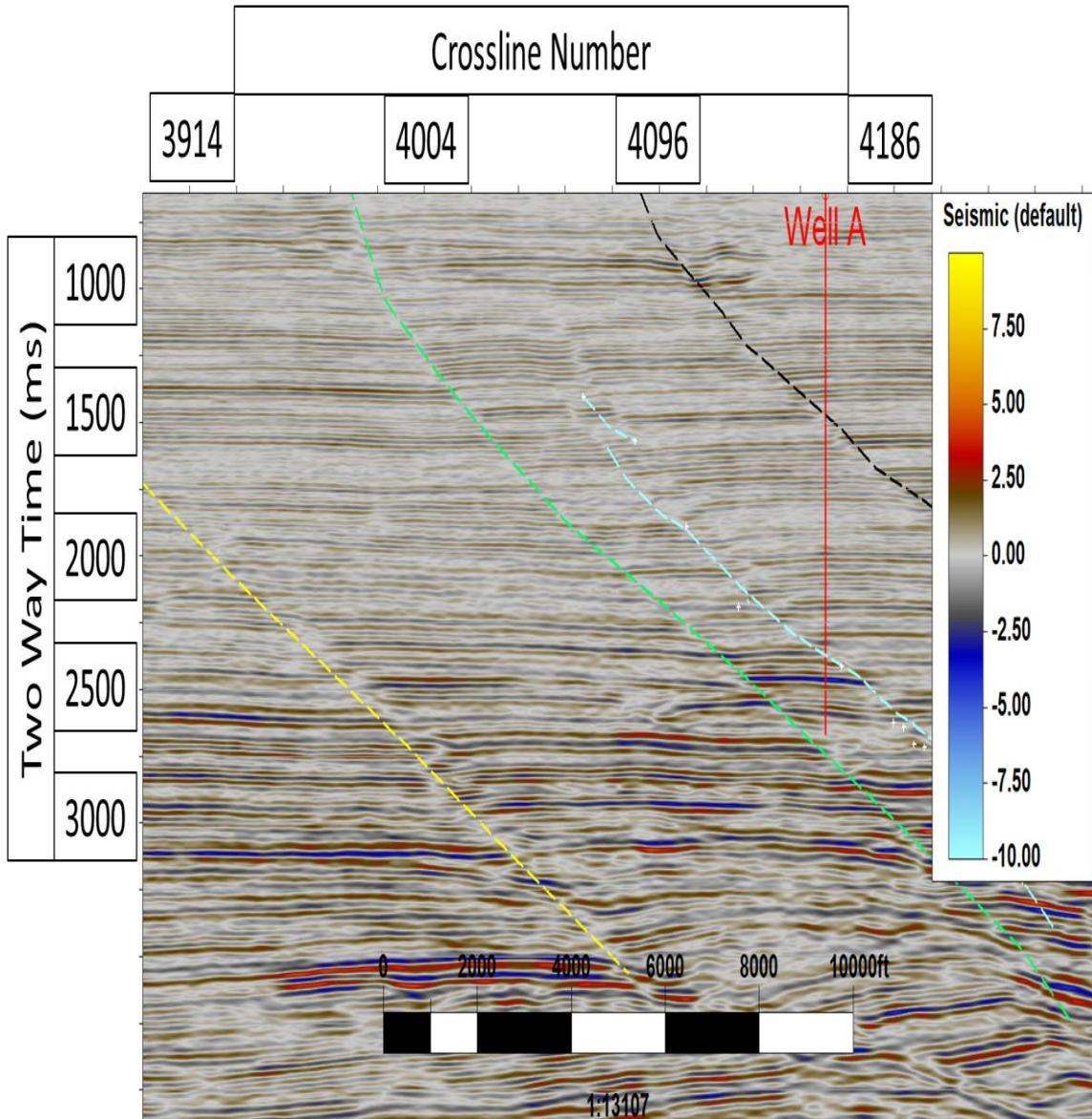
Figure 4.6. N-S line at Well A. On the *full stack* section, there is a strong negative reflection at the gas reservoir level that is bounded by faults on either side.
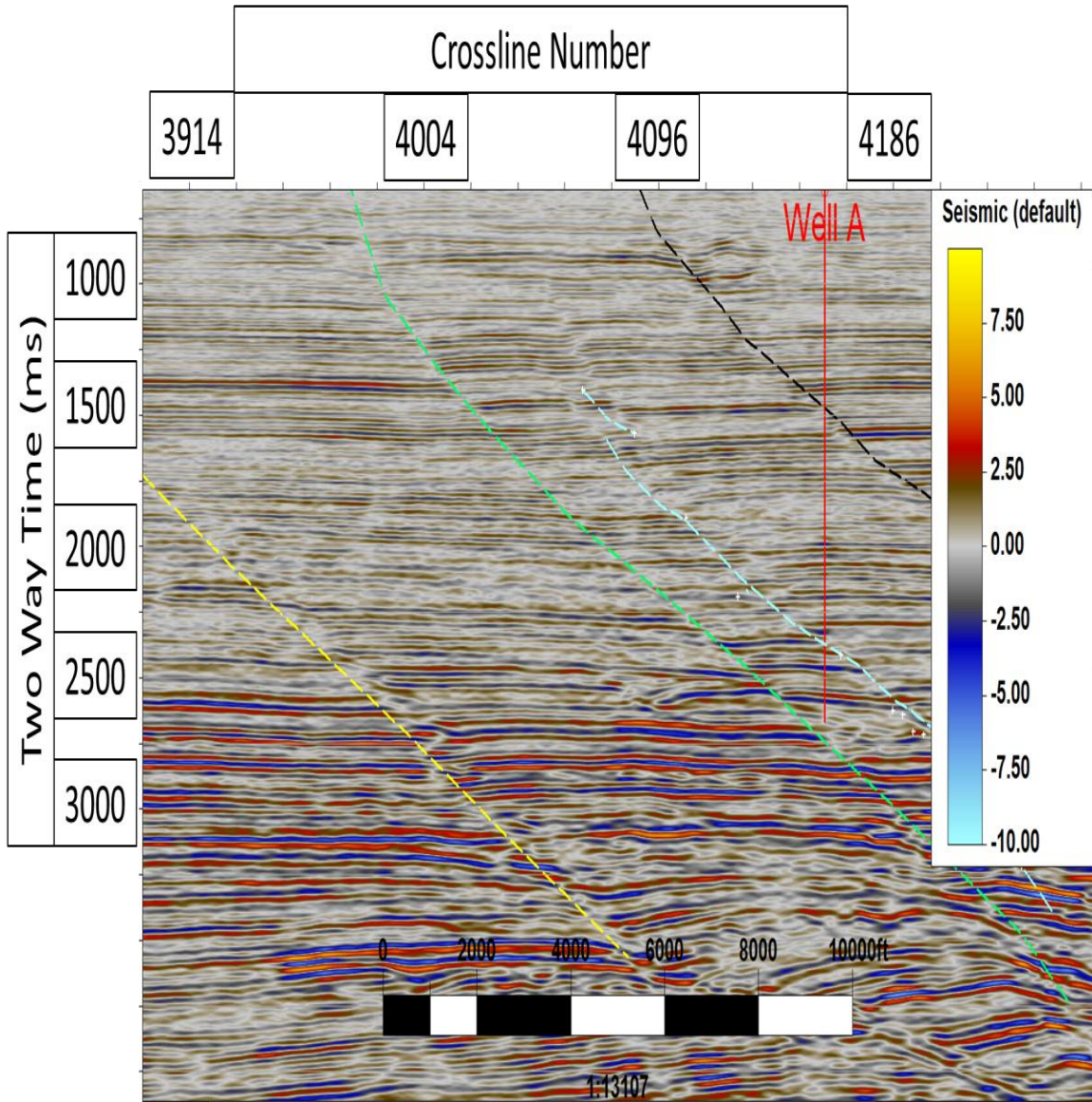
Figure 4.7. N-S line at Well A. The *near-angle* stack does not produce a significant anomaly at the gas reservoir level.
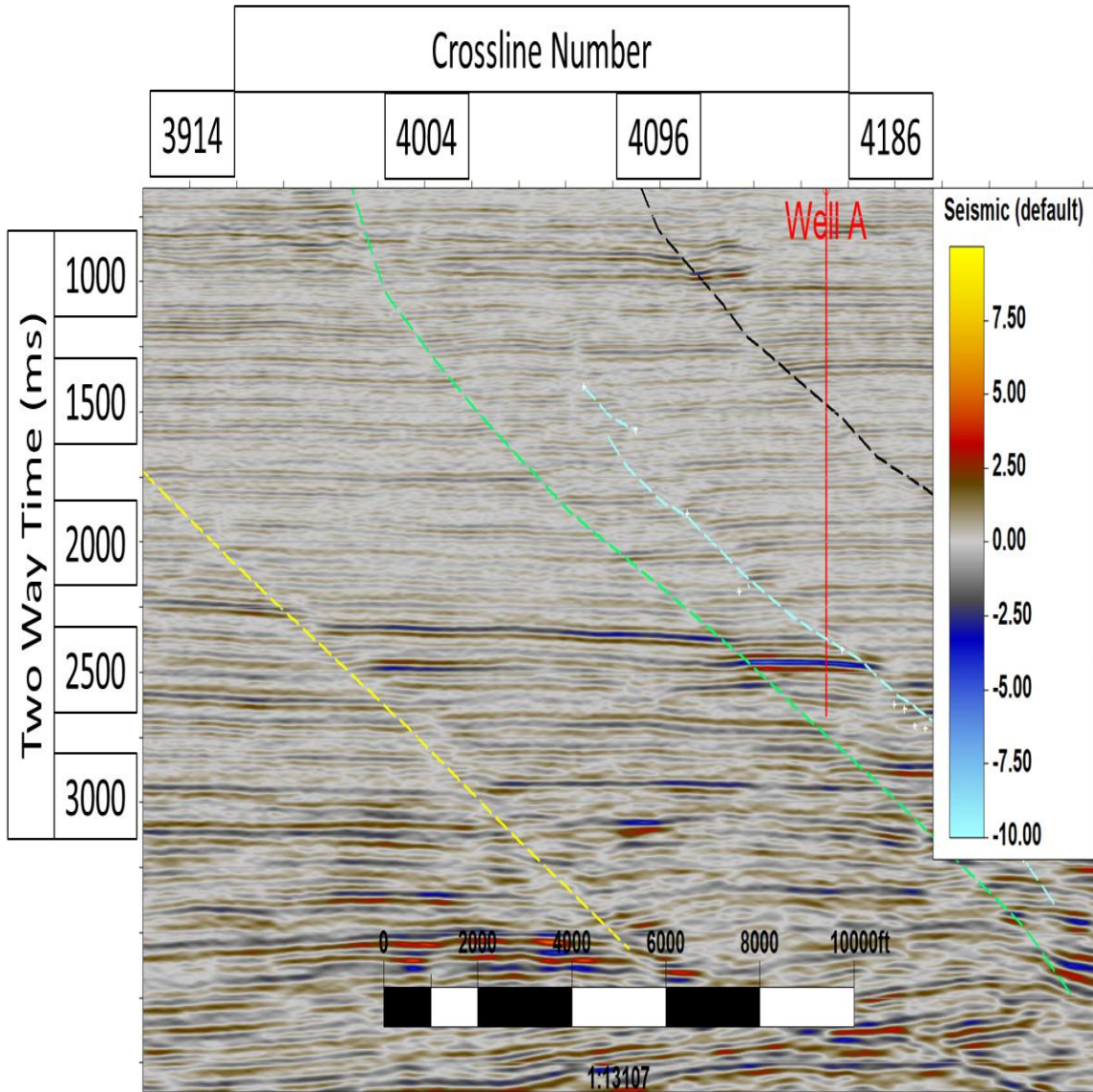
Figure 4.8 N-S line at Well A. The *far-angle* stack correlates to a strong trough reflection at the reservoir pay.
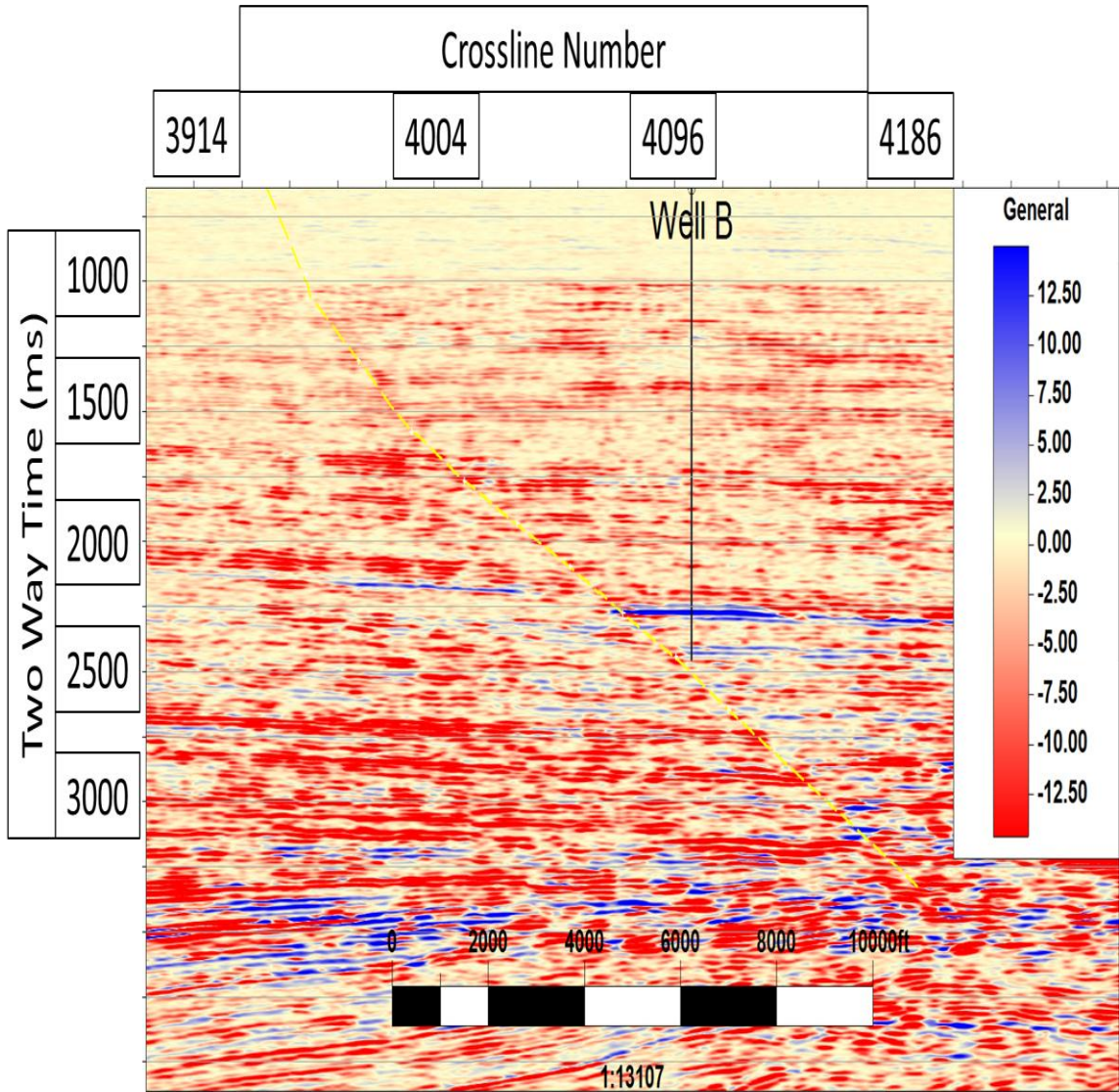
Figure 4.9 NIxPR (not rotated) attribute section for a N-S Line through Well B. There is a strong anomaly at well location B and a weaker anomaly along the expected reservoir horizon away from the well.
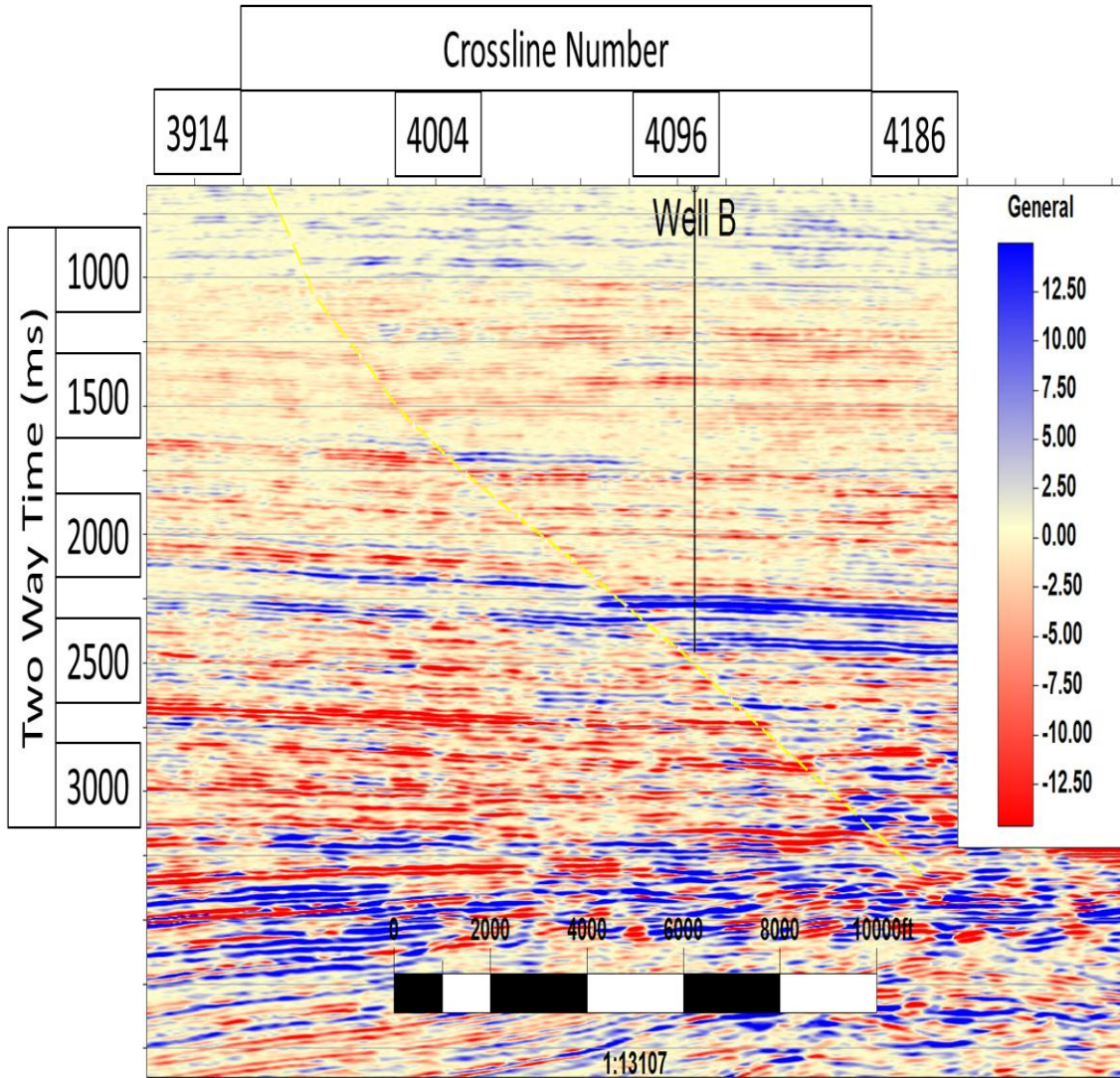
Figure 4.10 NIxPR (rotated) attribute section for a N-S Line through Well B. There is a strong anomaly at well location B, and the previously weak, discontinuous anomaly along the expected reservoir horizon away from the well has been recovered from the background trend.
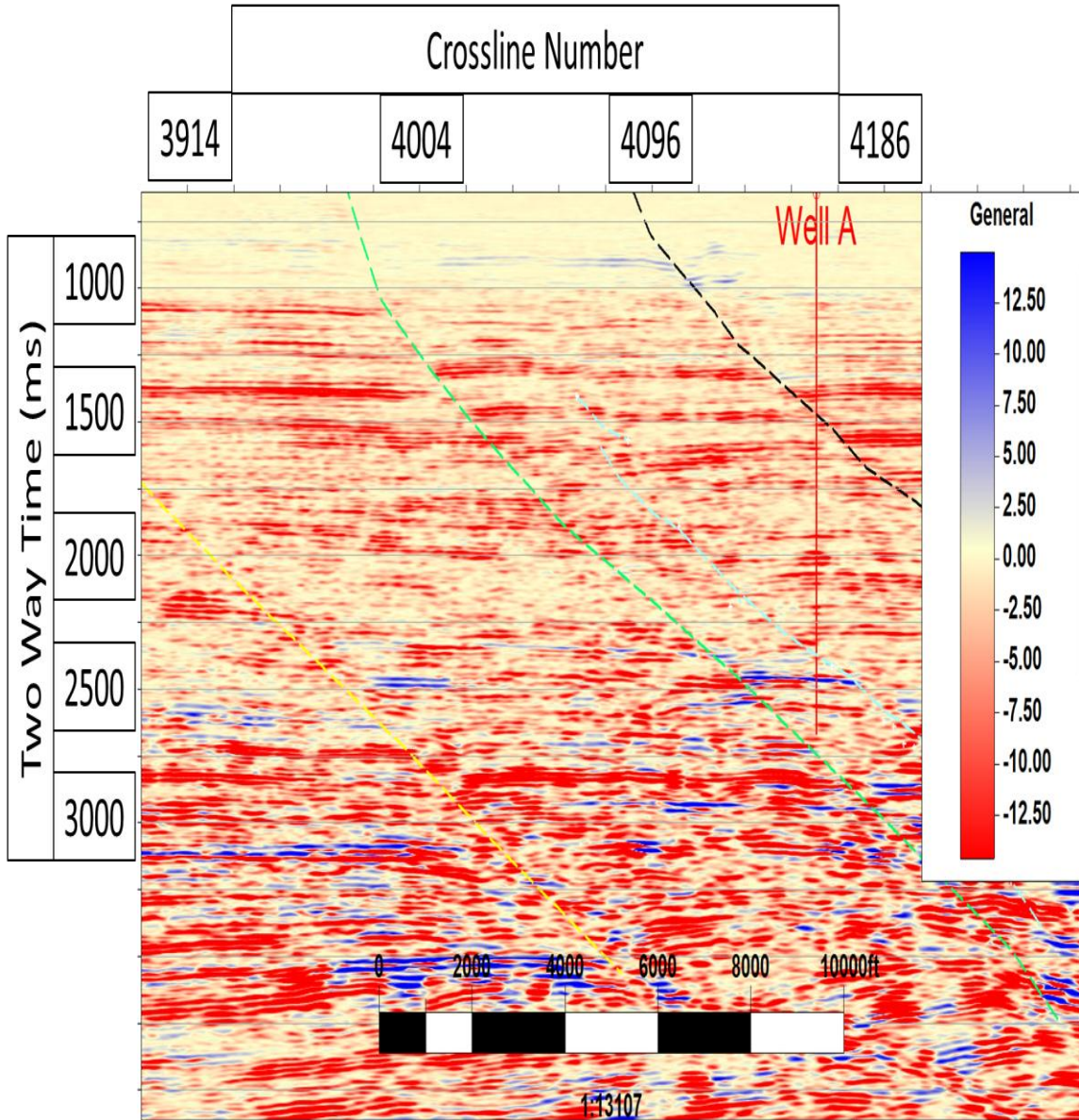
Figure 4.11 NIxPR (not rotated) attributes for a N-S Line through Well A. There is a weak anomaly at well location A at the center of the image.
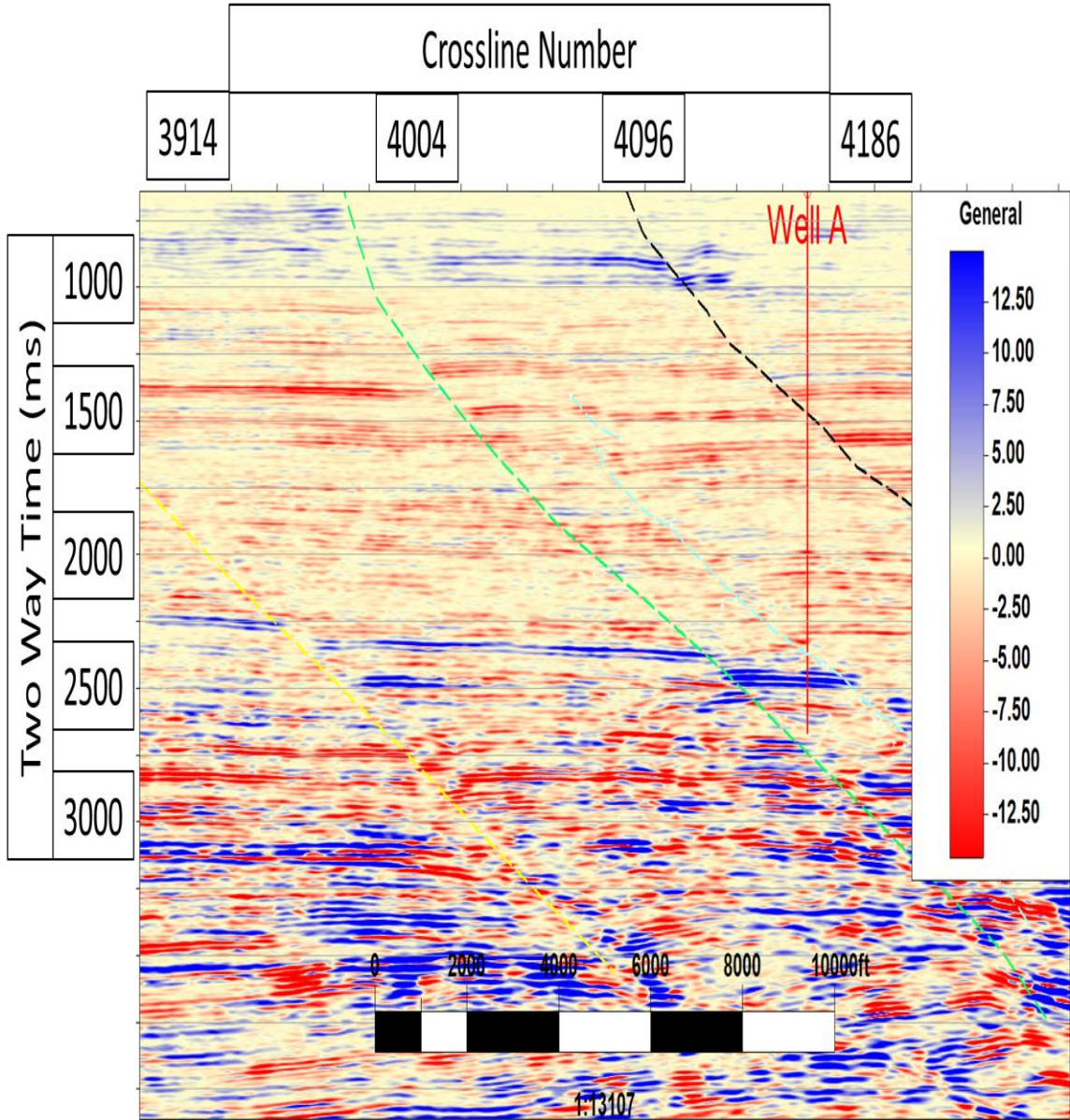
Figure 4.12 NIxPR (rotated) attributes for a N-S Line through Well A. The expected reservoir is now more apparent as a strong red (trough) response.
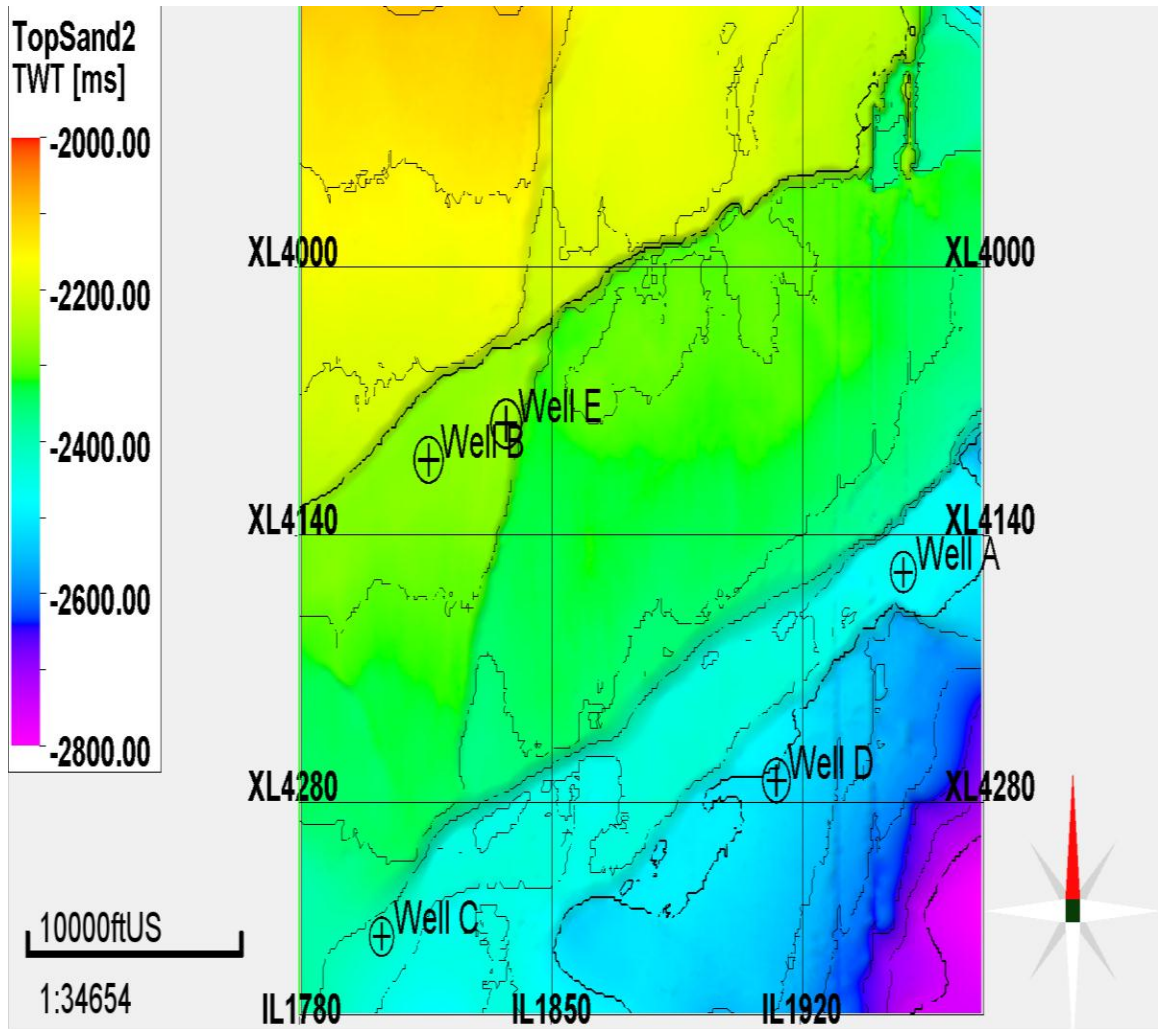
Figure 4.13. Two - way time structure map of reservoir horizon. Colors range from 2000 ms (yellow) to 2800 ms (purple)
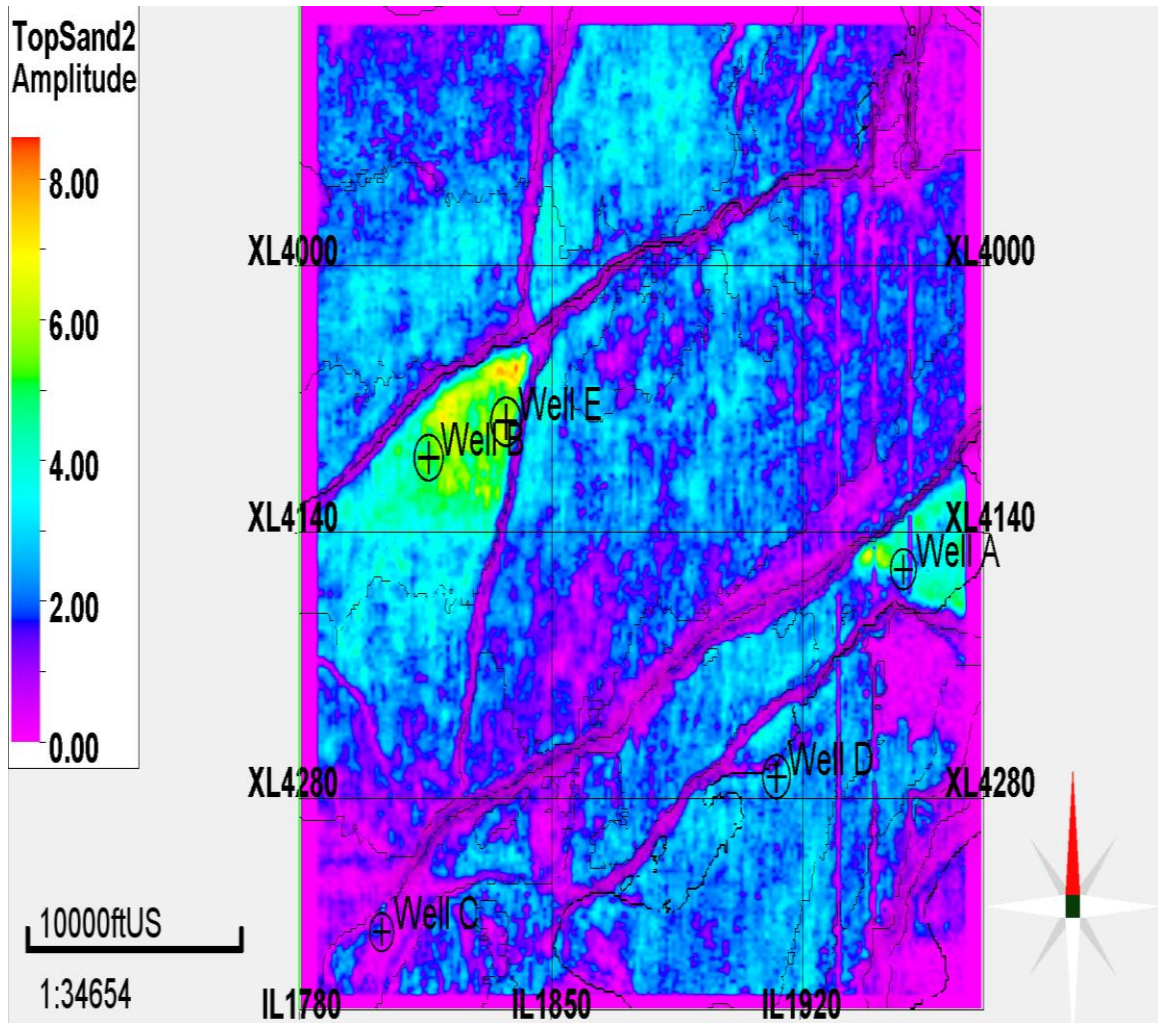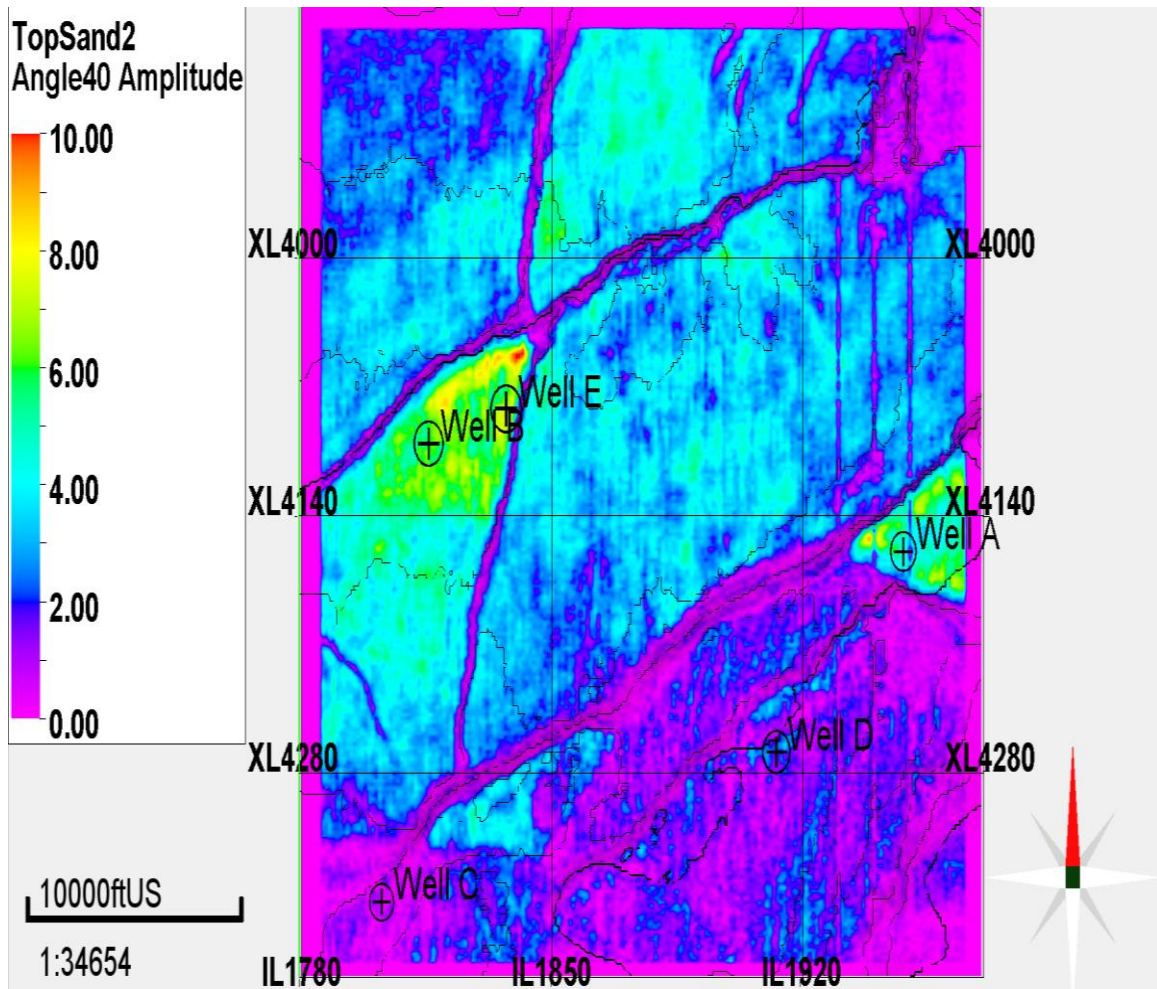
Figure 4.14. RMS amplitude of *full stack* at reservoir horizon. From left to right, red circles represent Wells B, E, and A. At this stage, Well B and E have a clear amplitude anomaly, while Well A does not
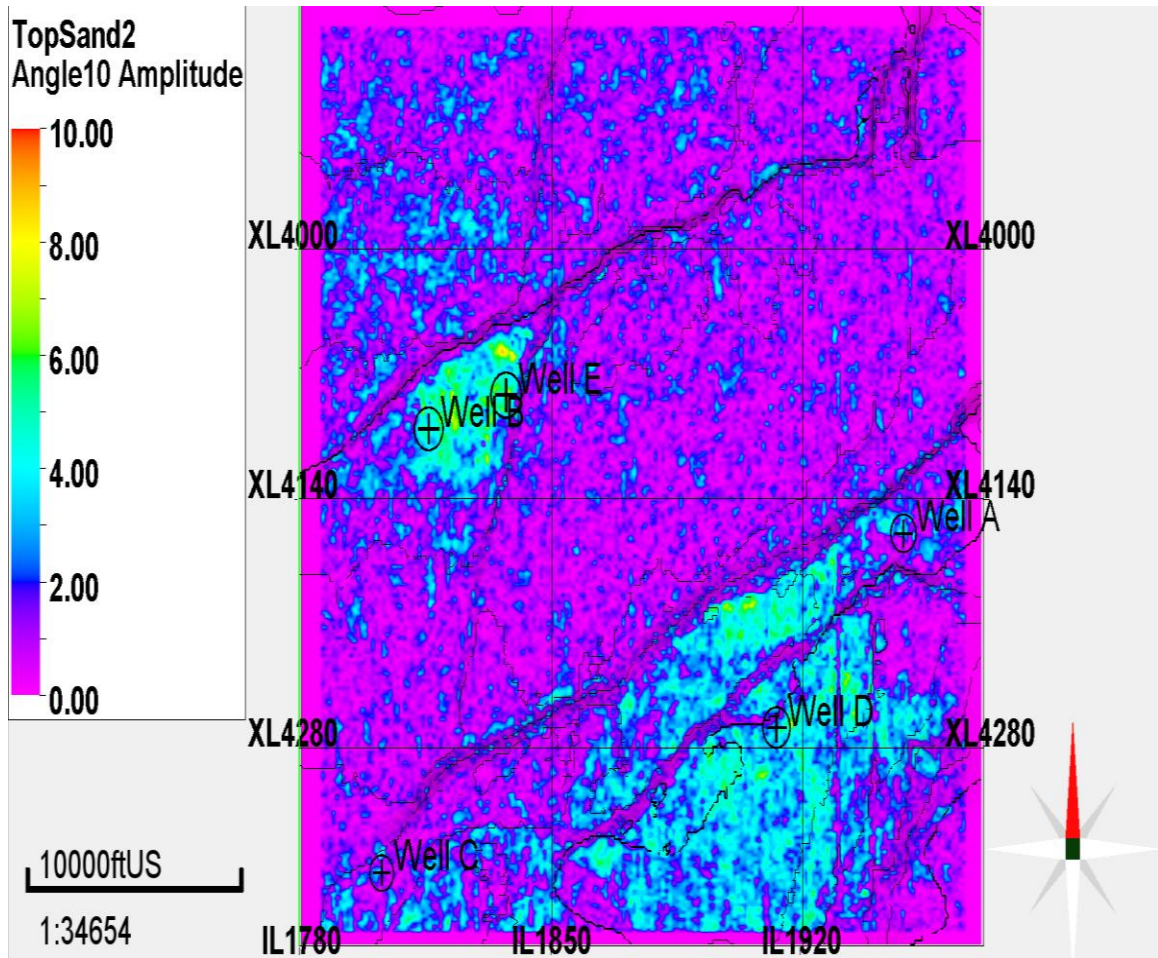
Figure 4.15. RMS amplitude of *Near (0-10° stack* at reservoir horizon. From left to right, red circles represent Wells B, E, and A. At this stage, Well B and E have a clear amplitude anomaly, while Well A does not.
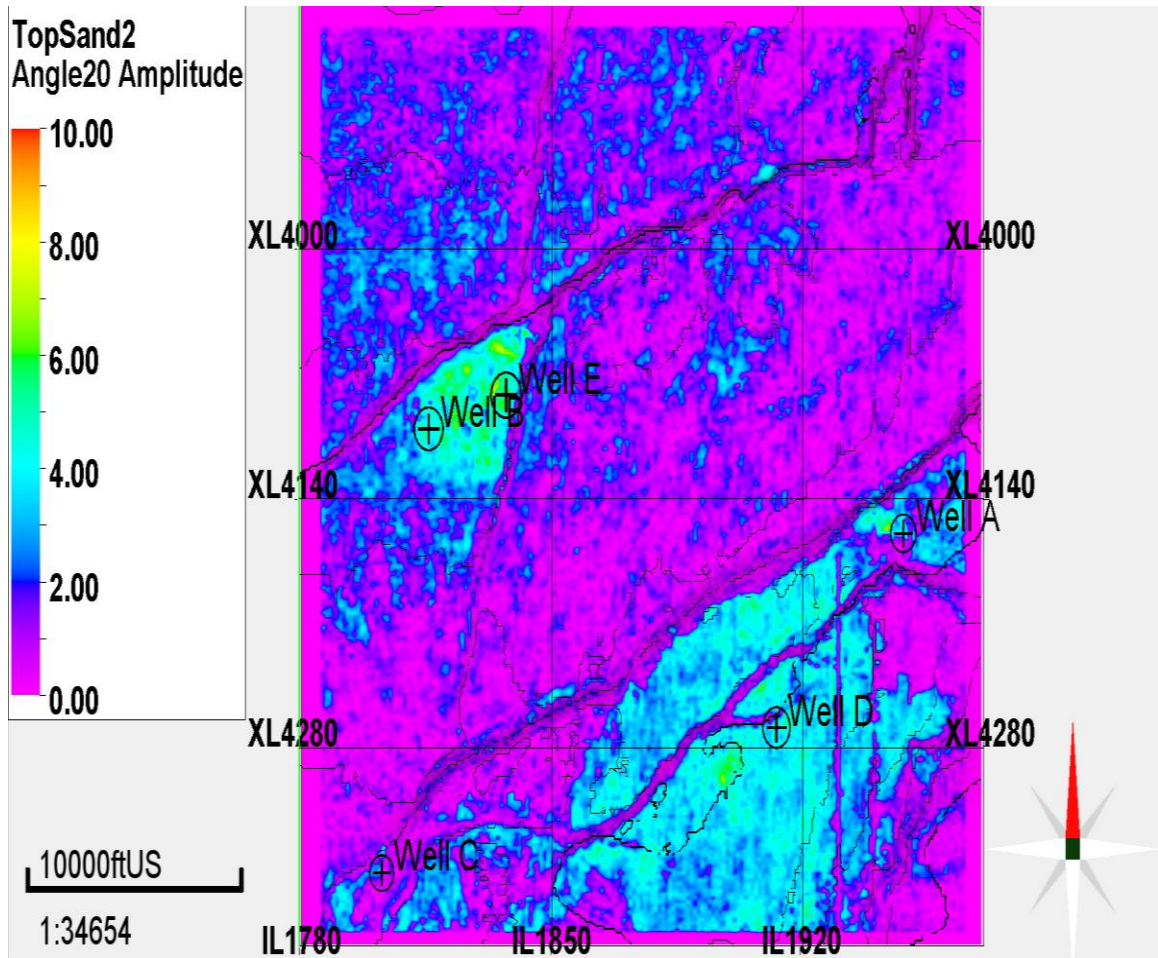
Figure 4.16. RMS Amplitude of *Near-Middle (10-20 Degrees)* Stack at reservoir horizon. From left to right, red circles represent Wells B, E, and A. Well B and E continue their strong amplitude anomaly, while Well A reservoir begins to take shape.
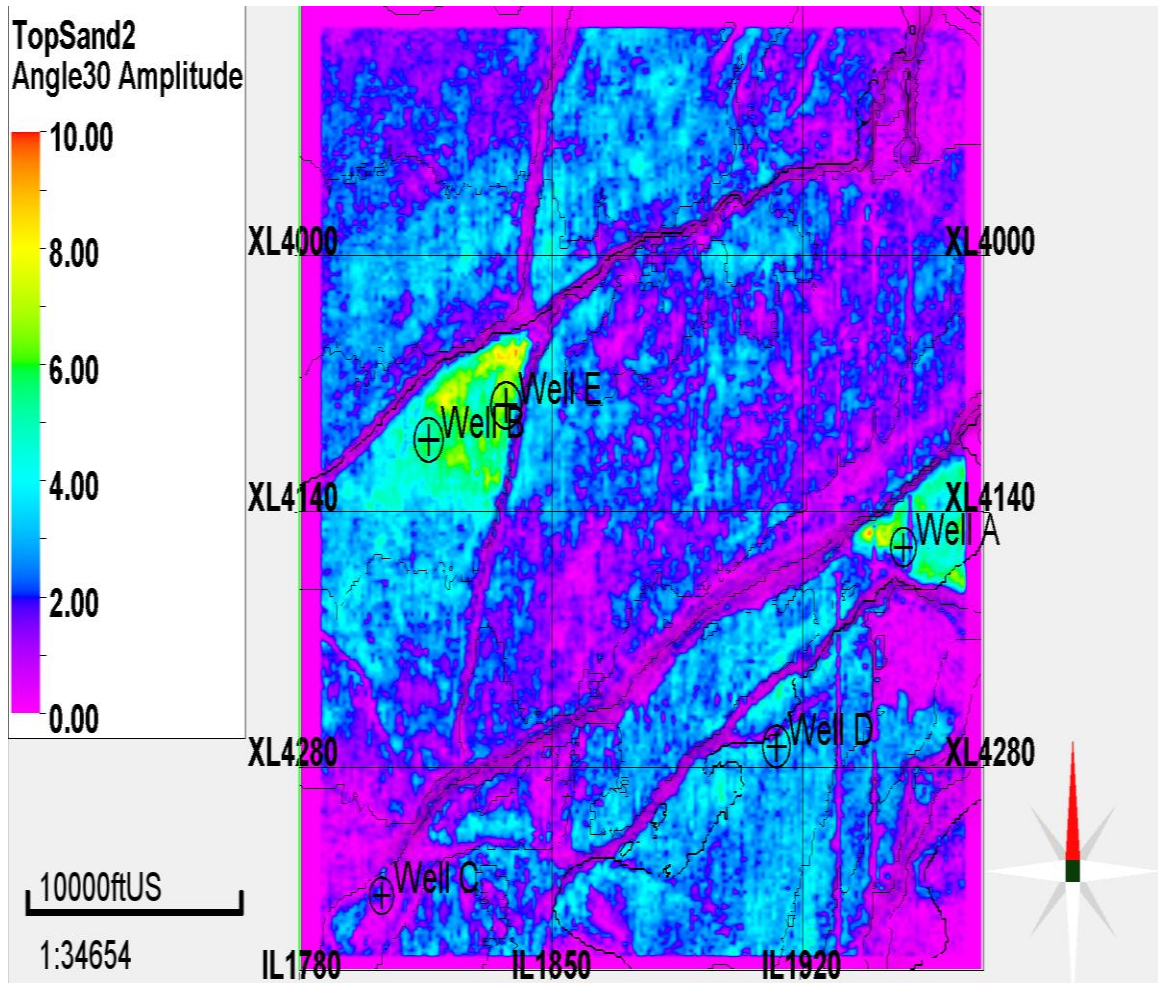
Figure 4.17. RMS Amplitude of *Far-Middle (20-30 Degrees) Stack* at reservoir horizon. From left to right, red circles represent Wells B, E, and A. Well B and E continue their strong amplitude anomaly, while Well A reservoir begins to differentiate from surrounding lithology. Fault boundaries start to become clearer at this level.

Figure 4.18. RMS Amplitude of *Far (30-40 Degrees) Stack* at reservoir horizon. From left to right, red circles represent Wells B, E, and A. Well B and E continue their strong amplitude anomaly, and Well A reservoir is nearly completely highlighted from all nearby lithology. Fault boundaries are very clear at this level. More amplitude information along the reservoir begins to come through outside the reservoir areas.
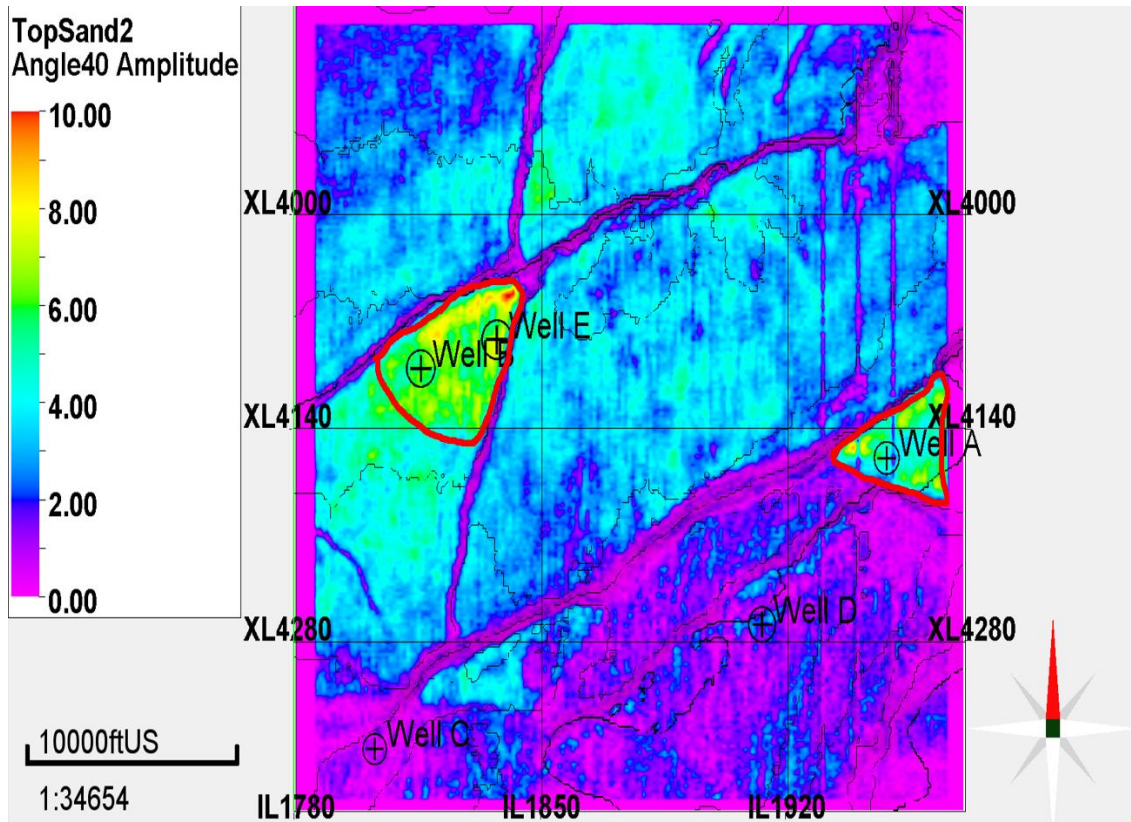
Figure 4.19. RMS Amplitude of *Far (30-40 Degrees) Stack* at reservoir horizon. Red Lines indicate rough outlines of reservoirs as derived from previous angle stack horizon amplitude extractions.

4.4 Conclusions

With a structural framework of faults, horizons, and target reservoirs delineated, the last inputs to the seismic inversion are ready. By relating the response of the AVO attributes at seismic scale to the interpretation of the well logs, the expectation was verified as consistent between wells and seismic in regards to Class II AVO gas sands with structural termination against major faults. With verification that the data was in agreement with each other, seismic inversion would be used to bring the two sources of information together and allowed a more comprehensive look into the entire survey.

CHAPTER V

SEISMIC INVERSION

5.1 Introduction

Seismic inversion refers to the process that transforms reflection data, which represents boundaries between different lithology, into rock properties. This is accomplished by generating a model response that fits the observed seismic data within a reasonable margin of error.

The algorithm used for this experiment was an application of pre-stack simultaneous seismic inversion. As described by Hampson and Russell (2006), the goal of the pre-stack seismic inversion was to obtain reliable estimates of p-wave velocity (Vp), s-wave velocity (Vs), and density (ρ), which were then used to predict the fluid and lithology properties of the subsurface. Since seismic data is a reflection property, it only contains information regarding the change in rock properties from one lithological unit to another, as seen in the derivation of reflectivity for Vp, Vs, and density

$$Rp = 0.5(\Delta Vp/Vp + \Delta\rho/\rho) \qquad\qquad (5.1)$$

$$Rs = 0.5(\Delta Vs/Vs + \Delta\rho/\rho) \qquad\qquad (5.2)$$

$$Rd = \Delta\rho/\rho \qquad\qquad (5.3)$$

where R, the reflection coefficient, is related to the impedance contrast between of two layers. For simplicity, the right side of Equation 5.3 will be referred to as an impedance

attribute. The inversion process takes a known R, the seismic data, and iteratively models impedance scenarios until a best global fit is resolved. The relationship of these reflectivities with angle of incidence was approximated using the Simon and Backus formulation of Fatti et al's (1994) variant of the Aki and Richards AVO equation, as shown below in Equation 5.4:

$$Rpp(\theta) = c_1 Rp + c_2 Rs + c_3 Rd \qquad (5.4)$$

$$c_1 = 1 + \tan^2\theta$$

$$c_2 = -8\gamma^2 \sin^2\theta$$

$$c_3 = -(1/2)\tan^2\theta + 2\gamma^2 \sin^2\theta$$

$$\gamma = Vs/Vp$$

5.2 Inversion Model Building and Results

To fit the change in reflectivity, an impedance contrast between two layers, to a functional layered-earth model, it was necessary to derive a low-frequency background trend of velocity and density. To optimize the calculations in simultaneous inversion, the γ constant in Equation 5.1, which represents the Vs/Vp ratio, was held constant at 1/2. Then, a linear trend derived from wells between the natural log of acoustic impedance and density was created for the initial density model. An example of this process, as well as an illustration of why a linear initial trend assists with interpretation and optimizing the inversion process, is shown in Figure 5.1. When conducting a simultaneous inversion, it was important to reduce any dependency between the variables to be inverted. In Figure 5.1, ln(shear impedance) is expressed in terms of a linear equation of the ln(acoustic

impedance) and an error term ΔL_S. Similarly, ln(density) is expressed in terms of the ln(acoustic impedance)and an error term ΔL_D. The independent variables in this example were ln(acoustic impedance), ΔL_S, and ΔL_D. Using these relationships, the equation below was derived to simultaneously resolve all three parameters based on perturbations from the linear trend between p-impedance, s- impedance, and density.

$$T(\theta) = \tilde{c}_1 W(\theta)DL_P + \tilde{c}_2 W(\theta)D\Delta L_S + c_3 W(\theta)D\Delta L_D \qquad (5.5)$$

$$\tilde{c}_1 = (1/2)c_{1\,+}(1/2)kc_2 \; + mc_3$$

$$\tilde{c}_2 = (1/2)c2$$

$$W(\theta) = \text{wavelet at angle of incidence } \theta$$

$$D = \text{Derivative operator}$$

$$Lp = \ln(\text{Acoustic Impedance})$$

As described by Hampson and Russel (2005), this was possible due to the observation that Vp, Vs and density are not three independent variables. This was corroborated in the way that Vs could be approximated from Vp, and density could be approximated from Vp. Using data from Well B, these linear trends between the natural log of the impedance and density attributes are displayed in Figure 5.2.

To balance the signal-to-noise concerns with the need for a wide variation in angle, I generated 4 angle stacks of 10° bandwidths for the seismic inversion. These volumes were then processed with trim statics to limit any residual moveout effects, though the overall displacements were fairly minute.

For this experiment, I populated a p-impedance model using the p-wave velocity information from Wells A and B, and left Wells C, D, and E blind. Similarly, linear estimates of density and s-impedance were derived from their natural log relationship to the natural log of p-impedance to populate the model for their respective properties. An 8 Hz high-cut filter was applied to the logs prior to the model building to ensure that only a global property is built. Horizons interpreted in the previous stage were used to interpolate the well data structurally. Figures 5.3-5.5 show an example of the initial model build through Well B for p-impedance, s-impedance, and density. After extensive testing of optimal parameters, the simultaneous inversion operator was applied in the target window from 1500 - 3000 ms. Figures 5.6-5.8 show the raw p-impedance, Vp/Vs ratio, and density results respectively at Wells A, B and C. The damping factor for the tie to the low frequency model was 15%, limiting the deviation from the input trend by that amount.

5.3 Rock Property Estimation and Results Discussion

From the inversion results, a multitude of parameter cubes were derived, including Vp/Vs ratio (Figure 5.9) and Poisson's ratio (Figure 5.10), shown at inline 1815 near Well B. These were the first signs of hydrocarbon prediction, as there were anomalously lower Vp/Vs and Poisson's ratio values at the known reservoir locations. Lambda-Rho and Mu-Rho were derived in Figures 5.11 and 5.12, and crossplotted in 5.13. Ultimately, while it did show a similar trend to the well log scenarios, it was not as clear in marking the gas sand away from the background trend. Furthermore, clean sand

vs. shale estimation was less than optimal, as seen in Figure 5.14, with an over estimation of sand lithology. While the sand bodies indicated in the well track were successfully marked, some sandy shales with volume of shale up to 80% were also indicated in the surrounding inversion results. Figure 5.15 displays a crossplot of p-impedance vs. density from the inversion volumes and an initial interpretation of gas sands vs. the background shale trend as indicated by the red zone. This response is what one would expect in a Class II AVO environment, where the acoustic impedance alone is not a fluid indicator, but the drop in density with fluid saturation changes can show anomalous behavior. Figure 5.16 applied this selection on the 3D cube to illustrate the overall rejection of the background trend, focused on the area around Well B. The stacked pay terminating against the fault line was successfully indicated, correlating with the strong troughs in the background seismic stack.

Utilizing the inversion volumes, I calculated values for porosity and water saturation. Figure 5.17 shows the derived porosity volume based on a crossplot of P-impedance vs. derived porosity using well log data, derived from the linear approximation of bulk density from the initial model building. Figure 5.18 shows the derived water saturation volume, which is derived from the following:

$$\rho = \varphi\big((1 - Sw)\rho_{gas} + Sw\rho_{water}\big) + (1 - \varphi)\rho_{matrix} \qquad (5.6)$$

Using $\rho gas = 0.29$ g/cm^3, $\rho water = 1.09$ g/cm^3, and $\rho matrix = 2.65$ g/cm^3, the equation 5.6 solves for water saturation with the following:

$$Sw = [((\rho - 2.65\,(1 - \varphi))\,/\,\varphi) - 0.29]\,/\,0.8 \qquad (5.7)$$

Similar to what was derived in the well logs, water saturation in the expected hydrocarbon-bearing units was calculated to around 20-40 percent, which made this derived attribute an effective QC of the inversion results. Figures 5.19-5.21 display the stack responses with overlay of the derived Sw attribute at each of the blind wells that were predicted by the inversion results. Each result showed a structurally-conformable drop in water saturation as the event moved up dip, terminating against a fault plane that acted as a seal. Given the presence of hydrocarbon reservoirs on either side of a fault plane, as seen most prominently in Figure 5.21, the trapping mechanism for the hydrocarbon accumulation was likely the low sand profile in the target depth. With an opposing foot wall lithology being primarily composed of less permeable shale units, the thin sands that terminated against the faults operate as the reservoir. The fault seal quality was interpreted as not being a complete seal, as there was some leakage of hydrocarbon saturation within a sand unit on either side of the fault.

Further attributes derived as hydrocarbon indicators were Poisson impedance and Lambda/Mu. Quakenbush et al. (2006) described the "Poisson impedance" attribute as the subtraction of the P-impedance and S-impedance scaled by a constant, γ, to isolate individual lithology or fluid saturations. In this case, using $\gamma = \sqrt{2}$ scaleed the result so that gas-bearing sands would approach zero Figure 5.22 shows the result of a north-south line through Well E when Poisson impedance was derived as follows:

$$PI = AI - \sqrt{2} * SI \qquad (5.8)$$

By dividing Lambda-Rho with Mu-Rho, the expected drop in the Lambda modulus with hydrocarbon saturation combined with the lack of change in Mu with respect to pore fluid

created a similar response to Poisson impedance. Both attributes were extracted along the reservoir horizon in Figures 5.23 and 5.24 to highlight their similarities in delineating the reservoir zones.

As a final fluid determination QC, the water saturation was overlaid on time slices at each of the expected gas sand reservoirs as seen in Figures 5.25-5.28. Overall, the responses for Well B and E were the strongest, with a clear termination and closure along fault lines and concentration in the high points of the sand body. Well A as shown in Figure 5.26, though somewhat disjointed in response, did maintain the expected shape as derived from other attributes. For Well C as shown in Figure 5.27, being at the edge of the survey limited how much could be interpreted reliably, though it is clear from the attribute analysis and the previous NIxPR attributes that the gas reservoir was successfully modeled. Well D as shown in Figure 5.28 was a partial success, in that gas sands were interpretable, but the response was small and disjointed, quickly thinning in depth.
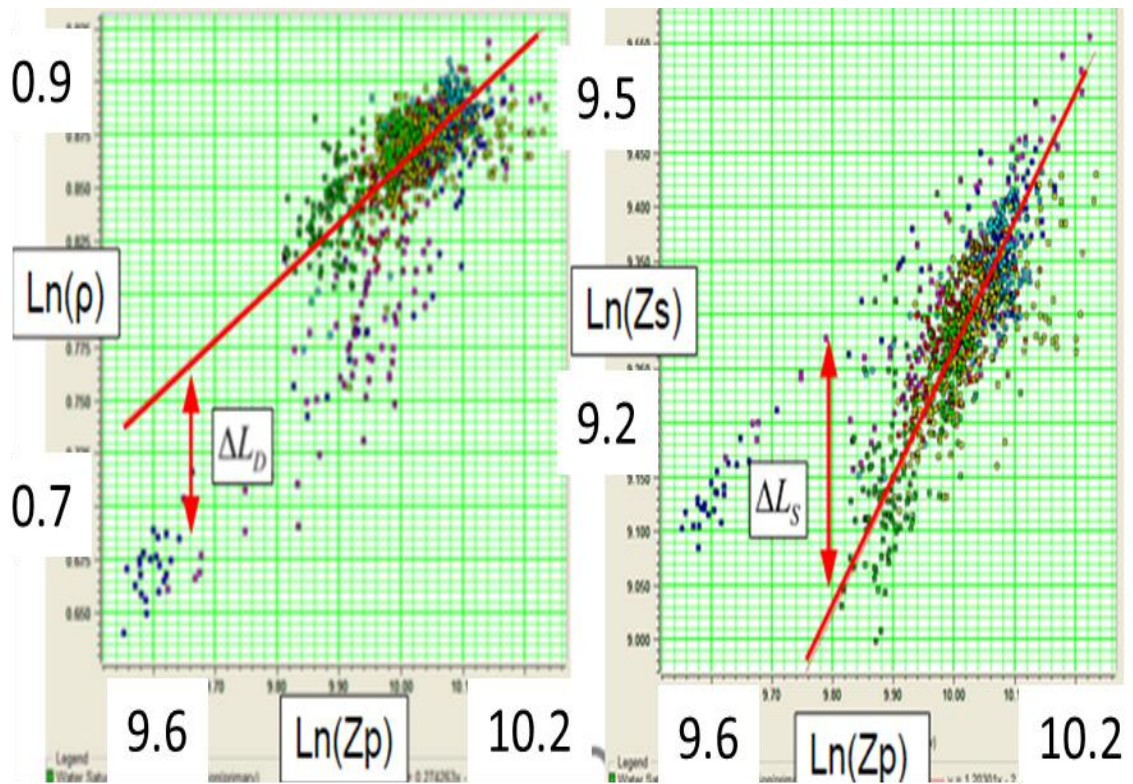
Figure 5.1 Example of linear approximations for shear impedance and density in relation to p-impedance (Hampson and Russel, 2005).
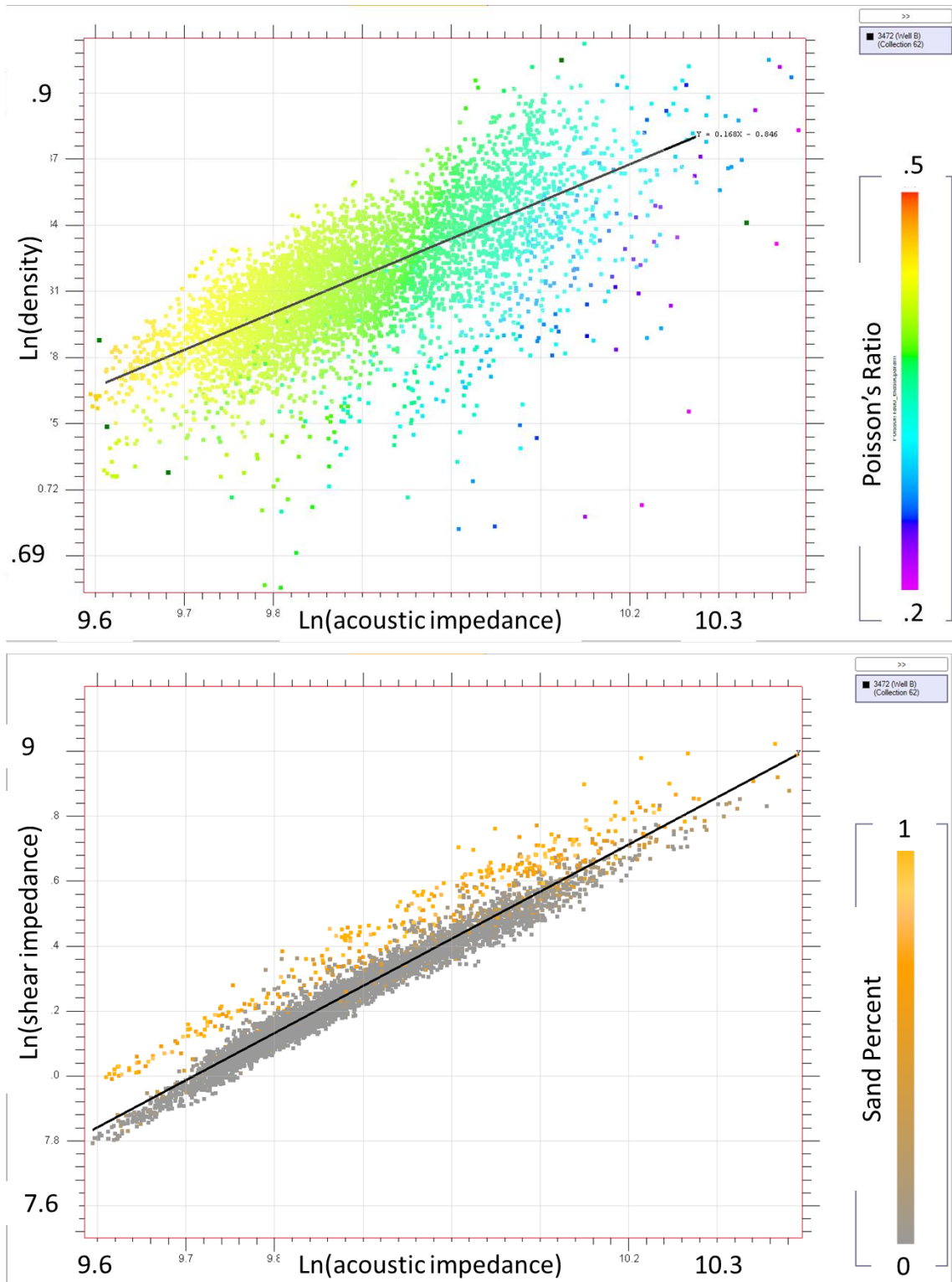
Figure 5.2 Linear trends between ln(acoustic impedance) and ln(density) at the top, and ln(acoustic impedance) and ln(shear impedance) at the bottom. Best fit trend lines from Well B are color - coded for values of Poisson's Ratio (top) and lithology (bottom).
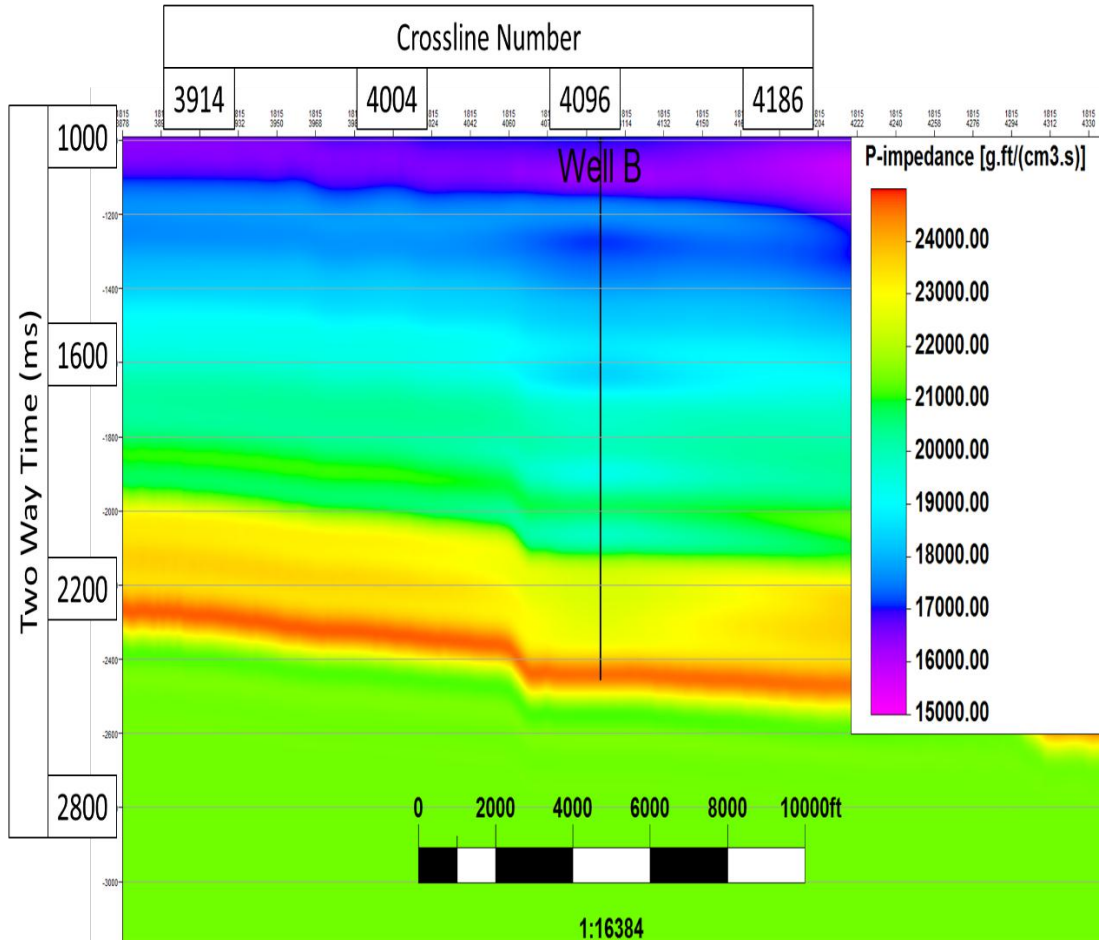
Figure 5.3 Low frequency P-impedance model built using the P - Velocity and density logs from Wells A and B
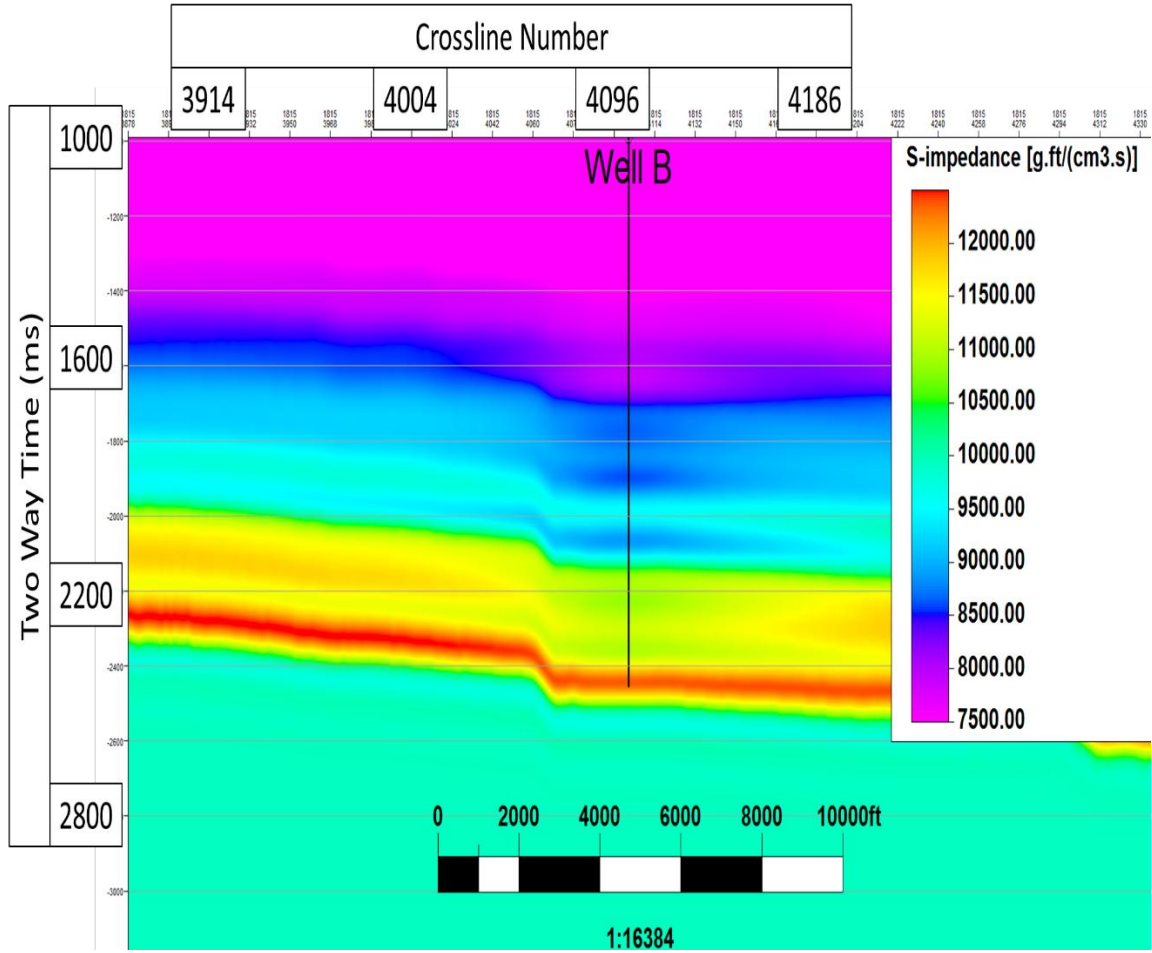
Figure 5.4 Low frequency S-impedance model, built using a Vp/Vs = 2 assumption along with the density logs from Wells A and B
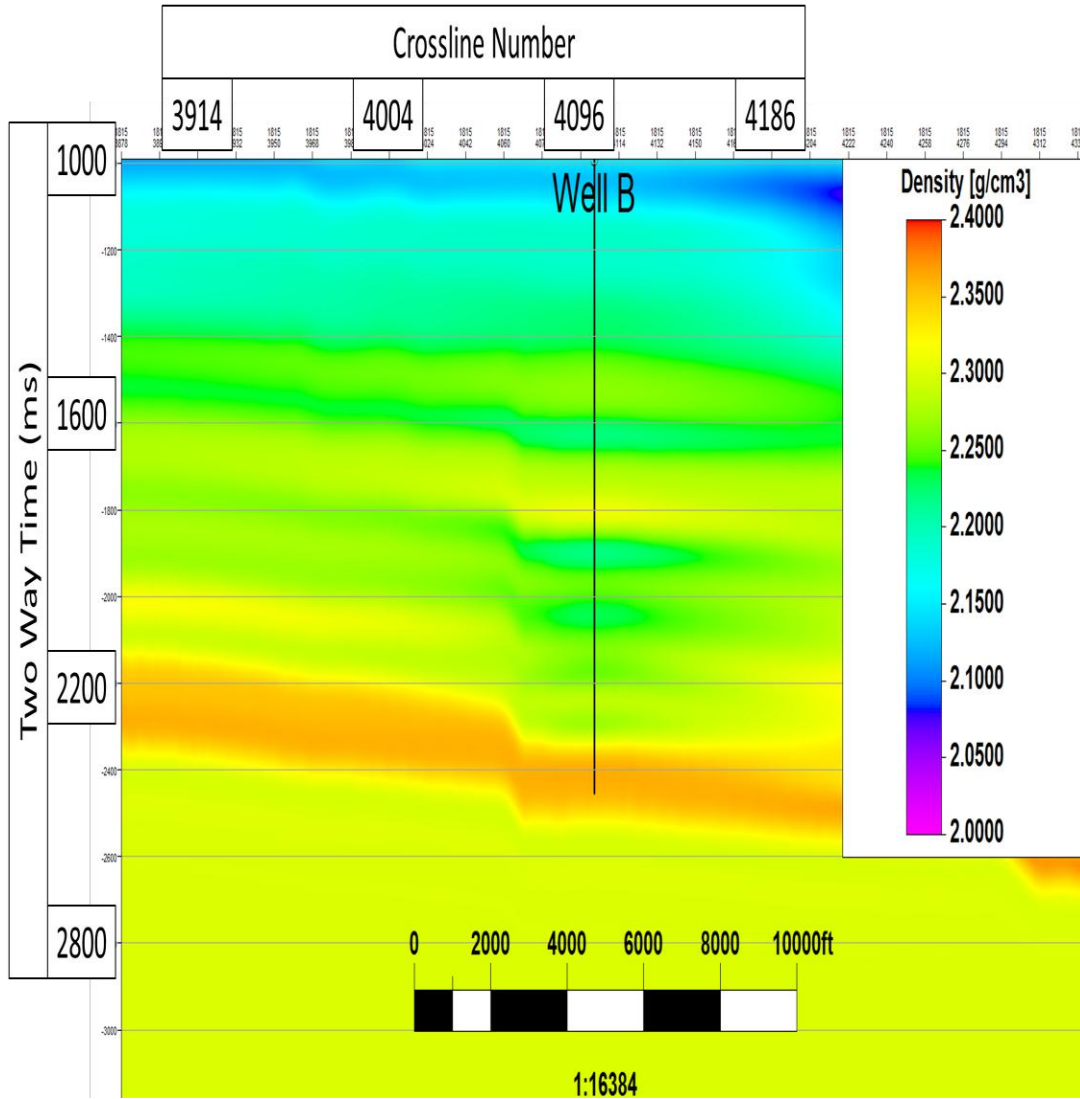
Figure 5.5 Low frequency density model built using density logs from Wells A and B.
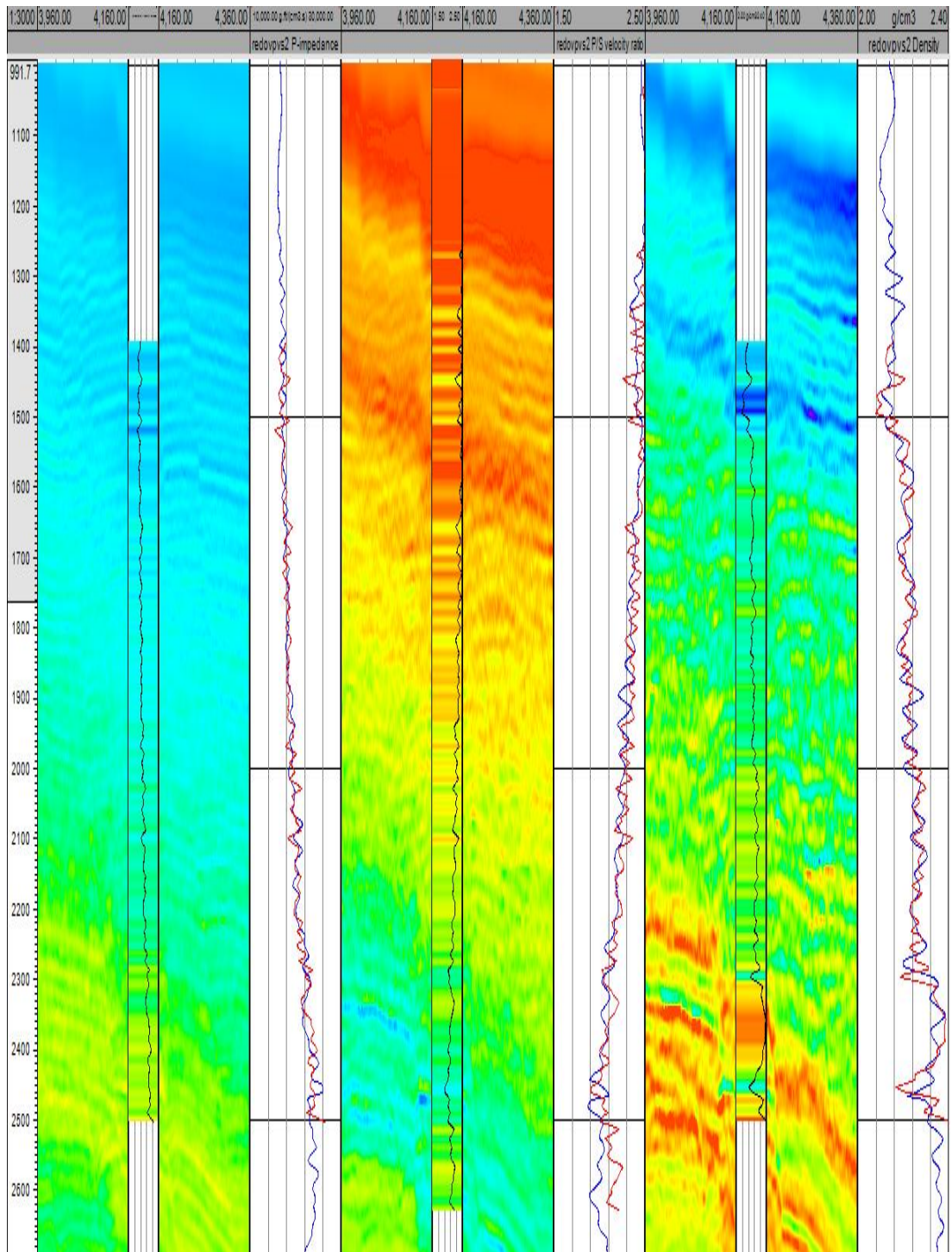
Figure 5.6. Inversion Results from Well A. From left to right are P-impedance, Vp/Vs ratio, and density. In this instance, the results are fairly comparable to the well log dataset, including the density result.
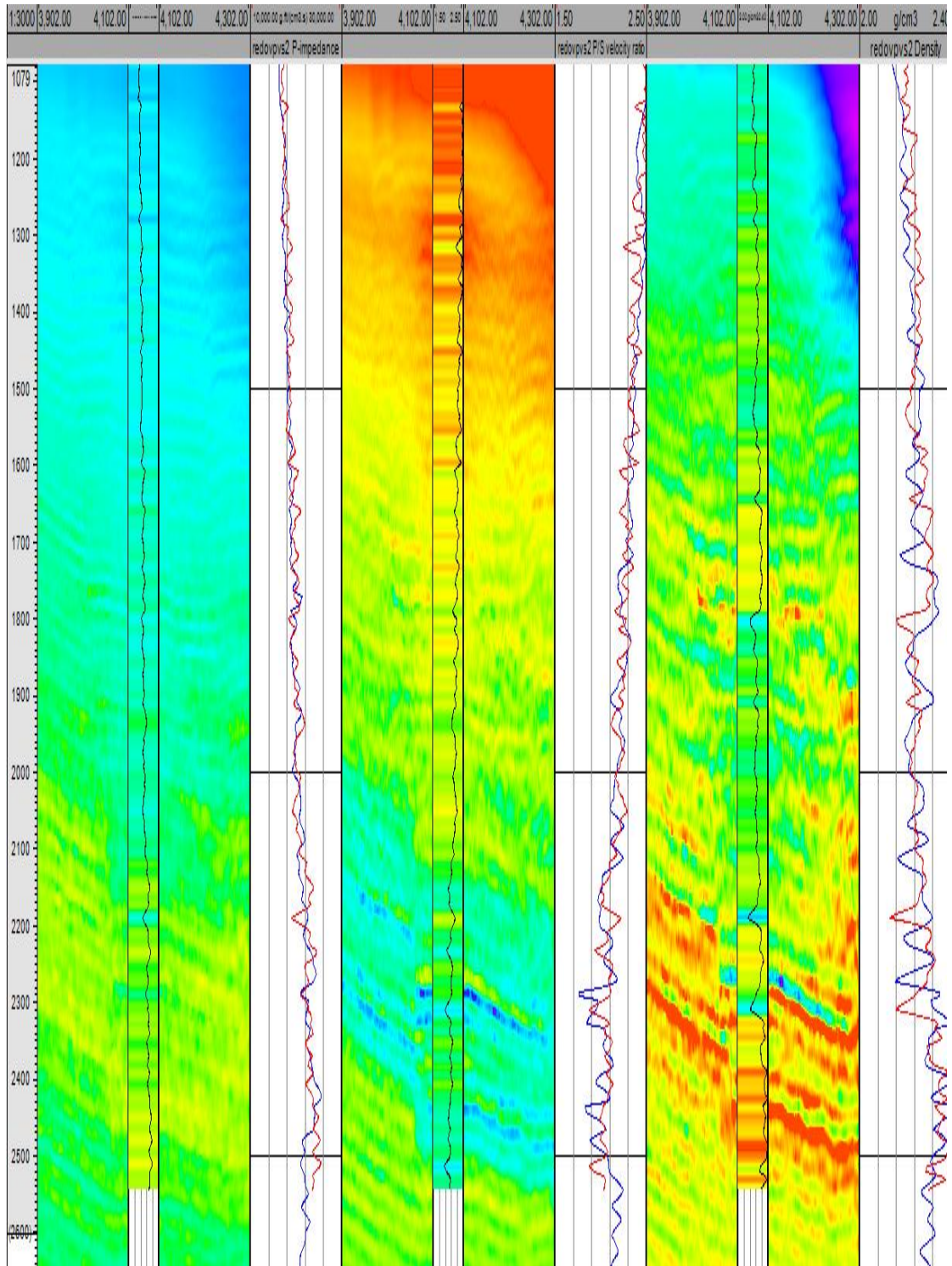
Figure 5.7. Results from Well B. Compared to Well A, the results for density are more erratic, though the expected drop in density and Vp/Vs ratio is still present in the hydrocarbon zones.
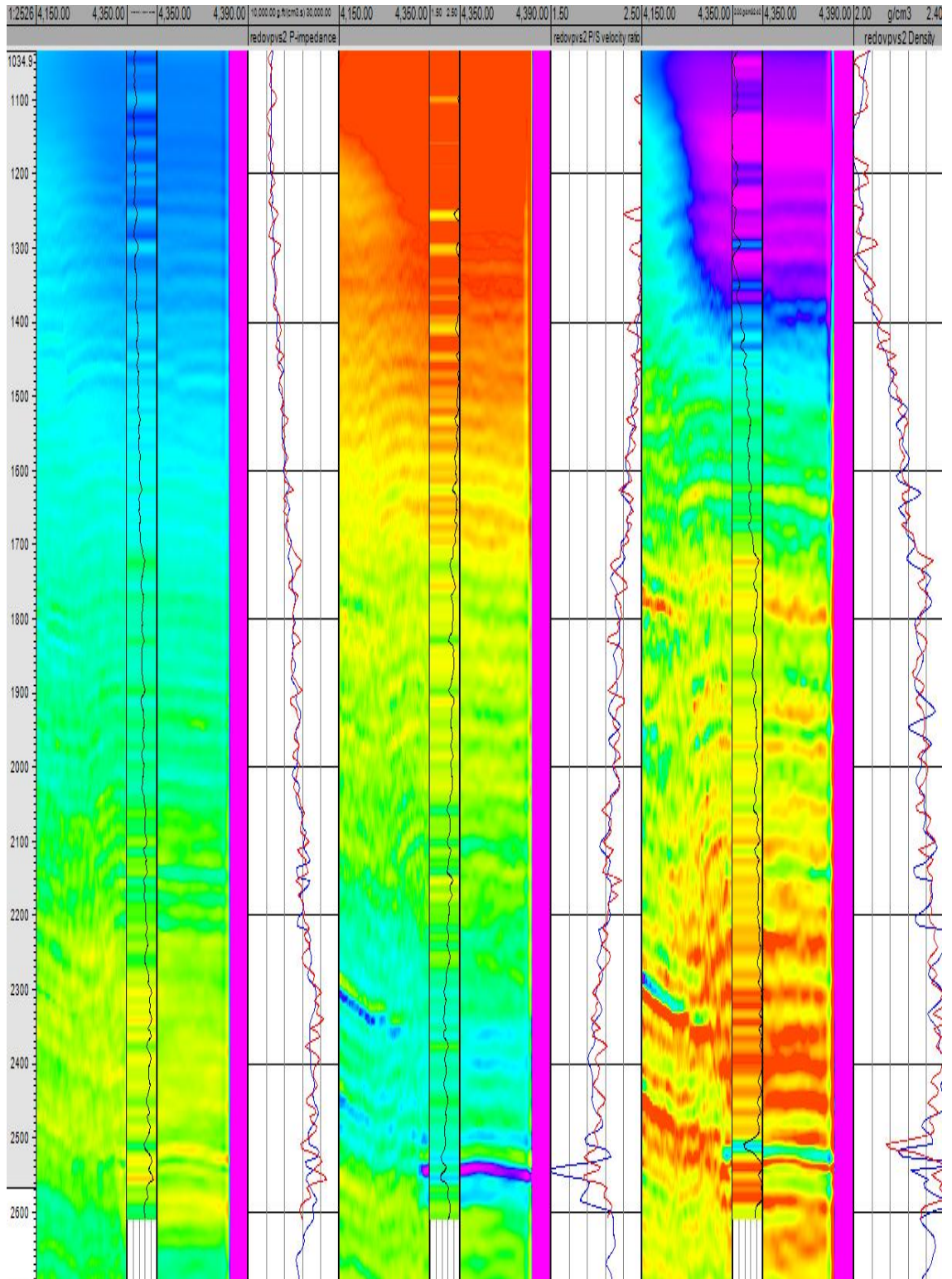
Figure 5.8 Results from Well C. Compared to Well A, the P-impedance and density results are fair at this location, the Vp/Vs ratio result is lower, about .4 less than the well measurement.
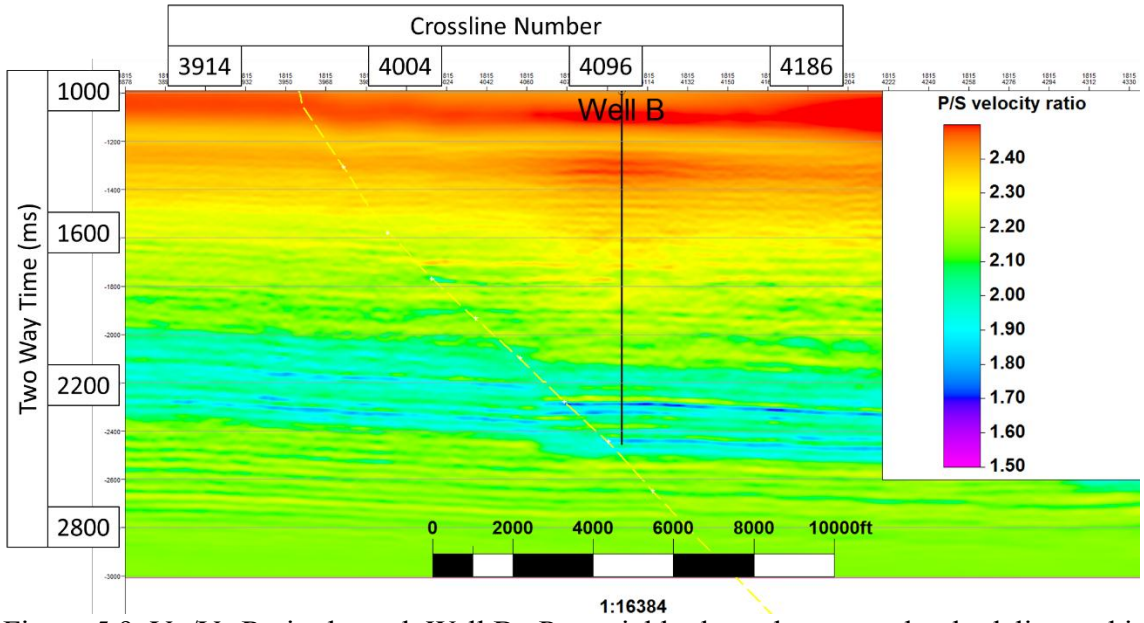
Figure 5.9. Vp/Vs Ratio through Well B. Potential hydrocarbons are clearly delineated in the dark blue values, representing Vp/Vs of around 1.7 vs. the background 2.
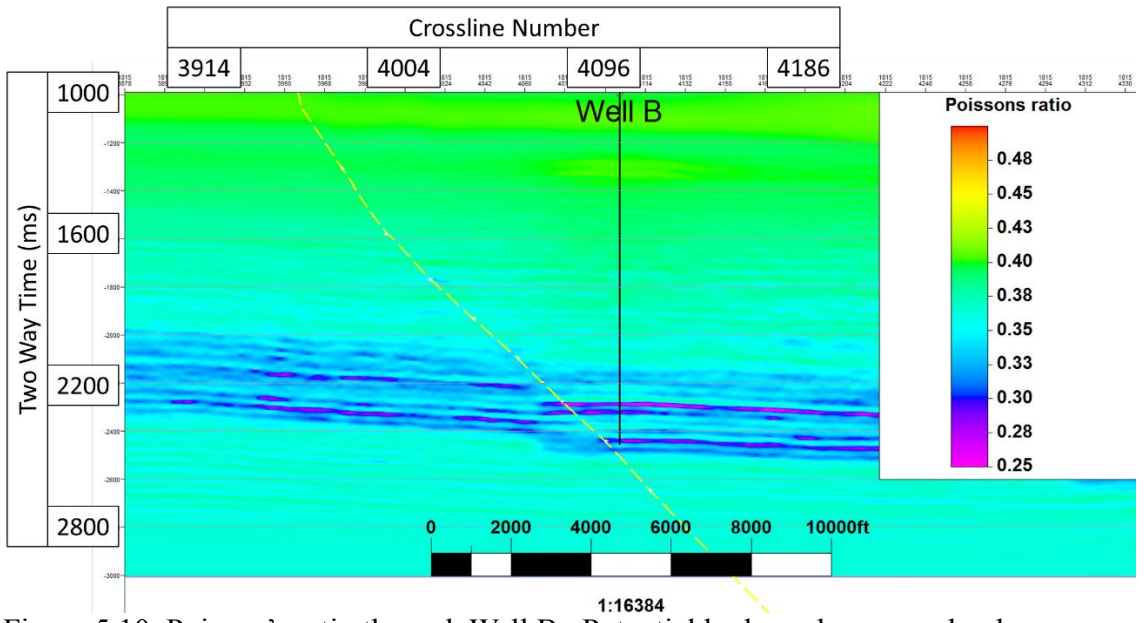
Figure 5.10. Poisson's ratio through Well B. Potential hydrocarbons are clearly delineated in the dark blue values, representing a lower ratio than the background.
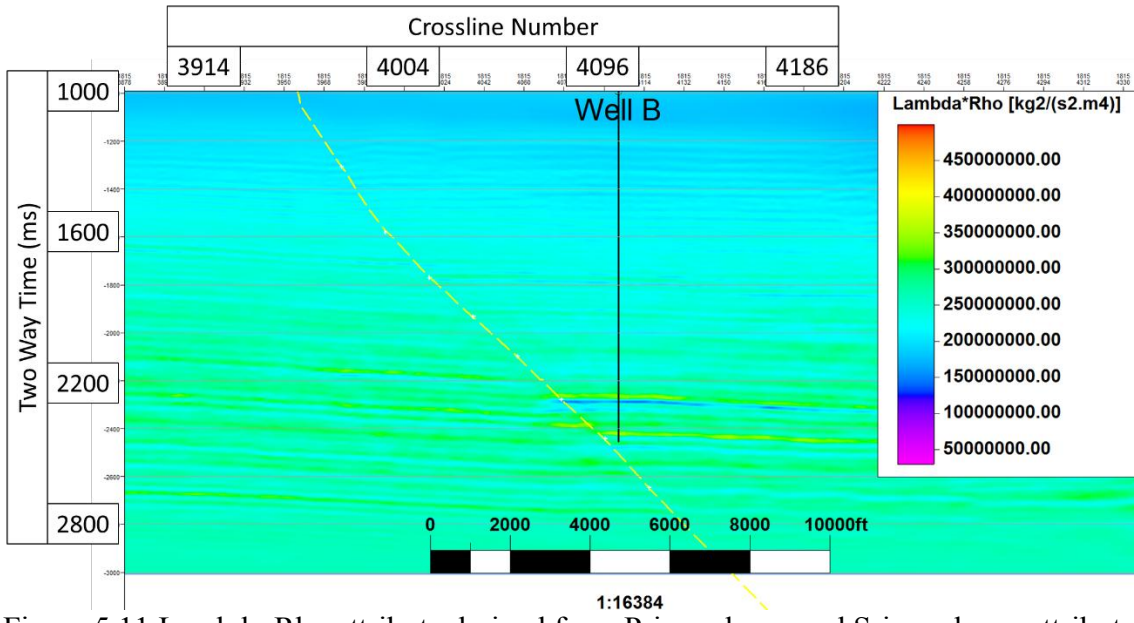
Figure 5.11 Lambda-Rho attribute derived from P-impedance and S-impedance attributes through Well B.
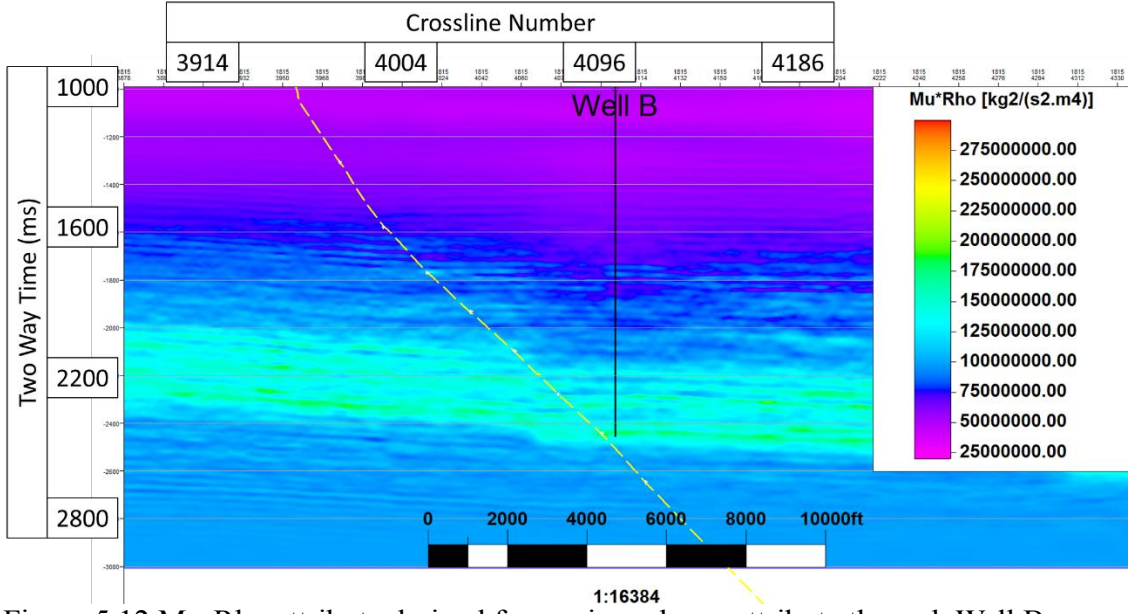
Figure 5.12 Mu-Rho attribute derived from s-impedance attribute through Well B. Similar to shear impedance in that it does not distinguish much in the way of pore fluid.
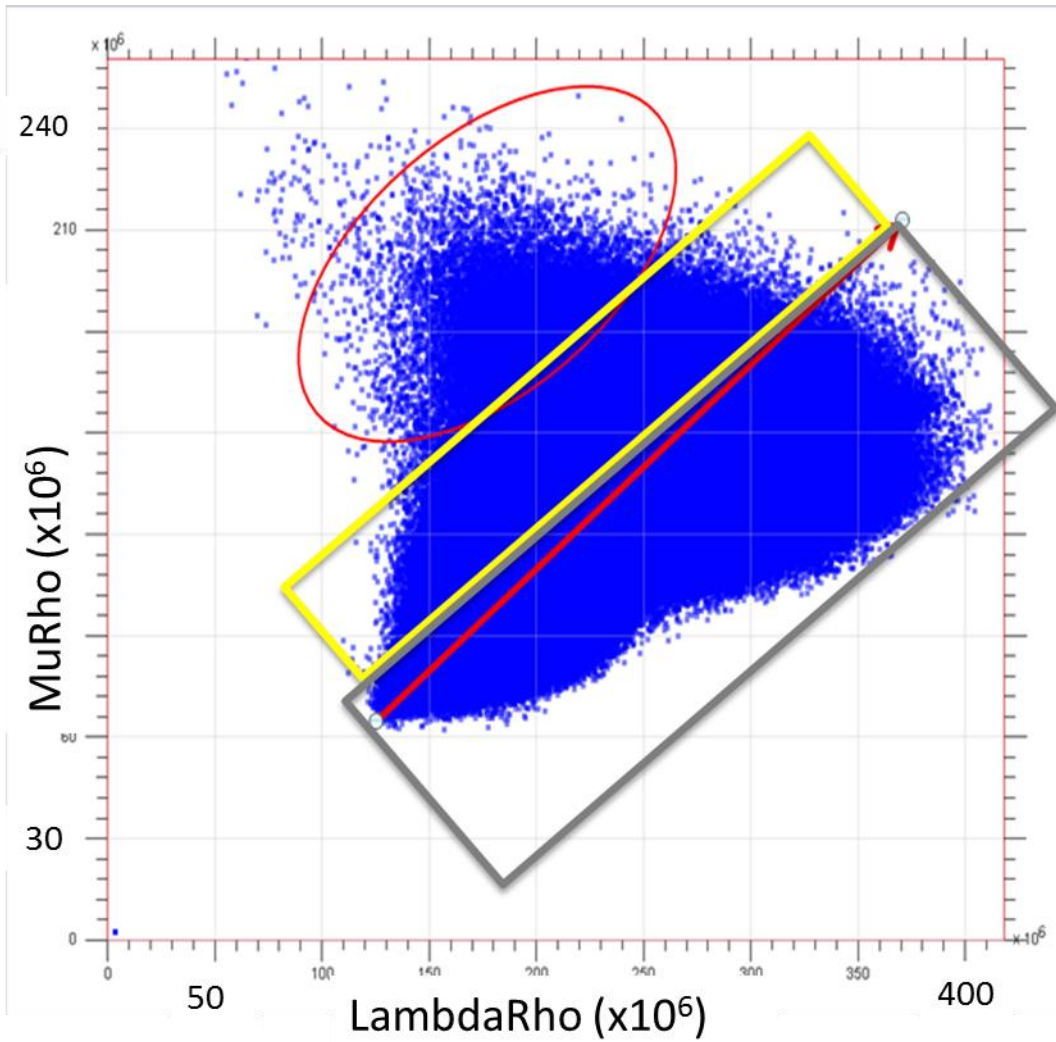
Figure 5.13 LMR Crossplot. Interpretation based on well-log trends of the background shale (red arrow) and gas sand response (red ellipse) with clean sand (yellow rectangle) and shale (grey rectangle) indicated. I decided that this attribute was not distinct enough to accurately delineate the gas sands and clean sands from the shale background.
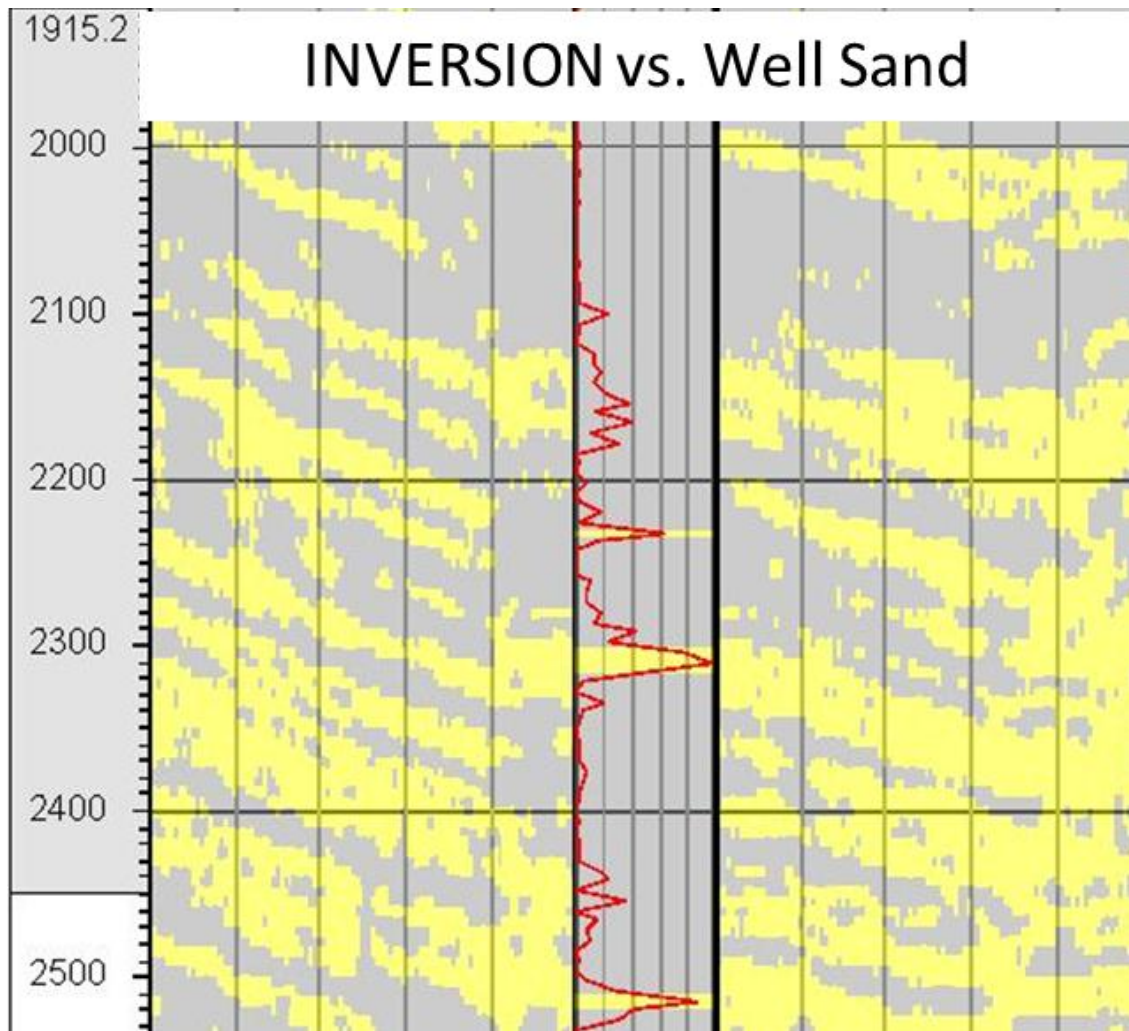
Figure 5.14 Plot of lithology around Well B based on Figure 5.15. Sand (yellow) in the inverted volume is based on a 50% cutoff.   Overall, the inversion results seem to indicate a minimum 20% sand lithology.
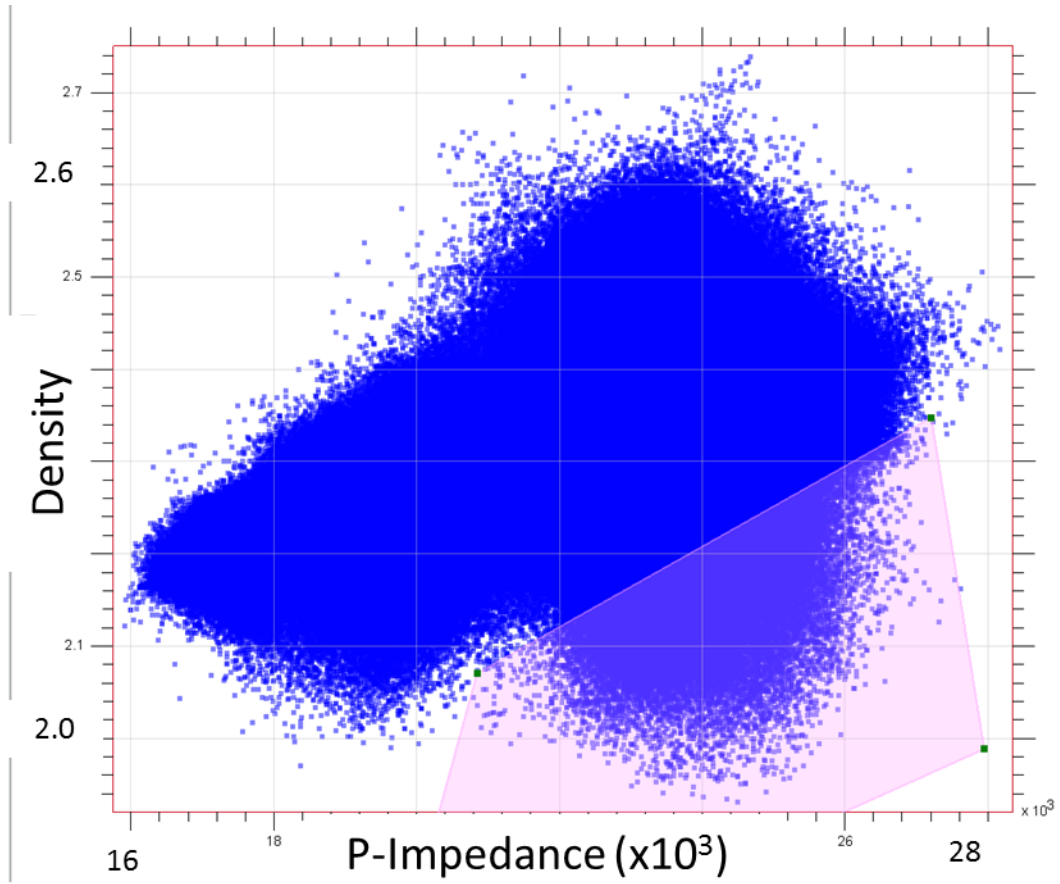
Figure 5.15 P-impedance vs. density crossplot shows a distinct density anomaly at a similar P-impedance to the background trend.
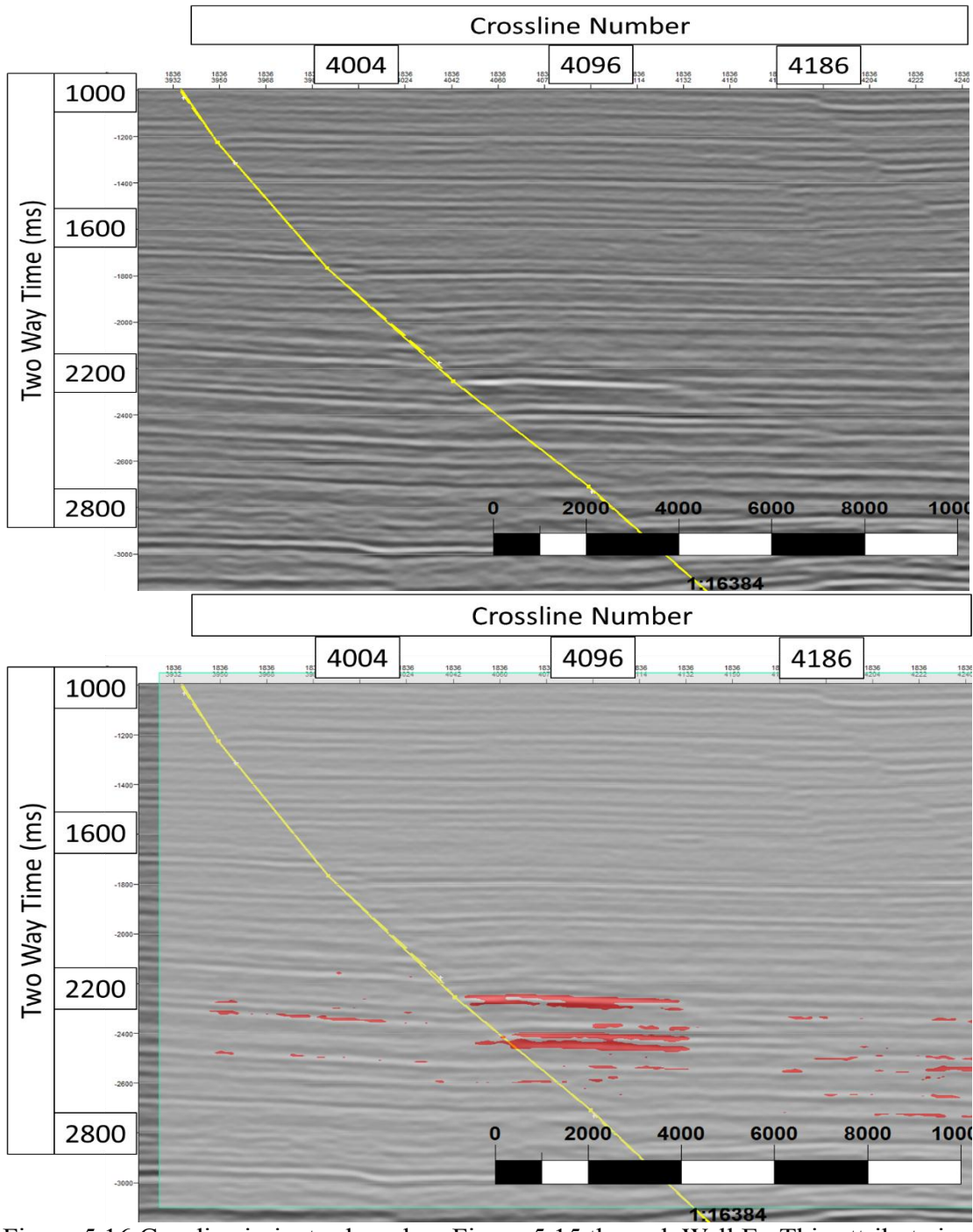
Figure 5.16 Gas discriminator based on Figure 5.15 through Well E. This attribute is a fair criterion for gas sands as this well location is expected to have two reservoirs in a stacked pay zone. Terminating fault displayed in yellow.
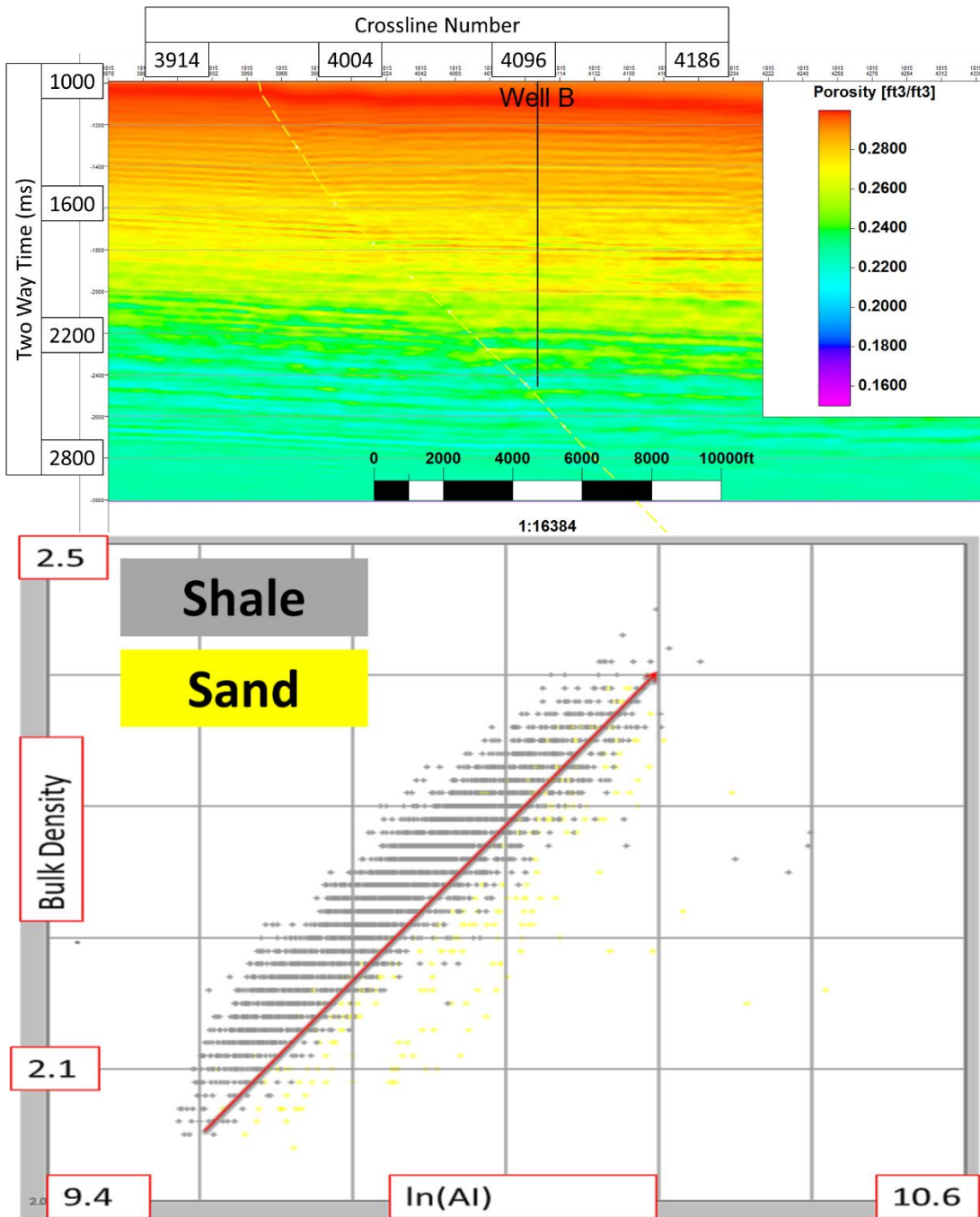
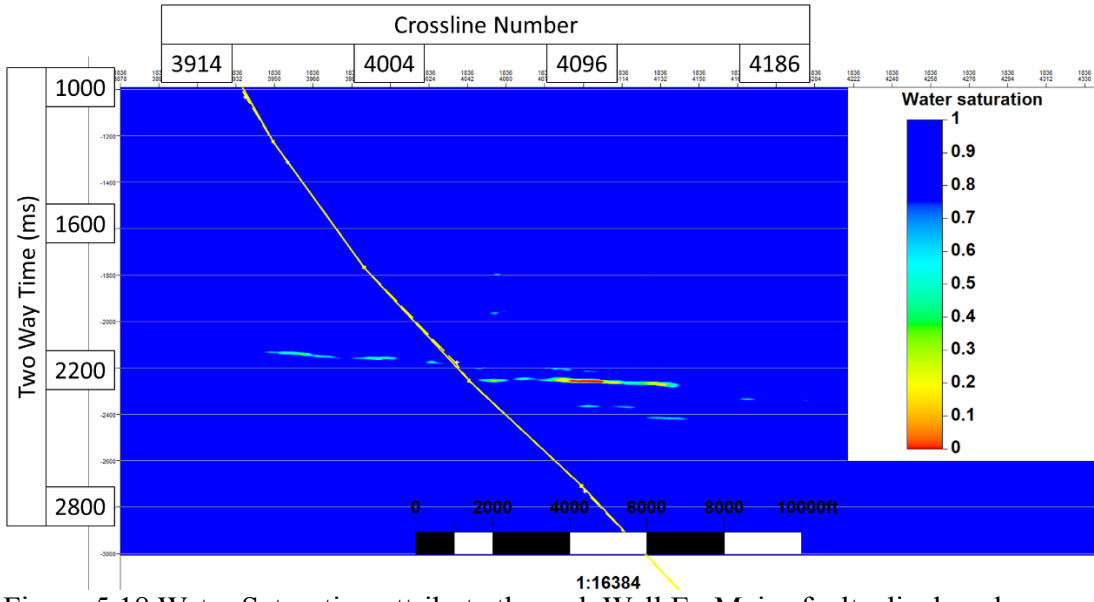Figure 5.17 Derived porosity volume based on P-impedance relationship as derived in well log information through Well B.

Figure 5.18 Water Saturation attribute through Well E. Major faults displayed.
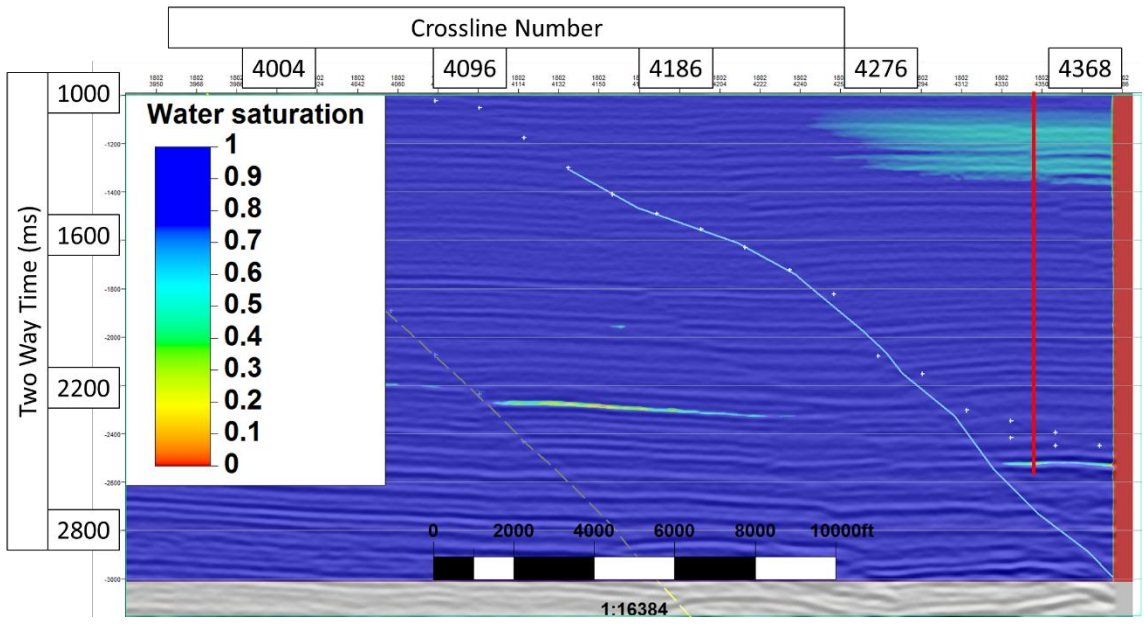

Figure 5.19 Water saturation attribute. QC of Well C shows a successful prediction of gas saturation at the reservoir time. Gas saturation peaks at the shallowest point and terminates approaching the fault. Major faults displayed.
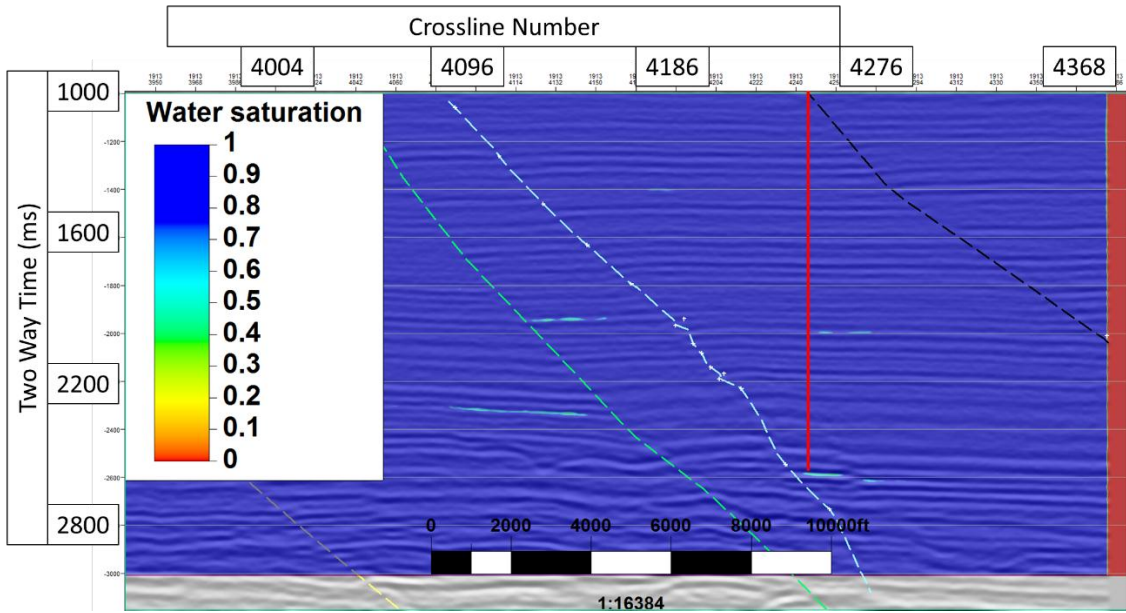
Figure 5.20 Water saturation attribute. QC of Well D in relation to gas saturation shows a successful prediction at the reservoir time. Gas saturation seems to mostly terminate at the fault plane, and there is evidence that the gas sand is in fact two thin beds near each other in this image. Major faults displayed.
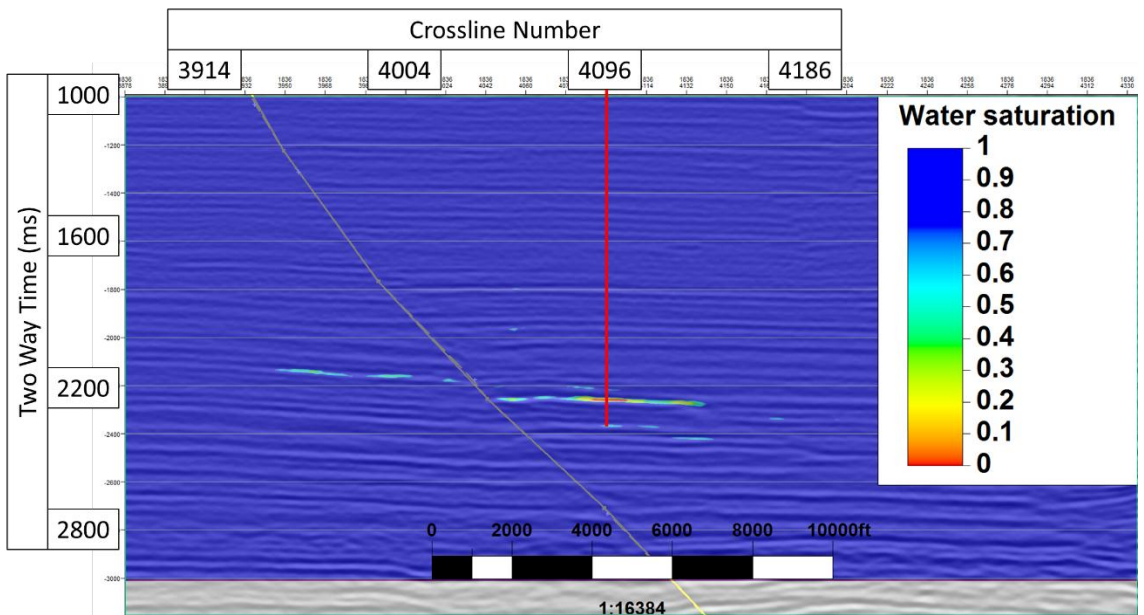

Figure 5.21 Water saturation attribute. QC of Well E in relation to gas saturation shows a successful prediction at the expected times for both reservoirs. Gas saturation terminated against fault A, and relative saturation is concentrated in local high points. Major faults displayed.
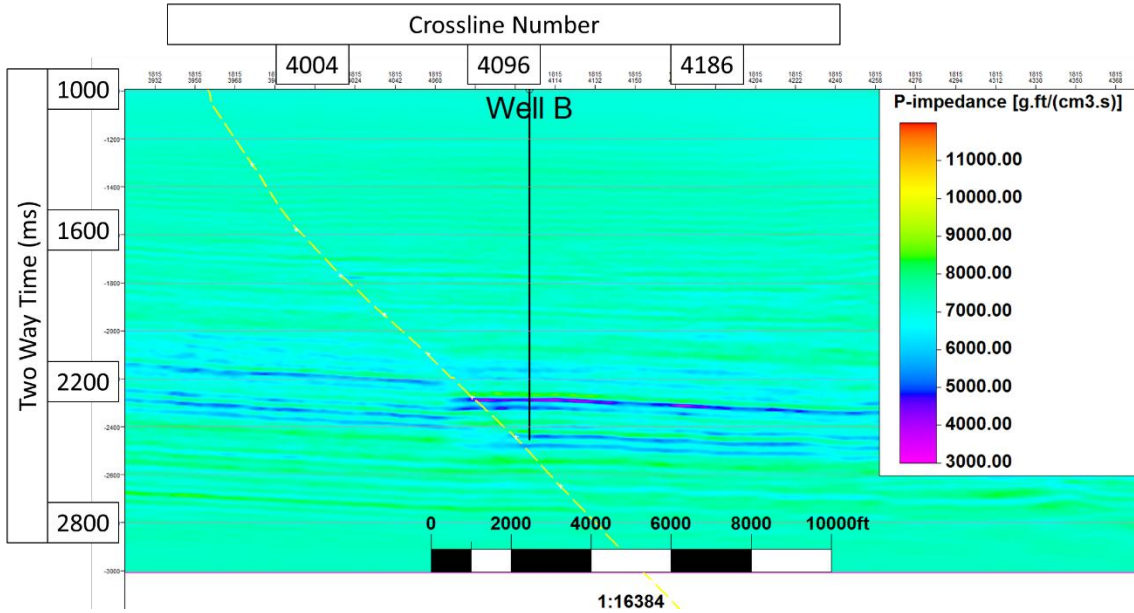
Figure 5.22 Poisson Impedance volume through Well B. Similar to Vp/Vs and Poisson's ratio attributes, PI highlights the fluid change around 2300 - 2500 ms. in dark blue vs. the light blue and green background. Major faults displayed.
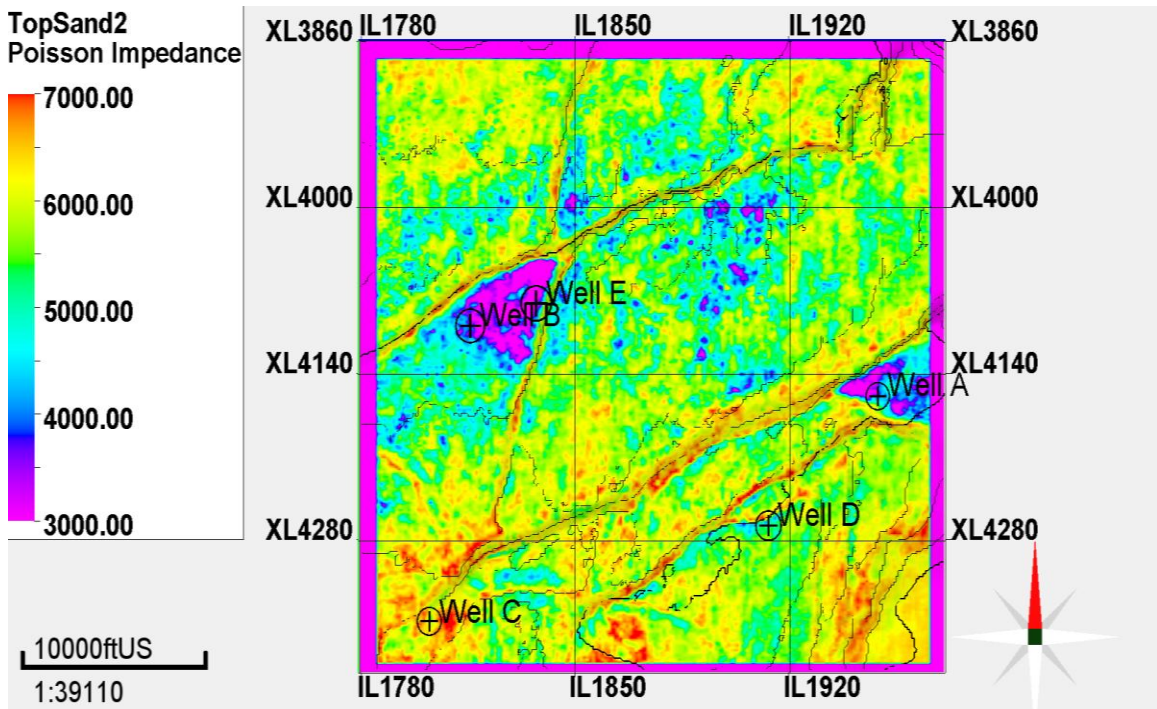

Figure 5.23 Poisson Impedance map extracted along the interpreted reservoir horizon. Both expected major reservoirs are clearly visible in purple with termination along faults.
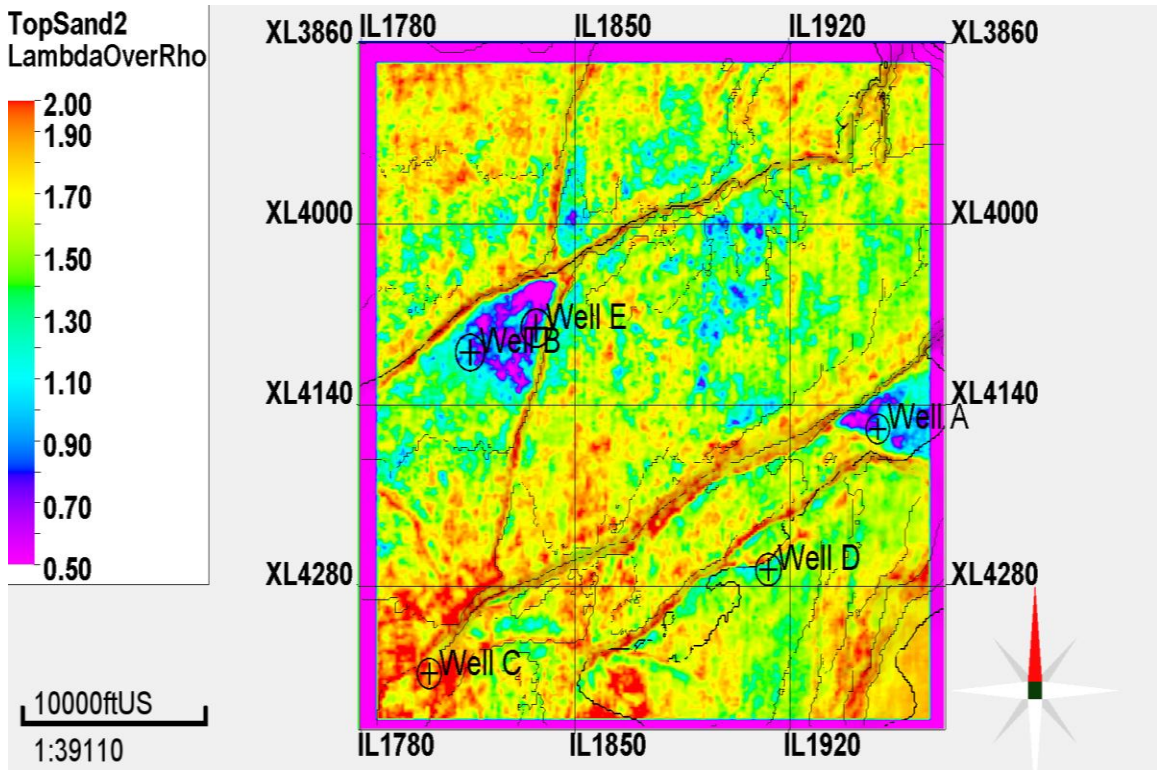
Figure 5.24. Lambda/Mu map extracted along the interpreted reservoir horizon. Similar to Poisson Impedance, expected gas reservoirs are visible as lower values than the background, light blue and purple.
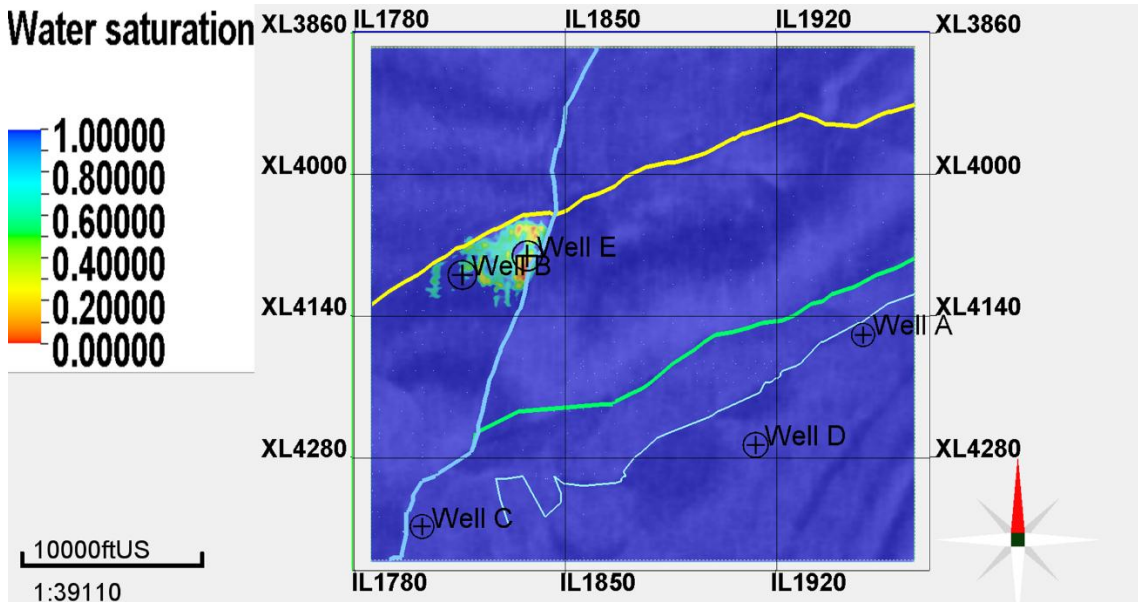

Figure 5.25 Time Slice at 2256 ms with water saturation overlaid confirms gas saturation at Well B and E locations, with closure along Faults A and B.
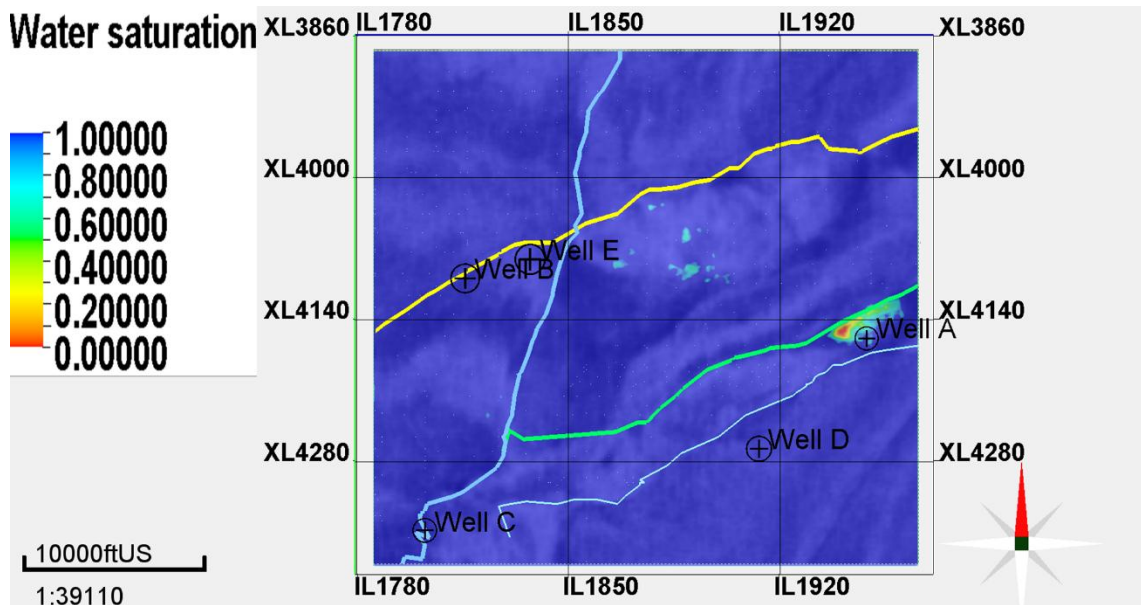
Figure 5.26 Time Slice at 2454 ms with water saturation overlaid confirms gas saturation at Well A, with terminations along Fault C and D.
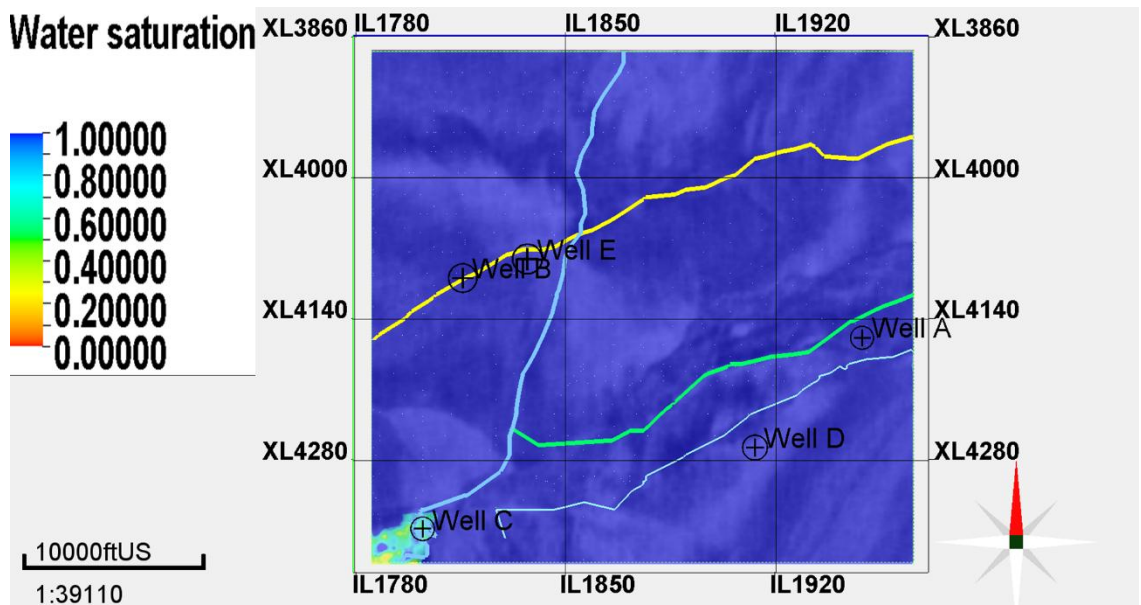

Figure 5.27 Time Slice at 2520 ms with water saturation overlaid confirms gas saturation at Well C. While the area around Well C is correctly interpreted as a gas reservoir, the lack of data further south limits interpretation of the reservoir extents, unlike Wells A, B, and E.
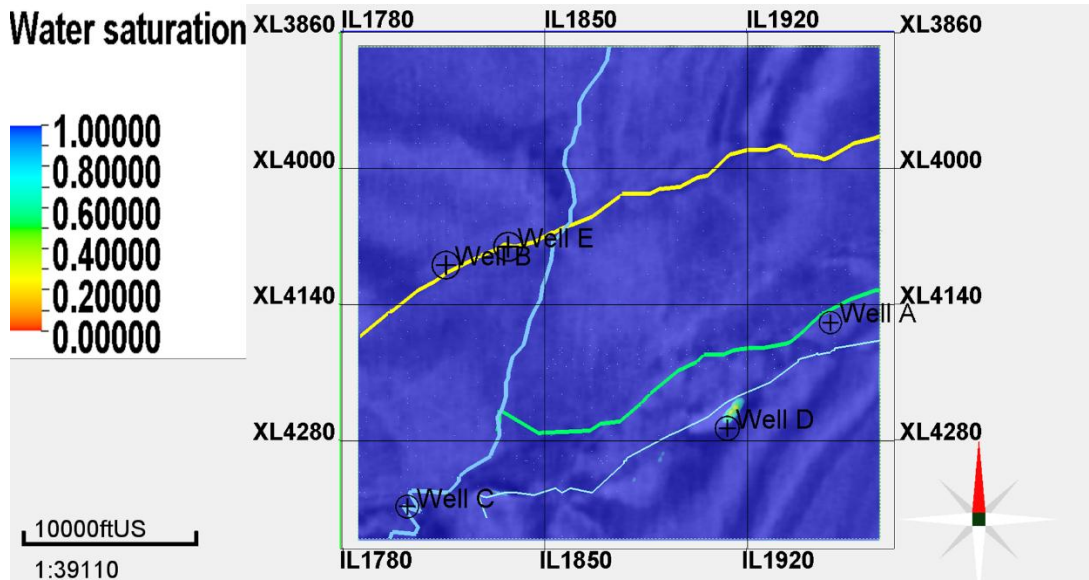
Figure 5.28 Time Slice at 2592 ms near Well D shows a small gas response that fades with further depth.

5.4 Conclusions

Throughout this experiment, the goal of being able to understand the lithology and accurately predict fluid properties was kept in mind. At each stage of the project, valuable information was gained.

1. Well Log curves provided insight in regards to detailed petrophysical properties. Estimations for fluid saturation and elastic parameters were first derived and related to one another in this controlled environment with well-log resolution and then to seismic resolution.

2. AVO analysis of the synthetic seismograms and available seismic data establish an understanding of the problem that traditional p-impedance contrasts were not

enough to make judgments on pore - fluid saturation. Class II AVO anomalies were observed, and a rotation in the NI-PR plane of the NIxPR attribute allowed for initial hydrocarbon delineation.

3. Seismic inversion results upscale the well-log information available to the full survey area. Through several attributes and rock-property estimation, a model of gas-saturated gas sands was generated. Using known wells as a blind QC, the inversion results successfully predicted gas saturation at all well locations.

Though fluid discrimination was successful, lithology was difficult to quantitatively define in this area. The lack of information on shear velocity, and the inherent reliance on generalized trends, limits the variability in the initial inversion model between different lithologies as well as establishing more precise trends distinguishing the two. Well information did corroborate a lack of p-wave velocity and density distinction between the thin sand and shale units, so perhaps addition log curves with shear sonic information could assist in finding a factor to separate lithology.

References

Aki K, and Richards P.G., 1979, Quantitative Seismology, W.H. Freeman & Co.

Archie, G. E., 1952, Classification of carbonate reservoir rocks and petrophysical considerations: AAPG Bulletin, **36**, p. 218–298.

Batzle, M., Wang, Z., 1992, Seismic properties of pore fluids: Geophysics, **57**, 1396-1408.

Benabentos, M. et al, 2007. Reservoir characterization in the Burgos Basin using simultaneous inversion: The Leading Edge, **26**, 556-561.

Boorman, C., Cowgill M., Ginal E., Mandley R., Thompson J., Roberts G., and Archer S., 2006, Huge potential still waiting in the Gulf of Mexico: GEO Expro Issue No. 4/5.

Bortfeld, R., 1961, Approximation to the reflection and transmission coefficients of plane longitudinal and transverse waves: Geophysical Prospecting, **9,** 485-502

Castagna, J.P., and Smith, S.W., 1994, Comparison of AVO indicators: a modeling study: Geophysics, **59**, 1849-1855.

Fatti, J. L., Smith G.C., Vail P.J., Strauss P.J., and Levitt P.R., 1994, Detection of gas in sandstone reservoirs using AVO analysis-A 3-D case history using Geostack technique: Geophysics, **59**, 1362-1376.

Goodway, W., Chen, T., and Downton, J., 1997, Improved AVO fluid detection and lithology discrimination using Lame petrophysical parameters; "Lambda-Rho" , "Mu-Rho" & "Lambda/Mu fluid stack", from P and S inversions: CSEG Recorder, **22**, 3-5

Greenberg, M. L., and J. P. Castagna, 1992, Shear - wave velocity estimation in porous rocks: Theoretical formulation, preliminary verification and applications: Geophysical Prospecting, **40**, 195-210.

Hampson D.P., Russell B.H., and Bankhead B., 2005, Simultaneous inversion of pre-stack seismic data: 75th Annual International Meeting, SEG expanded abstracts,1633–1636

Hilterman, F., 2001, Seismic Amplitude interpretation, SEG/EAGE 2001 Distinguished Instructor Short Course No. 4: Society of Exploration Geophysicists.

Liner, C. L., 2004, Elements of 3D Seismology (2nd edition): Pennwell Corporation.

Ma, X.Q., 2002. Simultaneous inversion of prestack seismic data for rock properties using simulated annealing: Geophysics, **67**, 1877-1885.

Ostrander, W. J., 1984, Plane - wave reflection coefficient for gas sand at non - normal angles of incidence: Geophysics, **49**, 1637-1648.

Reymond, B.A. and Stampfli G.M., 1996, Three - dimensional sequence stratigraphy and subtle stratigraphic traps associated with systems tracts: West Cameron region, offshore Louisiana, Gulf of Mexico: Marine and Petroleum Geology, **13**, 41-60.

Rutherford, S. R. and Williams R. H., 1989, Amplitude versus offset variations in gas sands: Geophysics, **54**, 680-688.

Shuey, R. T., 1985, A simplification of the Zoeppritz equations: Geophysics, **50**, 609-614.

White, R., 1997, The accuracy of well ties: Practical procedures and examples: 67th Annual International Meeting, SEG, Expanded Abstracts, 816-819.

Verm, R., and F. Hilterman, 1995, Lithology color - coded seismic sections, The calibration of AVO crossplotting to rock properties: The Leading Edge, **14**, 847-853.

Zhang, J.; Watkins, J.S., 1994, Plio - Pleistocene Structural Characteristics of Central Offshore Louisiana with Emphasis on Growth - Fault Interplay with Salt Tectonics: Gulf Coast Association of Geological Societies Transactions, **44**, 745 - 754

Zoeppritz, K., 1919, Erdbebenwellen VIIIB, On the reflection and propagation of seismic waves: Gottinger Nachrichten, **1**, 66-84.